ISSN 2074-272X

науково-практичний журнал 2021/5

Електротехніка і Електромеханіка

Electrical Engineering & Electromechanics

Електричні машини та апарати
Електротехнічні комплекси та системи
Силова електроніка
Електроізоляційна та кабельна техніка
Електричні станції, мережі і системи
Безпека електрообладнання

Журнал включено до найвищої категорії «А» Переліку фахових видань України

29 липня 2021 р. отримано позитивне рішення щодо включення журналу до Scopus

З 2015 р. журнал індексується у Web of Science Core Collection: Emerging Sources Citation Index

Electrical Engineering & Electromechanics

Scientific Journal was founded in 2002
Founders are:
National Technical University «Kharkiv Polytechnic Institute» (Kharkiv, Ukraine)
State Institution «Institute of Technical Problems of Magnetism of the NAS of Ukraine» (Kharkiv, Ukraine)

29th of July 2021 Journal «Electrical Engineering & Electromechanics» has been accepted for Scopus.

Journal «Electrical Engineering & Electromechanics» from no. 1 2015 is indexing in Web of Science Core Collection : Emerging Sources Citation Index (ESCI).

Also included in DOAJ (Directory of Open Access Journals), in EBSCO's database, in ProQuest's databases – Advanced Technologies & Aerospace Database and Materials Science & Engineering Database, in Gale/Cengage Learning databases.

Editorial office address:
National Technical University «Kharkiv Polytechnic Institute», Kyrpychova Str., 2, Kharkiv, 61002, Ukraine
phones: +380 57 7076281, +380 67 3594696, **e-mail:** a.m.grechko@gmail.com (**Grechko O.M.)**

ISSN (print) 2074-272X
ISSN (online) 2309-3404

Printed 26 October 2021. Format 60 × 90 ⅛. Paper – offset. Laser printing. Edition 200 copies.
Printed by Printing house «Madrid Ltd» (18, Gudanova Str., Kharkiv, 61024, Ukraine)

Electrical Engineering & Electromechanics
Scientific Journal

no. 5, 2021

Table of Contents

UDC 621.313.282 https://doi.org/10.20998/2074-272X.2021.5.01

V.F. Bolyukh, I.S. Schukin, J. Lasocki

INFLUENCE OF THE INITIAL WINDING DISPLACEMENT ON THE INDICATORS OF THE ELECTROMECHANICAL INDUCTION ACCELERATOR OF CYLINDRICAL CONFIGURATION

Purpose. *The purpose of the article is to determine the influence of the initial displacement of the windings on the indicators of an electromechanical induction accelerator of a cylindrical configuration with pulsed excitation from a capacitive energy storage and with short-term excitation from an alternating voltage source.* ***Methodology.*** *To take into account the interrelated electrical, magnetic, mechanical and thermal processes, as well as a number of nonlinear dependencies, we use the lumped parameters of the windings, and the solutions of the equations describing these processes are presented in a recurrent form. The mathematical model of the accelerator takes into account the variable magnetic coupling between the windings during the excitation of the inductor winding. When calculating the parameters and characteristics of the accelerator, a cyclic algorithm is used.* ***Results.*** *At a frequency of an alternating voltage source of 50 Hz, the current amplitude in the armature winding is less than in the inductor winding. With an increase in the source frequency to 250 Hz, the phase shift between the winding currents decreases. The current in the inductor winding decreases, and in the armature winding it increases. The accelerating components of the force increase, and the braking ones decrease. With an increase in the source frequency to 500 Hz, the current density in the armature winding exceeds that in the inductor winding. In this case, the phase shift between the windings is further reduced.* ***Originality.*** *When a cylindrical accelerator is excited, the largest amplitude of the current density in the inductor winding occurs at the maximum initial displacement of the windings, but the amplitude of the current density in the armature winding is the smallest. The largest value of the current density in the armature winding occurs in the absence of an initial displacement. When excited from a capacitive energy storage, the electrodynamic force between the windings has an initial accelerating and subsequent braking components. As a result, the speed of the armature initially increases to a maximum value, but decreases towards the end of the electromagnetic process. When a cylindrical accelerator is excited from an alternating voltage source, a phase shift occurs between the currents in the windings, which leads to the appearance of alternating accelerating and decelerating components of electrodynamic forces. The accelerating components of the force prevail over the braking components, which ensures the movement of the armature.* ***Practical value.*** *At a frequency of an alternating voltage source of 50 Hz, the highest speed at the output of the accelerator v_{zf}=0.5 m/s is realized at an initial displacement of the windings z_0=6.2 mm, at a frequency of 250 Hz, the highest speed v_{zf}=2.4 m/s is realized at z_0=3.1 mm, and at a frequency of 500 Hz the highest speed v_{zf}=2.29 m/s is realized at z_0=2.3 mm.* References 19, figures 9.

Key words: **electromechanical induction accelerator, cylindrical configuration, initial winding displacement, capacitive energy storage, alternating voltage source, armature speed.**

В електромеханічному індукційному прискорювачі циліндричної конфігурації найбільша амплітуда струму в обмотці індуктора виникає при максимальному початковому зсуві, але амплітуда струму в обмотці якоря при цьому найменша. Найбільша величина струму в обмотці якоря виникає при відсутності початкового зсуву. При збудженні від ємнісного накопичувача енергії електродинамічна сила між обмотками має початкову прискорювальну і подальшу гальмівну складові. Внаслідок цього швидкість якоря спочатку зростає до максимально величини, але потім зменшується до моменту закінчення електромагнітного процесу. При збудженні прискорювача від джерела змінної напруги (ДЗН) між струмами в обмотках виникає фазовий зсув, що призводить до почергової зміни прискорювальних і гальмівних складових електродинамічної сили. Прискорювальні складові сили переважають над гальмівними складовими, що забезпечує переміщення якоря. При частоті ДЗН 50 Гц амплітуда струму в обмотці якоря менше, ніж в обмотці індуктора. Зі збільшенням частоти ДЗН фазовий зсув між струмами обмоток зменшується, струм в обмотці індуктора зменшується, а в обмотці якоря збільшується. Прискорювальні складові сили збільшуються, а гальмівні – зменшуються. При підвищенні частоти ДЗН до 500 Гц щільність струму в обмотці якоря перевищує аналогічну величину в обмотці індуктора. Бібл. 19, рис. 9.

Ключові слова: **електромеханічний індукційний прискорювач, циліндрична конфігурація, початковий зсув обмоток, ємнісний накопичувач енергії, джерело змінної напруги, швидкість якоря.**

В электромеханическом индукционном ускорителе цилиндрической конфигурации наибольшая амплитуда тока в обмотке индуктора возникает при максимальном начальном смещении, но амплитуда тока в обмотке якоря при этом наименьшая. Наибольшая величина тока в обмотке якоря возникает при отсутствии начального смещения. При возбуждении от емкостного накопителя энергии электродинамическая сила между обмотками имеет начальную ускоряющую и последующую тормозящую составляющие. Вследствие этого скорость якоря вначале возрастает до максимально величины, но затем уменьшается к моменту окончания электромагнитного процесса. При возбуждении ускорителя от источника переменного напряжения (ИПН) между токами в обмотках возникает фазовый сдвиг, приводящий к возникновению чередующихся ускоряющих и тормозящих составляющих электродинамической силы. Ускоряющие составляющие силы преобладают над тормозящими составляющими, что обеспечивает перемещение якоря. При частоте ИПН 50 Гц амплитуда тока в обмотке якоря меньше, чем в обмотке индуктора. С увеличением частоты ИПН фазовый сдвиг между токами обмоток уменьшается, ток в обмотке индуктора уменьшается, а в обмотке якоря увеличивается. Ускоряющие составляющие силы увеличиваются, а тормозящие уменьшаются. При повышении частоты ИПН до 500 Гц плотность тока в обмотке якоря превышает аналогичную величину в обмотке индуктора. Библ. 19, рис. 9.

Ключевые слова: **электромеханический индукционный ускоритель, цилиндрическая конфигурация, начальное смещение обмоток, емкостной накопитель энергии, источник переменного напряжения, скорость якоря.**

Introduction. Electromechanical induction accelerators (EIAs) provide acceleration of the actuator to a high speed in a short active section [1-5]. In these coaxial accelerators, the stationary inductor winding, excited either from a capacitive energy storage (CES) or from an alternating voltage source (AVS), induces a current in the armature winding. The interaction of the armature winding current with the magnetic field of the inductor winding leads to the emergence of an electrodynamic force. Under the action of the axial electrodynamic force, the armature winding together with the actuator move linearly relative to the inductor winding, accelerating to high speed. All electromagnetic and electromechanical processes in the EIA proceed for a short time with indicators that significantly exceed the corresponding indicators of linear electric motors with a long operating mode.

EIAs are used in many areas of science and technology. Such accelerators are used in test installations for shock loads, in high-speed electrical devices and valve-switching equipment, in launchers, etc. [6-11] for example, work [12] describes a setup for testing electronic equipment in a collision with a moving object. Launchers are also used for many classes of unmanned aerial vehicles [4, 13]. Systems of active protection of armored devices from enemy objects on the approach are being developed on the basis of EIAs [14].

Features and problems of EIAs. EIAs with axial symmetry of the windings can have a disk or cylindrical configuration. In a disk accelerator, the windings of the inductor and the armature are made in the form of relatively thin disks with similar radial dimensions. In the initial position, the disk windings are set at the minimum axial distance from each other, at which the magnetic coupling is maximum. But as the armature winding accelerates, the magnetic coupling between the windings decreases sharply [15].

In a cylindrical accelerator, the windings are made in the form of hollow cylinders, the axial dimensions of which significantly exceed the radial thickness of the windings. In such an accelerator, the armature winding can move axially inside or outside the inductor winding. This makes such a design preferable, since with a larger displacement of the armature winding, and hence a longer interaction time, an effective magnetic coupling between the windings is ensured. Figure 1 shows a diagram of an EIA of a cylindrical configuration with a fixed outer winding of the inductor 1 and an accelerated inner winding of the armature 2. As the armature winding axially displaces inside the inductor winding, the magnetic coupling, characterized by the mutual inductance M_{12} between the windings, remains at a greater distance when the armature winding moves in comparison with the disk accelerator. This makes the design of the cylindrical accelerator more promising in comparison with the disk configuration.

The armature can be made in the form of a multi-turn short-circuited winding or in the form of a massive electrically conductive element. The massive armature is structurally simpler and has increased reliability. However, the induced current in the massive armature is distributed nonuniformly over the volume, which negatively affects the electromechanical parameters of the EIA. In a tightly wound multi-turn short-circuited armature, impregnated and monolithic with epoxy resin, despite a more complex design and reduced reliability, a uniform distribution of the induced current over the volume is ensured [6]. This makes it more promising, especially for the cylindrical EIA.

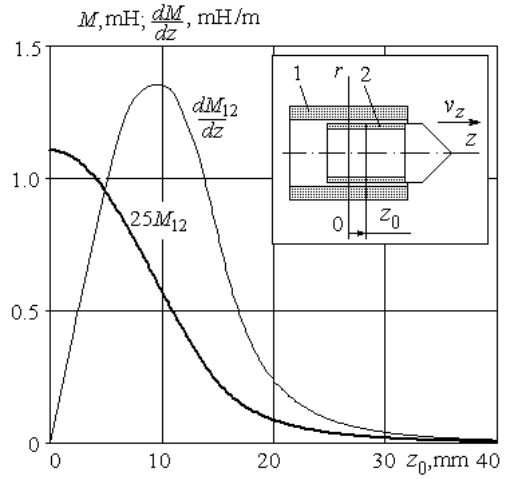

Fig. 1. Dependence of the mutual inductance between the windings M_{12} and its gradient dM_{12}/dz of the EIA on the initial displacement of the windings z_0:
1 – inductor winding; 2 – armature winding

However, in the EIA of the cylindrical configuration, the problem arises of choosing the initial displacement z_0 of the armature winding relative to the inductor winding. This is due to the fact that in the absence of the indicated displacement, when the central planes of the windings coincide, the magnetic coupling between the windings will be greatest. Accordingly, the induced current in the armature winding will be the highest. However, the axial electrodynamic force

$$f_z(t,z) = i_1(t) i_2(t) \frac{dM_{12}}{dz}(z),$$

where i_1, i_2 are the currents in the inductor and armature windings, respectively, driving the armature winding will be absent. This is due to the fact that the force f_z is proportional to the gradient of the mutual inductance in the axial direction dM_{12}/dz. As the initial displacement z_0 of the armature winding 2 increases relative to the inductor winding 1, the value of the mutual inductance M_{12} between the windings decreases, while the gradient of the mutual inductance dM_{12}/dz has a maximum at a certain value of z_0 (Fig. 1).

Since the currents in the accelerator windings flow for a short time, the question arises about the choice of the initial displacement z_0 of the armature winding 2 relative to the inductor 1 winding, at which the EIA of the cylindrical configuration provides the highest speed of the armature winding together with the actuator at the output of the accelerator v_{zf}.

The goal of the paper is to determine the influence of the initial displacement of the windings on the indicators of an electromechanical induction accelerator of a cylindrical configuration with pulsed excitation from

a capacitive energy storage and with short-term excitation from an alternating voltage source.

EIA mathematical model. Consider an electromechanical induction accelerator, in which the windings are tightly wound with round copper wire and made monolithic by impregnation with epoxy resin, followed by its hardening. To take into account the interrelated electrical, magnetic, mechanical and thermal processes, as well as a number of nonlinear dependencies, for example, of resistance on temperature, we use the lumped parameters of the windings, and the solutions of the equations describing these processes will be presented in a recurrent form [16]. The mathematical model of the EIA takes into account the changing magnetic coupling between the windings during the excitation of the inductor winding.

When calculating the parameters and characteristics of the accelerator, a cyclic algorithm is used. For this, the workflow is divided into a number of numerically small time intervals $\Delta t = t_{k+1} - t_k$ within which all quantities are considered unchanged. On the k-th cycle, using the parameters calculated at the time t_k as initial values, the parameters are calculated at the time t_{k+1}. To determine the currents over the time interval Δt, we use linear equations with unchanged parameter values. We choose a small value of the calculated step Δt so that it does not have a significant effect on the results of computer calculations, while ensuring the required accuracy.

The change in the spatial position of the armature winding is taken into account by the change in flux linkage Ψ between the windings [16]:

$$\frac{d\Psi}{dt} = M_{12}(z)\frac{di_n}{dt} + v_z(t)i_n\frac{dM_{12}}{dz},$$

where n = 1, 2 are the indices of the inductor and armature windings, respectively; v_z is the speed of movement of the armature winding along the z-axis.

Initial conditions of the mathematical model:
$i_n(0) = 0$ – current of the n-th winding;
$h_z(0) = z_0$ – armature winding displacement;
$T_n(0) = T_0$ – temperature of the n-th winding;
$u_c(0) = U_0$ – CES voltage;
$u(0) = U_\text{m} \sin\psi_u$ – AVS voltage;
$v_z(0) = 0$ – armature winding speed along the z-axis,
where U_m – voltage amplitude;
ψ_u=0 – initial phase of AVS voltage.

The mathematical model of the electromagnetic processes of the EIA at excitation from the CES is presented in [17], and at excitation from the AVS – in [18]. The mechanical processes of the accelerator take into account the masses of the armature winding and the actuator, the instantaneous position of the armature winding, the electrodynamic force between the windings and the aerodynamic resistance of the air environment [15]. The thermal processes of the accelerator take into account the specific heat, thermal conductivity, material density, specific resistance and current density j_n of the windings. Boundary conditions of the third kind are used on the cooling surfaces of the windings, and boundary conditions of the second kind are used on the axis of symmetry [19].

The amplitudes of the current densities in the windings of the inductor j_{1m} and of the armature j_{2m}, the amplitude of the electrodynamic force between the windings f_{zm}, the highest value of the armature speed v_{zm}, the speed of the armature at the output of the accelerator v_{zf}, when the electromagnetic processes decay, and the temperature rise of the inductor winding θ_1 and the armature winding θ_2 are used as the main indicators of the EIA.

EIA parameters. Consider an electromechanical accelerator with the following parameters: the inductor winding has an outer diameter D_{1ex} = 39 mm, an inner diameter D_{1in} = 27 mm, an axial height H_1 = 45 mm, and the number of turns N_1 = 120; the armature winding has an outer diameter D_{2ex} = 26 mm, an inner diameter D_{2in} = 20 mm, an axial height H_2 = 30 mm, and the number of turns N_2 = 40. The windings are wound with a round copper wire with a diameter of d_0 = 1.3 mm.

The CES has an energy of W_0 = 625 J and is implemented in two versions. Option I of the CES – charging voltage U_0 = 500 V and capacitance C_0 = 5000 μF and option II of the CES – U_0 = 707 V, C_0 = 2500 μF, which provide different duration of electrical processes.

The alternating voltage source has a voltage amplitude U_m = 100 V at frequencies of 50, 250 and 500 Hz and is connected to the inductor winding for a short time (t = 45 ms).

Let us consider the influence of the initial displacement z_0 of the armature winding relative to the inductor winding on the characteristics of the EIA of a cylindrical configuration. Note that for an accelerator with the specified geometrical parameters, the greatest value of the gradient of mutual inductance dM_{12}/dz occurs at z_{0m}≈10 mm (Fig. 1).

EIA indicators when excited from a capacitive energy storage. Let us consider the characteristics of the accelerator in the absence of an initial displacement (z_0 = 0), at a maximum displacement (z_0 = 20 mm) and at an intermediate displacement, in which the highest armature speeds at the output of the accelerator v_{zf} are provided.

The currents in the EIA windings have a vibration-damping character (Fig. 2,*a*).

When using the CES option I, the largest amplitude of the current density in the inductor winding j_{1m}= = 1.12 kA/mm^2 occurs at the maximum initial displacement, but the amplitude of the current density in the armature winding is the smallest – j_{2m}=0.2 kA/mm^2. The largest value of the current density – j_{2m}=1.4 kA/mm^2 occurs in the absence of an initial displacement. Note that for any initial displacement z_0, the currents in the windings practically decay after 10 ms.

The electrodynamic force f_z between the windings has an initial accelerating (positive) and subsequent braking (negative) components (Fig. 2,*b*). The accelerating component of the force arises at opposite polarities of the currents in the windings, and the braking one – at the same polarities of the currents. With an intermediate initial displacement z_0 = 8 mm, the amplitude of the accelerating component of the force is f_{zm} = 1.64 kN. Due to this pattern of changes in the electrodynamic force, the speed of the armature first

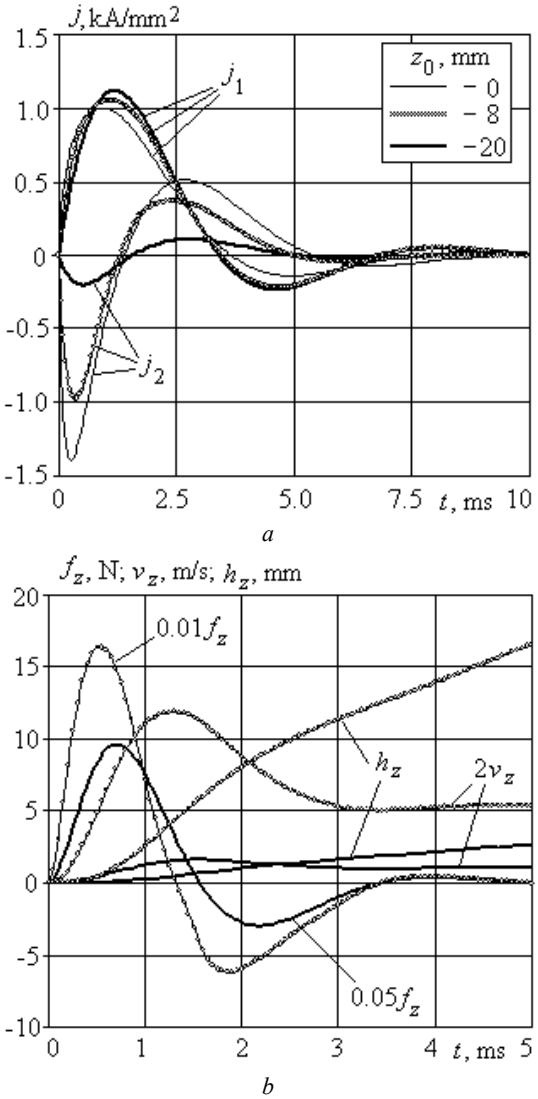

Fig. 2. Electrical (*a*) and mechanical (*b*) characteristics of the EIA at C_0=5000 μF, U_0=500 V

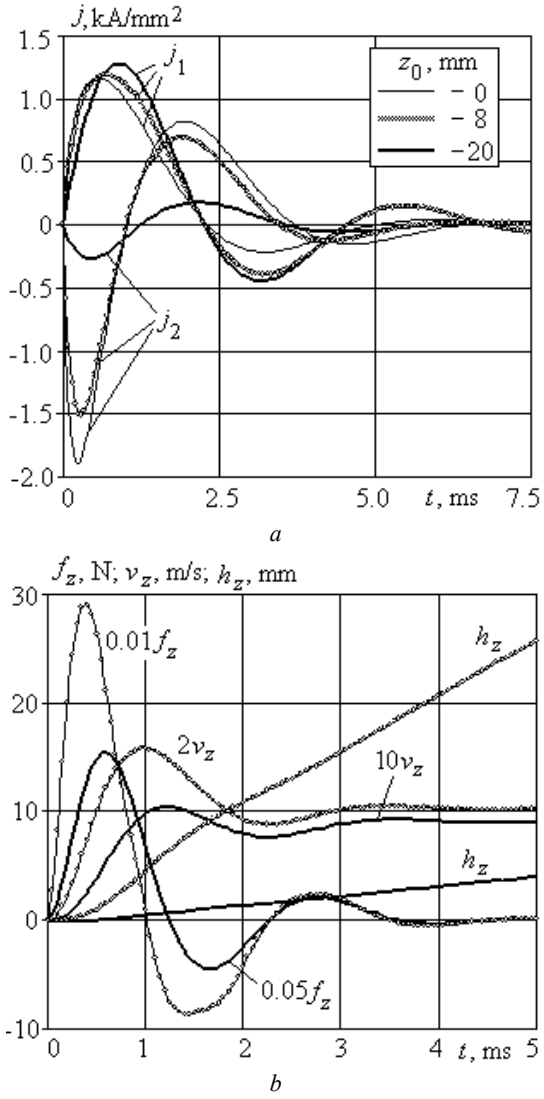

Fig. 3. Electrical (*a*) and mechanical (*b*) characteristics of the EIA at C_0=2500 μF, U_0=707 V

increases to a maximum value v_{zm} = 5.94 m/s, and then decreases by 2.23 times by the end of the electromagnetic process. The displacement of the armature winding h_z nonlinearly increases with time in the active section of acceleration, in which the electrodynamic interaction between the windings occurs. Obviously, the value of displacement h_z is significantly higher at the initial displacement of the windings z_0 = 8 mm than at z_0 = 20 mm. At z_0 = 0 mm, the mechanical indicators of the EIA of the cylindrical configuration are equal to zero. At z_0 = 8 mm, the temperature rise of the inductor winding is θ_1 = 6.3 K, and the temperature rise of the armature winding – θ_2 = 2.4 K.

When using the CES option II, the amplitudes of the current densities in the windings of the EIA increase (Fig. 3,*a*). The largest amplitude of the current density in the inductor winding occurs at the maximum initial displacement z_0 = 20 mm and is j_{1m}=1.28 kA/mm^2. The amplitude of the current density in the armature winding is minimal and amounts to j_{2m}=0.26 A/mm^2. In the absence of displacement (z_0 = 0 mm), the current density in the armature winding is maximum and is j_{2m}= 1.9 kA/mm^2.

The electrodynamic force f_z between the windings also has an initial accelerating and subsequent braking components (Fig. 3,*b*). With an intermediate initial displacement of the windings (z_0 = 6 mm), the amplitude of the accelerating component of the force increases to 2.9 kN. The armature winding speed initially increases to a maximum value of v_{zm} = 7.91 m/s, and then decreases by 1.54 times by the end of the electromagnetic process. At z_0 = 6 mm the temperature rise of the inductor winding is θ_1 = 5.9 K, and the temperature rise of the armature winding – θ_2 = 5.0 K.

Thus, in spite of the shorter force action, the use of a CES with a reduced capacity C_0 and an increased voltage U_0 provides higher speed indicators of an EIA of a cylindrical configuration. However, this is realized with different initial displacement of the windings z_0.

Figure 4 allows to estimate the influence of the initial displacement of the armature winding z_0 on the indicators of the accelerator, excited from the CES. Regardless of the option of the CES, the main dependencies of the EIA are as follows. When using the CES option I and increasing z_0 from 0 to 20 mm, the amplitude of the current density in the inductor winding

increases insignificantly (by 11.2 %), and in the armature winding decreases significantly (6.98 times). As a result, the temperature rise of the inductor winding increases by 19.1 %, and the temperature rise of the armature winding decreases by 32.1 times. However, the amplitude of the electrodynamic force f_{zm} and the speed at the output of the accelerator v_{zf} have pronounced maxima depending on the initial displacement of the windings z_0. The greatest amplitude of the force f_{zm} = 1.72 kN occurs at z_0≈6 mm, and the highest speed v_{zf} = 2.66 m/s – at z_0≈8 mm.

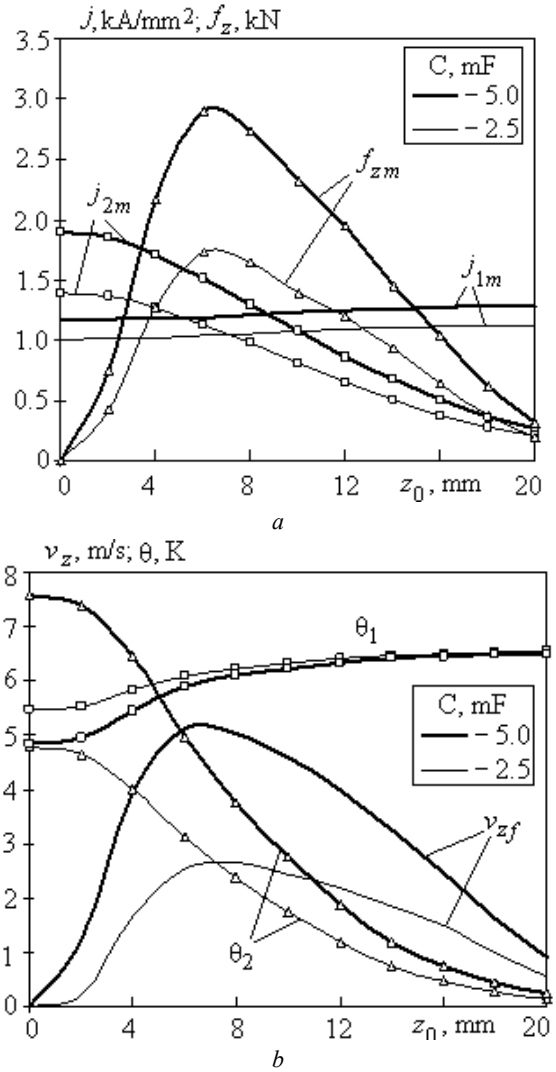

Fig. 4. Dependence of EIA indicators on the initial displacement of the windings when excited from the CES

When the EIA is excited from the CES option II, the amplitudes of the current densities in the windings increase, as do the rises of their temperatures. However, the highest speed v_{zf} = 5.11 m/s takes place at z_0≈6.5 mm.

EIA indicators when excited from an alternating voltage source. Let us consider the excitation of an EIA of a cylindrical configuration when excited from an alternating voltage source. If the AVS has a frequency ν=50 Hz, then a significant phase shift occurs between the currents in the windings at an initial displacement z_0 = 6 mm, leading to the appearance of alternating accelerating and braking components of electrodynamic forces (Fig. 5).

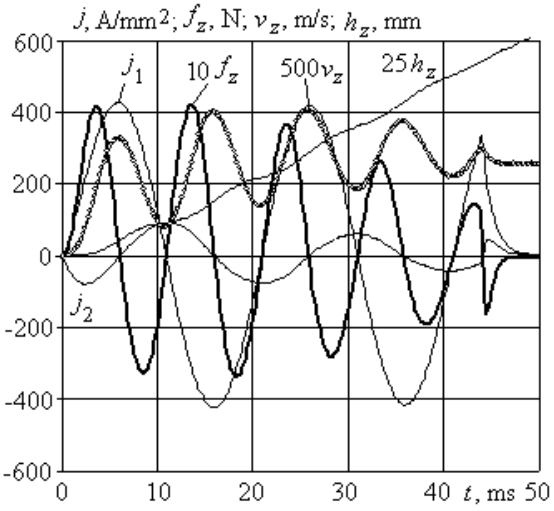

Fig. 5. Electromechanical indicators of the EIA at excitation from the AVS with frequency of 50 Hz at z_0=6 mm

Since the accelerating components of the force prevail over the braking components, the armature winding moves relative to the inductor winding by a distance h_z at a speed v_{zf} = 0.51 m/s. At such a frequency of the AVS, the current amplitude in the armature winding is about 4 times less than in the inductor winding. Moreover, the current density in the armature winding decreases as it moves relative to the inductor winding.

Since the phase shift between the winding currents decreases with an increase in the AVS frequency, the braking component of the electrodynamic force also decreases accordingly. Figure 6 shows the electromechanical indicators of the accelerator at excitation from the AVS with a frequency of 250 Hz at z_0 = 8 mm. With this excitation, in comparison with excitation with a frequency of 50 Hz, the current in the inductor winding decreases, and in the armature winding it increases. In the initial period of excitation, the current densities in the windings are comparable. However, due to a decrease in the magnetic coupling between the windings, the current density in the inductor winding reaches a steady-state value, and in the armature winding it almost completely decays by the end of the excitation period.

But due to the greater displacement of the armature winding relative to the inductor winding, for the same time the magnetic coupling decreases faster, which leads to a stronger damping of the electrodynamic force. This force decays after almost 30 ms. Its accelerating components increase, while the braking ones decrease, which leads to a higher speed at the output of the accelerator v_{zf} =1.9 m/s than at an AVS frequency of 50 Hz.

At the maximum initial displacement between the windings (z_0 = 20 mm), the following changes occur in the electromechanical processes (Fig. 7). With a practically unchanged current density in the inductor winding j_1, the current density in the armature winding j_2 at the initial stage significantly decreases due to the weakened magnetic coupling. However, over time, the current in the armature winding and the electrodynamic

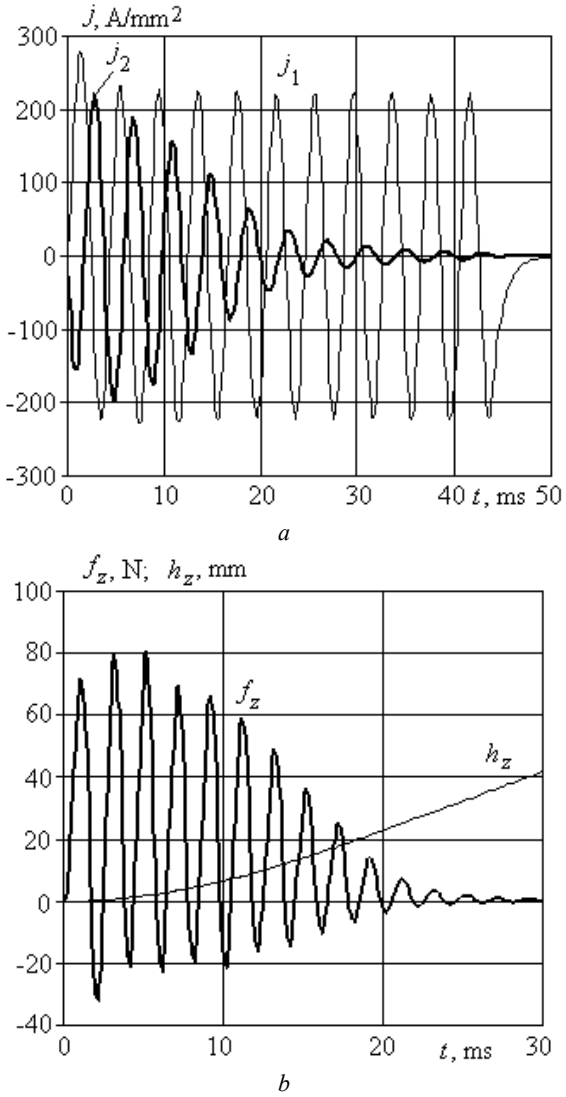

Fig. 6. Electromechanical indicators of the EIA at excitation from the AVS with frequency of 250 Hz at z_0=8 mm

force decay at a lower rate. This is due to the fact that due to the reduced speed v_z, the armature moves a smaller distance relative to the inductor winding.

With an increase in the AVS frequency to 500 Hz, the ratio between the amplitudes of the currents in the windings at the initial stage changes (Fig. 8). The value of the current density in the armature winding exceeds the same value in the inductor winding. In this case, the phase shift between the windings is further reduced. As a result, the braking components of the electrodynamic force decrease, which leads to an increase in the armature speed at the output of the accelerator to v_{zf} = 2.2 m/s, despite a decrease in the accelerating components of the force.

Figure 9 makes it possible to estimate the influence of the initial displacement of the armature winding on the indicators of the EIA of a cylindrical configuration when excited from the AVS.

With an increase in the initial displacement of the armature winding z_0 from 0 to 20 mm, the maximum speed at the output of the accelerator strongly depends on the AVS frequency.

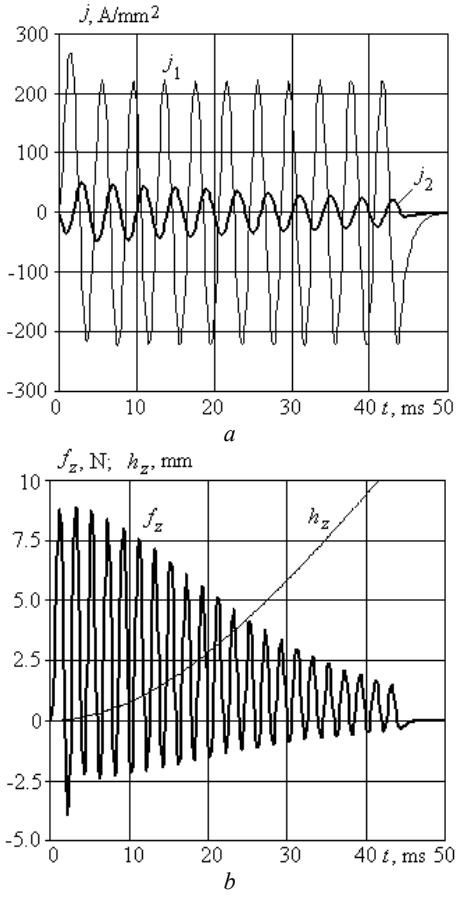

Fig. 7. Electromechanical indicators of the EIA at excitation from the AVS with frequency of 250 Hz at z_0=20 mm

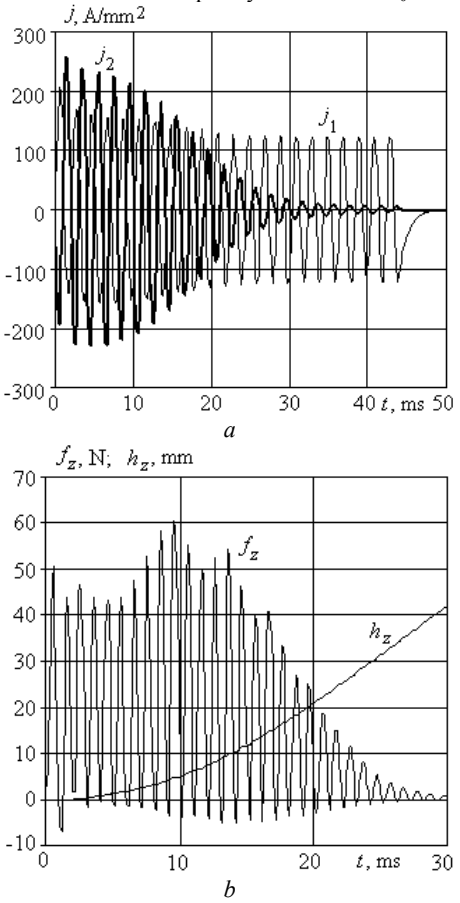

Fig. 8. Electromechanical indicators of the EIA at excitation from the AVS with frequency of 500 Hz at z_0=4 mm

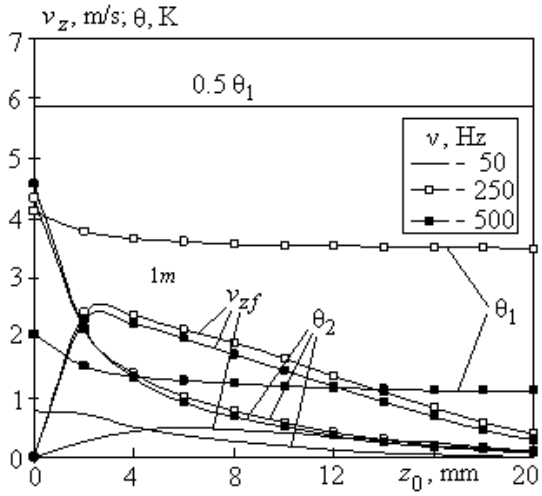

Fig. 9. Dependence of EIA indicators on the initial displacement of the windings when excited from the AVS

At a frequency of 50 Hz, the highest speed at the accelerator output v_{zf} = 0.5 m/s is realized at z_0 = 6.2 mm, at a frequency of 250 Hz – v_{zf} = 2.4 m/s at z_0 = 3.1 mm, and at a frequency of 500 Hz – v_{zf} = 2.29 m/s at z_0 = 2.3 mm. With an increase in the AVS frequency, the temperature rise of the inductor winding θ_1 decreases, and the temperature rise of the armature winding θ_2 increases.

At a frequency of 50 Hz, the value of θ_1 is practically independent on the initial displacement of the windings. However, at higher frequencies, with an increase in the initial displacement, the value θ_1 slightly decreases. The temperature rise of the armature winding θ_2 decreases to a greater extent from the value of z_0 in comparison with the temperature rise of the inductor winding.

Thus, when the EIA is excited from the CES, the initial displacement of the windings should be approximately $z_0 \approx 0.6 z_{0m}$, where z_{0m} is the distance at which the largest dM_{12}/dz value between the windings is ensured. When the EIA is excited from the AVS, the initial displacement z_0 must be selected depending on its frequency: at a frequency of 50 Hz – $z_0 \approx 0.6 z_{0m}$, and at frequencies of 250 Hz and 500 Hz – $z_0 \approx 0.2 z_{0m}$.

Conclusions.

When a cylindrical EIA is excited, the largest amplitude of the current density in the inductor winding occurs at the maximum initial displacement, but the amplitude of the current density in the armature winding is the smallest. The greatest value of the current density in the armature winding occurs in the absence of an initial displacement.

When excited from the CES, the electrodynamic force between the windings has an initial accelerating and subsequent braking components. As a result, the speed of the armature initially increases to a maximum value, but decreases towards the end of the electromagnetic process.

When a cylindrical EIA is excited from the AVS, a phase shift occurs between the currents in the windings, which leads to the appearance of alternating accelerating and breaking components of electrodynamic forces. The accelerating components of the force prevail over the braking components which ensures the displacement of the armature.

At an AVS frequency of 50 Hz, the current amplitude in the armature winding is less than in the inductor winding. With an increase in the AVS frequency to 250 Hz, the phase shift between the winding currents decreases. The current in the inductor winding decreases, and in the armature winding it increases. The accelerating components of the force increase, and the braking ones decrease. With an increase in the AVS frequency to 500 Hz, the value of the current density in the armature winding exceeds the same value in the inductor winding. In this case, the phase shift between the windings is further reduced.

At an AVS frequency of 50 Hz, the highest speed v_{zf} = 0.5 m/s is realized at the initial displacement of the windings z_0 = 6.2 mm, at a frequency of 250 Hz the highest speed v_{zf} = 2.4 m/s is realized at z_0 = 3.1 mm, and at a frequency of 500 Hz, the highest speed v_{zf} = 2.29 m/s is realized at z_0 = 2.3 mm.

Conflict of interest. The authors declare that they have no conflicts of interest.

REFERENCES

1. Guangcheng F., Wang Y., Xu Q., Xinyi N., Yan Z. Design and analysis of a novel three-coil reconnection electromagnetic launcher. *IEEE Transactions on Plasma Science*, 2019, vol. 47, no. 1, pp. 814-820. doi: https://doi.org/10.1109/tps.2018.2874287.

2. Puumala V., Kettunen L. Electromagnetic design of ultrafast electromechanical switches. *IEEE Transactions on Power Delivery*, 2015, vol. 30, no. 3, pp. 1104-1109. doi: https://doi.org/10.1109/tpwrd.2014.2362996.

3. Kostsov E.G. Microelectromechanical accelerator of solids. *Optoelectronics, Instrumentation and Data Processing*, 2012, no. 48, pp. 401-409. doi: https://doi.org/10.3103/S8756699012040115.

4. Reck B. First design study of an electrical catapult for unmanned air vehicles in the several hundred kilogram range. *IEEE Transactions on Magnetics*, 2003, vol. 39, no. 1, pp. 310-313. doi: https://doi.org/10.1109/tmag.2002.805921.

5. Chemeris V.T. Multistage induction accelerator of a macro-object: search for technical solutions. *Artillery and small arms*, 2011, no. 3 (40), pp. 45-51. (Rus).

6. Bolyukh V.F., Shchukin I.S. *Lineinye induktsionno-dinamicheskie preobrazovateli* [Linear induction-dynamic converters]. Saarbrucken, Germany, LAP Lambert Academic Publ., 2014. 496 p. (Rus).

7. Novakovic Z., Vasic Z., Ilic I., Medar N., Stevanovic D. Integration of tactical - medium range UAV and catapult launch system. *Scientific Technical Review*, 2016, vol. 66, no. 4, pp. 22-28. doi: https://doi.org/10.5937/str1604022n.

8. Angquist L., Baudoin A., Norrga S., Nee S., Modeer T. Low-cost ultra-fast DC circuit-breaker: Power electronics integrated with mechanical switchgear. *2018 IEEE International Conference on Industrial Technology (ICIT)*, 2018, pp. 1708-1713. doi: https://doi.org/10.1109/icit.2018.8352439.

9. Gerasimov Yu.V., Karetnikov G.K., Selivanov A.B., Fionov A.S. Evaluation of relative final mass of a nanosatellite delivered to the near-earth space using a pulsed launcher and a pulsed correcting thruster. *Herald of the Bauman Moscow State Technical University. Series Mechanical Engineering*, 2013, no. 3 (92), pp. 69-76. (Rus). Available at: http://vestnikmach.ru/articles/116/eng/116.pdf (accessed 15 May 2021).

10. Upshaw J.L., Kajs J.P. Micrometeoroid impact simulations using a railgun electromagnetic accelerator. *IEEE Transactions on Magnetics*, 1991, vol. 27, no. 1, pp. 607-610. doi: https://doi.org/10.1109/20.101103.

11. Bissal A. *On the design of ultra-fast electro-mechanical actuators. Licentiate Thesis*. Stockholm, Sweden, 2013. 76 p.

Available at: https://www.diva-portal.org/smash/get/diva2:617236/FULLTEXT01.pdf (accessed 15 May 2021).
12. Torlin V.N. Vetrogon A.A., Ogryzkov S.V. Behavior of electronic units and devices under the influence of shock loads in an accident, *Automobile transport*, 2009, vol. 25, pp. 178-180. (Rus). Available at: https://dspace.khadi.kharkov.ua/dspace/bitstream/123456789/807/1/39.pdf (accessed 15 May 2021).
13. Kondratiuk M., Ambroziak L. Concept of the magnetic launcher for medium class unmanned aerial vehicles designed on the basis of numerical calculations, *Journal of Theoretical and Applied Mechanics*, 2016, vol. 54, no. 1, pp. 163-177. doi: https://doi.org/10.15632/jtam-pl.54.1.163.
14. Li S., Gui Y., Yu C., Liu P., Zhang P., Li J. Study on the effect and the direction accuracy of active electromagnetic protection system. *IEEE Transactions on Magnetics*, 2009, vol. 45, no. 1, pp. 351-353. doi: https://doi.org/10.1109/TMAG.2008.2008850.
15. Bolyukh V.F., Oleksenko S.V., Schukin I.S. Efficiency of linear pulse electromechanical converters designed to create impact loads and high speeds. *Electrical Engineering & Electromechanics*, 2015, no. 3, pp. 31-40. doi: https://doi.org/10.20998/2074-272X.2015.3.05.
16. Bolyukh V.F., Shchukin I.S. Influence of an excitation source on the power indicators of a linear pulse electromechanical converter of induction type. *Technical Electrodynamics*, 2021, no. 3, pp. 28-36. doi: https://doi.org/10.15407/techned2021.03.028.
17. Bolyukh V.F., Katkov I.I. Influence of the Form of Pulse of Excitation on the Speed and Power Parameters of the Linear Pulse Electromechanical Converter of the Induction Type. *Volume 2B: Advanced Manufacturing*, Nov. 2019, 8 p. doi: https://doi.org/10.1115/imece2019-10388.
18. Bolyukh V.F., Kashansky Yu.V., Schukin I.S. Features of excitation of a linear electromechanical converter of induction type from an AC source. *Electrical Engineering & Electromechanics*, 2021, no. 1, pp. 3-9. doi: https://doi.org/10.20998/2074-272x.2021.1.01.
19. Bolyukh V.F., Shchukin I.S. The thermal state of an electromechanical induction converter with impact action in the cyclic operation mode, *Russian Electrical Engineering*, 2012, vol. 83, no. 10, pp. 571-576. doi: https://doi.org/10.3103/S1068371212100045.

Received 10.07.2021
Accepted 25.09.2020
Published 26.10.2021

V.F. Bolyukh[1], *Doctor of Technical Science, Professor,*
I.S. Schukin[2], *PhD, Associate Professor,*
J. Lasocki [3], *PhD, Associate Professor,*
[1] National Technical University «Kharkiv Polytechnic Institute»,
2, Kyrpychova Str., Kharkiv, 61002, Ukraine,
e-mail: vfbolyukh@gmail.com (Corresponding author)
[2] Firm Tetra, LTD,
18, Gudanova Str., Kharkiv, 61024, Ukraine,
e-mail: tech@tetra.kharkiv.com.ua
[3] Warsaw University of Technology,
Narbutta 84, 02-524, Warsaw, Poland,
e-mail: jakub.lasocki@pw.edu.pl

How to cite this article:
Bolyukh V.F., Schukin I.S., Lasocki J. Influence of the initial winding displacement on the indicators of the electromechanical induction accelerator of cylindrical configuration. *Electrical Engineering & Electromechanics*, 2021, no. 5, pp. 3-10. doi: https://doi.org/10.20998/2074-272X.2021.5.01.

UDC 621.763: 621.74.047 https://doi.org/10.20998/2074-272X.2021.5.02

P.D. Andrienko, O.V. Nemykina, A.A. Andrienko, R.E. Mokhnach

RESEARCH OF OPERATING MODES OF CONDUCTORS IN POWER SUPPLY SYSTEMS OF CRANES WITH INDUCTION FEED, TAKING INTO ACCOUNT THE INFLUENCE OF HIGHER HARMONICS OF THE CURRENT

Purpose. *Investigation of the influence of higher harmonics of current on current distribution, voltage and power losses in the supply systems of crane trolleys and development of a calculation method for practical use.* ***Methodology.*** *The analytical method and the results of the modeling method were used for research.* ***Results.*** *Analytical relationships have been obtained that make it possible to determine the current distribution, voltage and power losses in the systems of induction feeding of crane trolleys, taking into account the composition and amplitude of the higher harmonics of the current.* ***Originality.*** *For the first time, analytical dependences are obtained that take into account the effect of changing the trolley parameters on the frequency in the feed systems. Numerical values have been determined for the most commonly used induction feed systems for cranes. It is shown that with an increase in the cross-section of the feed bar there is a decrease in the main, and especially additional, losses.* ***Practical value.*** *Theoretical relationships have been obtained that can be used to calculate the optimization of induction feed systems in the presence of higher harmonic currents arising in power systems during operation of crane semiconductor controlled electric drives.* References 13, tables 4, figures 6.

Key words: **induction feed system, trolleys, feed bus, current distribution, power and voltage losses.**

У статті викладена методика розрахунку розподілу струму по струмопроводам, втрат напруги і потужності з урахуванням вищих гармонік струму в системах живлення кранів з індукційним підживленням. Отримані необхідні аналітичні залежності, що пов'язують параметри струмопроводів з відносними значеннями частоти вищих гармонійних і визначають їх вплив на струморозподіл, втрати напруги та потужності. Показано, що зі збільшенням перетину шин підживлення відбувається зниження втрат напруги і додаткових втрат, в тому числі і від струмів вищих гармонік, за рахунок перерозподілу цих струмів і втрат від них в шину подачі, що має практично незалежний від частоти активний опір. Показано, що основна частина додаткових втрат визначається амплітудами гармонік з порядком n≤7. Методика може бути застосована для систем живлення залізничного транспорту і розподільних систем, виконаних з застосуванням сталемідних і сталеалюмінієвих струмопроводів. Бібл. 13, табл. 4, рис. 6.

Ключові слова: **система індукційного живлення, тролея, шина живлення, розподіл струму, втрати потужності та напруги.**

В статье изложена методика расчёта токораспределения по токопроводам, потерь напряжения и мощности с учётом высших гармоник тока в системах питания кранов с индукционной подпиткой. Получены необходимые аналитические зависимости, связующие параметры токопроводов с относительными значениями частоты высших гармонических и определяющие их влияние на токораспределение, потери напряжения и мощности. Показано, что с увеличением сечения шин подпитки происходит снижение потерь напряжения, потерь мощности, в том числе и от токов высших гармоник, за счёт перераспределения этих токов и потерь от них в шину подпитки, обладающей практически независимым от частоты активным сопротивлением. Показано, что основная часть добавочных потерь определяется амплитудами гармоник с порядком n≤7. Методика применима для систем питания железнодорожного транспорта и распределительных систем, выполненных с применением сталемедных и сталеалюминиевых токопроводов. Библ. 13, табл. 4, рис. 6.

Ключевые слова: **система индукционной подпитки, троллея, шина подпитки, токораспределение, потери мощности и напряжения.**

Introduction. Energy saving in electrical networks is a priority area, both worldwide and in Ukraine. The widespread introduction of semiconductor converters leads to an increase in higher harmonics of current and voltage distortion, which increases voltage and power losses in electrical networks and leads to a deterioration in power quality indicators [1-3], and also has a significant impact on the operation of converters connected to these networks [4]. Determination of the composition and amplitude of the higher harmonics of the current is carried out by calculation, experimental and modeling methods [5-9]. To determine the influence of higher current harmonics on the supply network, it is necessary to know the parameters of the equivalent circuit. For low-voltage workshop networks, the values of active and inductive resistances are determined mainly by an analytical method. For complex wired conductor systems containing ferromagnetic elements and protective shields, analytical calculations are difficult. For these cases, modeling methods are used [5, 10].

For the most common and typical circuits, as a rule, analytical methods for calculating voltage and power losses are used [2, 11]. Such circuits include crane installations where variable frequency drives (VFDs) are used when modernizing old ones or designing new ones. The use of VFDs with semiconductor converters in crane power systems leads to a significant content of higher harmonic currents in the supply network, which are taken into account by the total harmonic distortion (THD_I) in accordance with the requirements of the International Standards IEEE 519-1992, IEC 61000-3-12:2012 and IEC 61000-3-12:2004. Higher harmonic currents lead to additional voltage and power losses in shop networks [6]. This circumstance attracts more and more attention to the study of operating modes of nonlinear loads, taking into account the higher harmonics of the current [4-9, 12, 13].

The implementation of the requirements for limiting the generation of higher harmonics in the network required research and development of circuit solutions for

converters, passive active filters [1, 3]. From an economic point of view, the power distortion compensation is carried out at the load nodes: switchgear 6, 10 kV or switchgear 0.4 kV. However, in shop networks supplying electrical receivers with converters, the influence of higher harmonics turns out to be significant [5] and requires its solution.

In [6, 7], the authors proposed a method for studying the influence of higher harmonics of current in power supply systems of crane installations using steel trolleys and aluminum buses for the current conductor. It is shown that the presence of higher harmonics of the current leads to an increase in voltage losses by 3.2–4 times and power losses by 1.26–1.43 times in comparison with sinusoidal current for steel trolleys.

In the power supply system of heavy duty cranes and relatively long working spans, to ensure the operating voltage within the permissible limits, the main trolley is fed. The most widely used induction feed system is the least expensive. With induction feeding, an aluminum bus is usually laid in parallel to the trolleys [11].

The presence of higher harmonics of current in the power supply systems of the cranes leads to a change in the impedances of individual conductors and, accordingly, in the current distribution in them.

The goal of the paper is to investigate the influence of higher harmonics of currents on current distribution, voltage and power losses in the conductors of the induction feed system of cranes, and offer recommendations for reducing losses from higher harmonics.

Main research material.

Initial data. According to the generally accepted technique, the current of the fundamental harmonic of the trolleys I_t is determined from the condition of the permissible voltage losses in the working section of the crane operation, according to the relationship [6, 11]:

$$\begin{cases} I_t = \dfrac{\Delta U_{\max}}{l_t \cdot \Delta U_{t1}} = \dfrac{\Delta U_{\max}}{\sqrt{3} \cdot l_t \cdot R_t \cdot \left(\cos\varphi_1 + \mathrm{tg}\varphi_{t1} \cdot \sin\varphi_1\right)}; \\ I_s = I_{\max} - I_t, \end{cases} \quad (1)$$

where $\Delta U_{\max}$, ΔU_{t1} are the permissible voltage losses and voltage losses per 1 m of trolley section length, respectively, at a given trolley current; l_t is the working length of the trolley; $I_{\max}$, I_s are the maximum current of the system and feed bus, respectively; $\mathrm{tg}\varphi_{t1} = X_{t1}/R_{t1}$; where X_{t1}, R_{t1} are the inductive and active resistance of the trolley for the fundamental harmonic with frequency of 50 Hz; φ_1 is the shift angle of the fundamental harmonic.

To ensure the permissible voltage losses $\Delta U_{\max} \le 5$ %, an aluminum bus is laid parallel to the trolley in the working area of the crane operation. The current distribution along the conductors in the feed system is determined by the ratio of the impedances at the fundamental harmonic [11].

Ratio of currents in conductors using the superposition method for components with harmonic n

$$\gamma_n = \frac{Z_{sn}}{Z_{tn}} = \frac{R_{sn}}{R_{tn}} \cdot \sqrt{\frac{1 + tg^2\varphi_{sn}}{1 + tg^2\varphi_{tn}}}, \quad (2)$$

where $Z_{s(t)n} = \sqrt{R^2_{s(t)n} + X^2_{s(t)n}}$ is the impedance of the corresponding conductor (s – bus, t – trolley) for n harmonic; $X_{tn} = X'_{tn} + X''_{tn} + X'''_{tn}$; $X_{sn} = X'_{sn} + X'''_{sn}$ is the inductive resistance: X' – internal; X'' – external; X''' is the resistance to mutual inductance of the trolley and the feed bus.

The parameters of the conductors of the most common induction feed systems are given in Table 1 for distance between trolleys of 250 mm, made with a corner of 50 × 50 × 5 mm.

The inductive resistance of the conductors is indicated taking into account the mutual inductance of the trolley and the feed bus [11].

Table 1

Parameters of conductors of feed systems

Dimensions, mm	Parameters						
Steel corner 50×50×5 mm	R_{t1}, Ω/km	X_{t1}, Ω/km	Z_{t1}, Ω/km	$X'_{t1} + X'''_{t1}$, Ω/km	X''_{t1}, Ω/km	$\mathrm{tg}\varphi_{t1}$	γ_1, p.u.
	1,65	1,263	2,08	0,339	0,924	0,765	
Aluminum bus	R_{s1}, Ω/km	X_{s1}, Ω/km	Z_{s1}, Ω/km	—	—	$\mathrm{tg}\varphi_{s1}$	
20×3	0,513	0,277	0,583	—	—	0,54	0,28
30×3	0,342	0,253	0,425	—	—	0,74	0,204
40×3	0,256	0,237	0,348	—	—	0,926	0,161
50×3	0,205	0,225	0,32	—	—	0,11	0,147
60×4	0,128	0,213	0,248	—	—	1,664	0,119
80×5	0,077	0,195	0,21	—	—	2,53	0,101

The most common sources of higher harmonics are uncontrolled (for variable frequency drives) and controlled (for DC drives) rectifiers. The relative values of the n-order harmonics of the input current of the bridge rectifier are determined from the relationship:

$$I_n^* = K_n \cdot \frac{I_n}{I_1} = K_n \cdot \frac{1}{n} = K_n \cdot \frac{1}{f_n^*}, \quad (3)$$

where K_n is the coefficient that takes into account the ratio of the ripple amplitude in a real rectifier to an ideal one [6] (with inductance L_d in the rectifier link $L_d = \infty$ $K_n = 1$); I_n, I_1 are the current values of the n-order harmonic and fundamental harmonic in current conductors, respectively; $f_n^* = f_n$ / 50 is the relative frequency of the n-order harmonic.

In [6] it was shown that the resistance of aluminum buses is related by the following ratios for the n harmonic component relative to the main one:

$$\begin{cases} R_{sn} = R_{s1}; \quad X_{sn} = X_{s1} f_n^*; \\ \mathrm{tg}\varphi_{sn} = \dfrac{X_{sn}}{R_{sn}} = \mathrm{tg}\varphi_{s1} f_n^*. \end{cases} \tag{4}$$

The resistance of the steel corners is related by the ratios for the n harmonic component relative to the main one:

$$\begin{cases} R_{tn} = R_{t1}\sqrt{f_n^*}; \quad X_{tn} = \left(X'_{t1} + X''_{t1} + X'''_{t1}\right) f_n^*; \\ \mathrm{tg}\varphi_{tn} = \dfrac{X_{tn}}{R_{tn}} = \dfrac{\left(X'_{t1} + 0{,}56R_{t1}\sqrt{f_n^*} + X'''_{t1}\right)\sqrt{f_n^*}}{R_{t1}}. \end{cases} \tag{5}$$

The maximum current taking into account higher harmonics is determined by the relationship [2, 6]

$$I_{\max}^* = \sqrt{\sum_{k=0}^{n=6k\pm1} K_n^2 I_n^{*2}} = \sqrt{\sum_{k=0}^{n=6k\pm1} K_n^2 \frac{1}{f_n^{*2}}}, \tag{6}$$

where k is the series of integers 1, 2, 3, etc. In this case, we assume that the fundamental harmonic is equal to the fundamental harmonic of the sinusoidal current of the trolley without feed.

Research results.

1. Distribution of currents in the feed conductors. Transforming expression (2), taking into account the considered relations (3), we have:

$$\gamma_n = \frac{R_{s1}}{R_{t1}\sqrt{f_n^*}} \sqrt{\frac{1 + \left(\mathrm{tg}\varphi_{s1} f_n^*\right)^2}{1 + \dfrac{\left(X'_{t1} + 0{,}56R_{t1}\sqrt{f_n^*} + X'''_{t1}\right)^2 f_n^*}{R_{t1}^2}}}. \tag{7}$$

Analysis of the relationship (7), taking into account the values of the parameters for calculating the conductors, summarized in Table 1 showed that for $f_n^* \geq 7$, relationship (7) with sufficient accuracy can be reduced to the form:

$$\gamma_n = \frac{X_{s1}}{0{,}56R_{t1}\sqrt{f_n^*}}. \tag{8}$$

Thus, the distribution of currents along the conductors is practically directly proportional to the inductive resistance of the feed buses at the fundamental harmonic and inversely proportional to the square root of the frequency f_n^*, i.e. with increasing frequency, γ_n decreases monotonically, which indicates an increase in high-frequency components in the feed bus (Fig. 1).

It is not difficult to show, using the second equation in expression (1) and relation (2), that the relative value of the bus current I_{sn}^* and trolley current I_{tn}^* for the n harmonic component has the form:

$$\begin{cases} I_{sn}^* = \dfrac{I_{sn}}{I_{\max}} = \dfrac{1}{1+\gamma_n} \cdot \dfrac{1}{f_n^*}; \\ I_{tn}^* = \dfrac{I_{tn}}{I_{\max}} = \dfrac{\gamma_n}{1+\gamma_n} \cdot \dfrac{1}{f_n^*}. \end{cases} \tag{9}$$

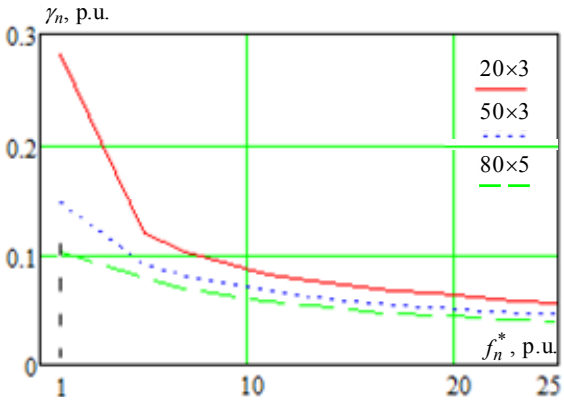

Fig. 1. Dependences $\gamma_n = f(f_n^*)$ for the steel corner 50×50×5 mm with feed bus 20×3, 50×3, 80×5 mm

Figure 2 shows the relative values of the currents in the induction feed system: a corner 50 × 50 × 5 mm with a feed bus 80 × 5 mm for the n harmonic component.

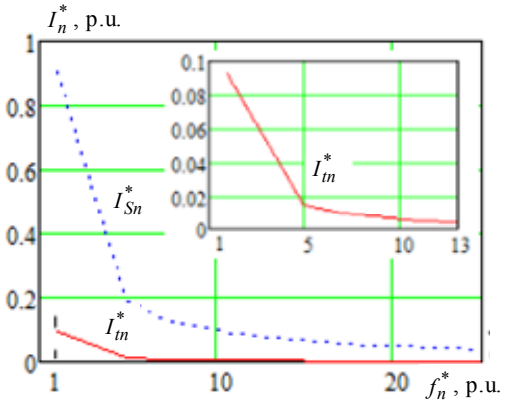

Fig. 2. Dependences $I_n^* = f(f_n^*)$ for the steel corner 50×50×5 mm with feed bus 80×5 mm

Table 2 shows the relative values of the currents in the trolley made of a corner 50 × 50 × 5 mm with a feed bus.

Table 2

Relative values of currents

Bus sizes, mm	Parameter					
	I_{s1}^*, p.u.	$I_{s\Sigma}^*$, p.u.	$I_{sn\Sigma}^*$, $n\geq5$, p.u.	I_{t1}^*, p.u.	$I_{t\Sigma}^*$, p.u.	$I_{tn\Sigma}^*$, $n\geq5$, p.u.
20×3	0,781	0,819	0,024	0,219	0,221	0,026
50×3	0,872	0,908	0,252	0,128	0,13	0,021
80×5	0,908	0,943	0,255	0,092	0,094	0,018

Analysis of Table 2 shows that with an increase in the cross-section of the feed bus, the current of the trolleys $I_{t\Sigma}^*$ significantly decreases including the decrease in the high-frequency component $I_{tn\Sigma}^*$.

2. Voltage losses.

Since the trolleys are selected according to the permissible voltage losses at a given current (1), then we check the influence of higher harmonics for the trolleys.

In the presence of higher harmonics, the relative increase in voltage losses in trolleys relative to the voltage losses at the fundamental harmonic ΔU_{t1} is determined taking into account expressions (1), (9):

$$\Delta U_t^* = \frac{\sqrt{\Delta U_{t1}^2 + \Delta U_{t5}^2 + ... + \Delta U_{t13}^2}}{\Delta U_{t1}} = \sqrt{\sum_{k=0}^{n=6k\pm1} \Delta U_{tn}^{*2}} = \sqrt{1 + \sum_{k=1}^{n=6k\pm1} K_n^* \frac{1}{f_n^*} \left(\frac{\gamma_n}{1+\gamma_n}\right)^2 \left(\frac{1+\gamma_1}{\gamma_1}\right)^2 \frac{\left(\cos\varphi_1 + \mathrm{tg}\varphi_{t1} f_n^* \sin\varphi_1\right)^2}{\left(\cos\varphi_1 + \mathrm{tg}\varphi_{t1} \sin\varphi_1\right)^2}}, \quad (10)$$

where $\Delta U_{t1} = \dfrac{\sqrt{3} I_{t1} R_{t1} l_t \left(\cos\varphi_1 + \mathrm{tg}\varphi_{t1} \sin\varphi_1\right)}{U_{\text{nom}}} \cdot 100\%$;

$I_{t1} = I_{\max}\left(\dfrac{\gamma_1}{1+\gamma_1}\right)$; $\mathrm{tg}\varphi_{t1} = X'_{t1} + 0{,}56R_{t1} + X'''_{t1}$;

U_{nom} is the trolley rated voltage.

For the case of an ideal uncontrolled rectifier $K_n = 1$, $\cos\varphi_1 \approx 1$ which corresponds to a rectifier with an LC filter (distortion factor $\nu = 0.955$ which corresponds to $THD_I = 31.05$ %)), the voltage losses are:

$$\Delta U_t^* = \sqrt{1 + \sum_{k=1}^{n=6k\pm1} \frac{1}{f_n^*} \left(\frac{\gamma_n}{1+\gamma_n}\right)^2 \left(\frac{1+\gamma_1}{\gamma_1}\right)^2}. \quad (11)$$

The dependence of the relative values of voltage losses in the trolley with a feed bus as a function of frequency f_n^* are shown in Fig. 3.

The relative values of ΔU_{t5}^* and ΔU_{t7}^* are about 22 % and 16 % of the voltage losses at the fundamental harmonic, and the relative values of ΔU_{t11}^* and ΔU_{t25}^* are 10 % and 5 %, respectively.

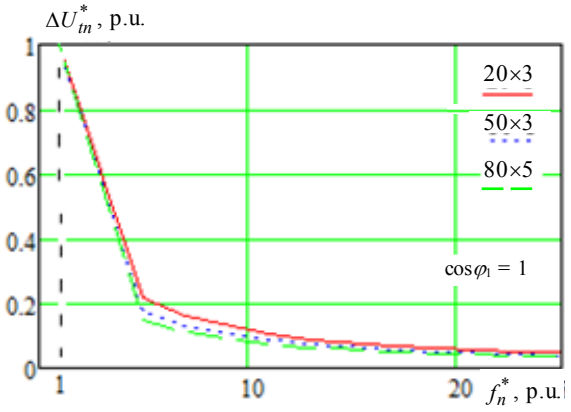

Fig. 3. Dependences $\Delta U_{tn}^* = f(f_n^*)$ in the trolley with feed bus 20×3, 50×3, 80×5 mm; $\cos\varphi_1 = 1$

The dependence of the relative values of the voltage losses in the trolley with feed bus on the frequency is shown in Fig. 4 at $\cos\varphi_1 = 0.5$.

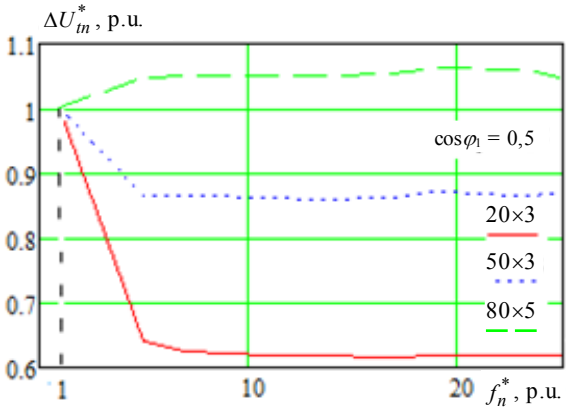

Fig. 4. Dependences $\Delta U_{tn}^* = f(f_n^*)$ in the trolley with feed bus 20×3, 50×3, 80×5 mm; $\cos\varphi_1 = 0.5$

As follows from Fig. 4, the relative values of the voltage losses ΔU_{tn}^* for $n \geq 5$ harmonic components at $\cos\varphi_1 = 0.5$ increase significantly which is explained by the influence of the component $(\cos\varphi_1 + \mathrm{tg}\varphi_{t1} \cdot f_n^* \cdot \sin\varphi_1)$ in expression (10). An increase in ΔU_{tn}^* is noted for $n \geq 5$ with an increase in the cross-section of the feed bus which is caused by the redistribution of the ratio of the relative values of the currents of the fundamental harmonic of the trolley I_{t1}^* and high-frequency components $I_{tn\Sigma}^*$. This ratio increases as the cross-section of the feed bus decreases.

Table 3 shows the relative values of the voltage losses in the trolley at $\cos\varphi_1$ = var, made of the corner 50 × 50 × 5 mm for some combinations of feed at $f_n^* \leq 25$.

Table 3

Relative value of voltage losses

bus, mm / $\cos\varphi_1$	20×3	50×3	80×5
1	1,051	1,033	1,025
0,9	1,36	1,63	2,081
0,8	1,54	1,91	2,31
0,7	1,69	2,16	2,53
0,6	1,853	2,39	2,83
0,5	2,022	2,65	3,14

Analysis of Table 3 shows that the relative value of the voltage losses of the corner at $\cos\varphi_1 = 1$ with 20 × 3 mm bus increases by 5.1 %, and with 80 × 5 mm bus – by 2.5 %. The relative value of the voltage losses reaches its maximum value at $\cos\varphi_1 = 0.5$: with 20 × 3 mm bus it increases by 2.022 times, and with 80 × 5 mm bus – by 3.1 times. Therefore, $\Delta U_{\max}$ in expression (1) should be reduced by an appropriate value.

Dependences $\Delta U_t^* = f(\cos\varphi_1)$ in the trolley with feed bus are shown in Fig. 5.

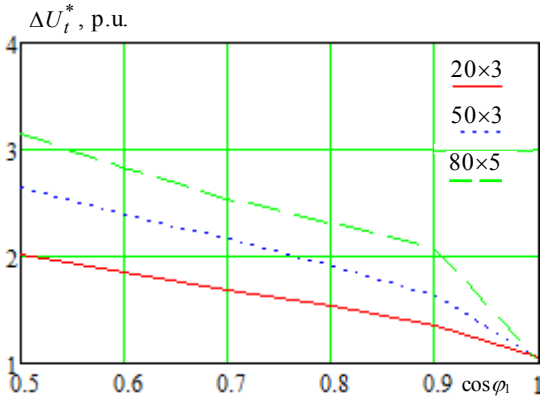

Fig. 5. Dependences $\Delta U_t^* = f(\cos\varphi_1)$ in the trolley with feed bus 20×3, 50×3, 80×5 mm

An analysis of the dependence $\Delta U_t^* = f(\cos\varphi_1)$ for the trolley with feed bus shows that with a decrease in $\cos\varphi_1$, the values of the relative voltage losses in the trolley increase with an increase in the cross-section of the feed bus.

Note that the relative value of the voltage losses in the trolley with feed bus, depending on $\cos\varphi_1$, is lower in the same trolley without feed bus in the presence of higher harmonics [6].

3. Power losses.

Power losses in the induction feed system have two components: losses in the trolley ΔP_t and in the feed bus ΔP_s which are equal, respectively:

$$\Delta P_t = 3\cdot \sum_{k=0}^{n=6k\pm1} R_{tn} I_{tn}^2 \quad \text{and} \quad \Delta P_s = 3\cdot \sum_{k=0}^{n=6k\pm1} R_{s1} I_{sn}^2 .$$

In relative units, power losses are determined taking into account expressions (1), (5), (9):

$$\Delta P^* = \Delta P_t^* + \Delta P_s^* = \frac{\Delta P_t + \Delta P_s}{\Delta P_1} = \\ = \sum_{k=0}^{n=6k\pm1} K_n^2 \frac{\sqrt{f_n^*}}{f_n^{*2}} \left(\frac{\gamma_n}{1+\gamma_n}\right)^2 + \frac{R_{s1}}{R_{t1}} \sum_{k=0}^{n=6k\pm1} \left(\frac{1}{1+\gamma_n}\right)^2 \frac{K_n^2}{f_n^{*2}}, \quad (12)$$

where $\Delta P_1 = 3R_{t1}I_{t1}^2$ are the losses in trolleys without feed.

The relative values of the power losses in the induction feed system are shown in Fig. 6.

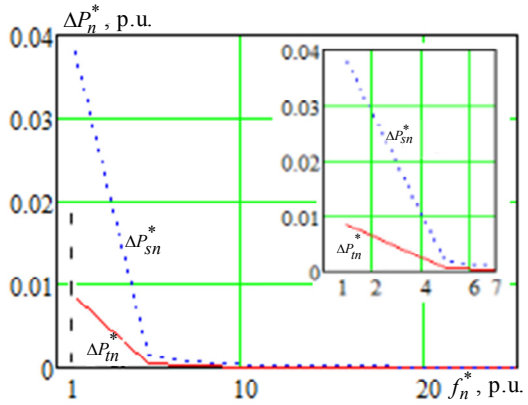

Fig. 6. Dependences $\Delta P_n^* = f(f_n^*)$ in the trolley with feed bus 80×5 mm

The relative values of power losses in the trolley with feed bus for an ideal uncontrolled rectifier $K_n = 1$ are summarized in Table 4.

Table 4

Relative values of power losses

Bus sizes, mm	Parameter, p.u.						
	ΔP_{t1}^*	$\Delta P_{tn\Sigma}^*$, $n\geq5$	ΔP_t^*	ΔP_{s1}^*	$\Delta P_{sn\Sigma}^*$, $n\geq5$	ΔP_s^*	ΔP^*
20×3	0,048	0,0018	0,0498	0,189	0,012	0,2	0,248
50×3	0,016	0,0007	0,0167	0,118	0,0061	0,118	0,135
80×5	0,0084	0,00044	0,00884	0,038	0,0018	0,039	0,047

Analysis of Table 4 shows that relative to the first harmonic of the system current, the power losses in the induction feed systems ΔP^* decrease depending on the cross-section of the feed buses by 4; 7.4 and 21.3 times, respectively. In this case, the relative additional power losses ($\Delta P_{tn\Sigma}^* + \Delta P_{sn\Sigma}^*$) are 5.5–4.6 % of the total losses.

Analysis of losses from high-frequency components shows that the main share of additional losses is losses from harmonics $n\leq7$. Accounting of the coefficient K_n^2, according to [6], leads to an increase in additional losses by about 1.5 times. Therefore, the calculation of the losses should be made taking into account the real values of the higher harmonics obtained experimentally [8] or by modeling [6].

Note that in order to reduce voltage and power losses in systems with crane installations that operate in heavy duty with a large number of starts, relatively expensive non-inductive feed systems are used, in which the feed bus is made of aluminum wires laid in pipes [11]. Analysis of these feed systems shows that with cross-section of wires of 50–150 mm^2 and with number of cores equal to 3, the inductive resistances decrease by 2–3 times. This leads, according to expression (12), to a decrease in additional voltage and power losses in the trolleys. This circumstance partially or completely compensates the primary capital costs for building a non-inductive feed system, which are determined by a technical and economic calculation.

The proposed technique for calculating voltage and power losses can be used to calculate voltage and power losses in steel-copper and steel-aluminum wires used in railway transport and distribution networks.

A feature of AC power supply systems in railway transport is the significant value of the currents of the 3rd and the 5th harmonics, which reach 60 and 30 % of the fundamental one, respectively [13] which significantly affects the distribution of currents and the value of additional power losses and voltage losses.

Conclusions.

Research results show that in induction feed systems, due to the redistribution of higher harmonic currents between the feed bus and the trolley, there is a decrease in voltage losses, main and additional power losses.

When determining the permissible voltage losses, the reduction factor of the value of the permissible voltage losses 1.051–1.025, and 2.022–3.14 should be used, depending on the change in the power factor in the range of $\cos\varphi_1$ = 1.0–0.5 and depending on the cross-section of the feed buses, respectively.

The use of an induction feed system allows to reduce the total power losses by 4–21.3 times depending on the cross-section while the relative additional power losses are no more than 5.5 % of the total power losses.

The proposed technique for calculating current distribution, voltage losses and power losses can be used to calculate the modes of steel-aluminum and steel-copper conductors.

Conflict of interests. The authors declare no conflicts of interest.

REFERENCES

1. Lumbreras D., Gálvez E., Collado A., Zaragoza J. Trends in power quality, harmonic mitigation and standards for light and heavy industries: a review. *Energies*, 2020, vol. 13, no. 21, p. 5792. doi: https://doi.org/10.3390/en13215792.

2. Zhezhelenko I.V., Saenko Yu.L. *Pokazateli kachestva i ih kontrol na promyishlennyih predpriyatiyah* [Quality indicators and their control at industrial enterprises]. Moscow, Energoatomizdat Publ., 2000. 252 p. (Rus).

3. Kalair A., Abas N., Kalair A.R., Saleem Z., Khan N. Review of harmonic analysis, modeling and mitigation techniques. *Renewable and Sustainable Energy Reviews*, 2017, vol. 78, pp. 1152-1187. doi: https://doi.org/10.1016/j.rser.2017.04.121.

4. Egorov A.N., Kharitonov Y.S., Shevchuk V.A., Semenov A.S. Influence of high harmonics on a frequency converter operation in underground mining. *Bulletin of the Tomsk Polytechnic University. Geo Assets Engineering*, 2020, vol. 331, no. 6, pp. 141-151. (Rus). doi: https://doi.org/10.18799/24131830/2020/6/2683.

5. Zmieva K.A. Modeling of an industrial enterprise power supply system using direct current. *Russian Electrical Engineering*, 2015, vol. 86, no. 5, pp. 239-245. doi: https://doi.org/10.3103/s1068371215050120.

6. Andrienko P.D., Nemykina O.V., Andrienko A.A. High current harmonics influence on the choice of conductors of crane power supply systems. *Electrical Engineering & Electromechanics*, 2019, no. 3, pp. 24-29. doi: https://doi.org/10.20998/2074-272x.2019.3.04.

7. Andrienko P.D., Nemykina O.V., Andrienko A.A. Comparative analysis of crane electrotechnical complexes. *Bulletin of NTU "KhPI". Series: Problems of Electrical Machines and Apparatus Perfection. The Theory and Practice*, 2019, no. 2, pp. 3-7. (Rus). doi: https://doi.org/10.20998/2079-3944.2019.2.01.

8. Proykov M., Simeonova N. Investigation of the influence of current harmonics generated by crane systems on some parameters of the power supply systems. *2021 17th Conference on Electrical Machines, Drives and Power Systems (ELMA)*, 2021, pp. 1-4. doi: https://doi.org/10.1109/elma52514.2021.9503048.

9. Semenov A.S., Semenova M.N., Fedorov O.V. The results of the implementation of the system for monitoring the quality of electricity in mining enterprises. *2019 1st International Conference on Control Systems, Mathematical Modelling, Automation and Energy Efficiency (SUMMA)*, 2019, pp. 644-649. doi: https://doi.org/10.1109/summa48161.2019.8947601.

10. Milykh V.I., Polyakova N.V. Determination of electromagnetic parameters and phase relations in turbo-generators by the automated calculation of the magnetic field in the software environment FEMM. *Electrical Engineering & Electromechanics*, 2016, no. 1, pp. 26-32. doi: https://doi.org/10.20998/2074-272X.2016.1.05.

11. Benerman V.I., Lovtskii N.N. *Proektirovanie silovogo elektrooborudovaniia promyshlennykh predpriiatii* [Design of power electrical equipment for industrial enterprises]. Moscow-Leningrad, GEI Publ., 1960. 385 p. (Rus).

12. Shevyrev Y.V., Pichuev A.V., Shevyreva N.Y. Improving energy performance in networks with semiconductor converters. *2019 International Conference on Industrial Engineering, Applications and Manufacturing (ICIEAM)*, 2019, pp. 1-6. doi: https://doi.org/10.1109/icieam.2019.8743020.

13. Sychenko V.H., Kuznetsov V.H., Bosyi D.O., Sablin O.I. *Enerhetyka tiahovykh merezh* [Power engineering of traction networks]. Dnipro, Standart-Servis Publ., 2017. 210 p. (Ukr). doi: https://doi.org/10.15802/978-617-73-82-04-0.

Received 11.07.2021
Accepted 23.09.2020
Published 26.10.2021

P.D. Andrienko[1], *Doctor of Technical Science, Professor,*
O.V. Nemykina[1], *PhD, Associate Professor,*
A.A. Andrienko[1], *Postgraduate Student,*
R.E. Mokhnach[1],
[1] Zaporizhzhia Polytechnic National University,
64, Zhukovsky Str., Zaporizhzhia, Ukraine, 69063,
e-mail: andrpd@ukr.net (Corresponding author),
olganemikina@ukr.net,
vamoseandrey@mail.ru,
etkmpk@gmail.com

How to cite this article:
Andrienko P.D., Nemykina O.V., Andrienko A.A., Mokhnach R.E. Research of operating modes of conductors in power supply systems of cranes with induction feed, taking into account the influence of higher harmonics of the current. *Electrical Engineering & Electromechanics*, 2021, no. 5, pp. 11-16. doi: https://doi.org/10.20998/2074-272X.2021.5.02.

UDC 621.3.07 https://doi.org/10.20998/2074-272X.2021.5.03

Z.A. Gulshan, M.Z.H. Ali, M.S. Shah, D. Nouman, M. Anwar, M.F. Ullah

A ROBUST CONTROL DESIGN APPROACH FOR ALTITUDE CONTROL AND TRAJECTORY TRACKING OF A QUADROTOR

Introduction. *Unmanned aerial vehicles as quadcopters, twin rotors, fixed-wing crafts, and helicopters are being used in many applications these days. Control approaches applied on the quadrotor after decoupling the model or separate altitude control and trajectory tracking have been reported in the literature. A robust linear H_∞ controller has been designed for both altitude control and circular trajectory tracking at the desired altitude.* ***Problem.*** *The ability of the quadrotor system to hover at a certain height and track any desired trajectory makes their use in many industrial applications in both military and civil applications. Once a controller has been designed, it may not be able to maintain the desired performance in practical scenarios, i.e. in presence of wind gusts.* ***Originality.*** *This work presents the control strategy to ensure both altitude control and trajectory tracking using a single controller.* ***Purpose.*** *However, there is a need for a single controller that ensures both altitude control and trajectory tracking.* ***Novelty.*** *This paper presents a robust H_∞ control for altitude control and trajectory tracking for a six degree of freedom of unmanned aerial vehicles quadrotor.* ***Methodology.*** *Multi input multi output robust H_∞ controller has been proposed for the quadrotor for altitude control and tracking the desired reference. For the controller validation, a simulation environment is developed in which a 3D trajectory is tracked by the proposed control methodology.* ***Results.*** *Simulation results depict that the controller is efficient enough to achieve the desired objective at minimal control efforts.* ***Practical value.*** *To verify that the proposed approach is able to ensure stability, altitude control, and trajectory tracking under practical situations, the performance of the proposed control is tested in presence of wind gusts. The ability of the controller to cater to the disturbances within fractions of seconds and maintaining both transient and steady-state performance proves the effectiveness of the controller.* References 16, table 1, figures 9.

Key words: ***H_∞* controller, six degree of freedom quadrotor, unmanned aerial vehicle, attitude regulation, nonlinear system, robust control.**

Вступ. *Безпілотні літальні апарати, такі як квадрокоптери, двороторні апарати, апарати з нерухомими крилами та гелікоптери сьогодні використовуються у багатьох сферах застосування. У літературі повідомляється про підходи до керування, застосовані на квадрокоптері після від'єднання моделі або окремого контролю висоти та відстеження траєкторії. Надійний лінійний регулятор H_∞ був розроблений як для контролю висоти, так і для відстеження кругової траєкторії на потрібній висоті.* ***Проблема.*** *Здатність квадрокоптерної системи зависати на певній висоті та відстежувати будь-яку бажану траєкторію робить їх застосування можливим у багатьох сферах як у військових, так і в цивільних цілях. Розроблений контролер може не підтримувати бажані характеристики у реальних умовах, тобто за наявності поривів вітру.* ***Оригінальність.*** *У цій роботі представлена стратегія керування, яка забезпечує як контроль висоти, так і відстеження траєкторії за допомогою одного контролера.* ***Мета.*** *Однак існує потреба в єдиному контролері, який забезпечує як контроль висоти, так і відстеження траєкторії.* ***Новизна.*** *У цій статті представлено надійний регулятор H_∞ для контролю висоти та відстеження траєкторії для шести ступенів свободи безпілотних літальних апаратів.* ***Методологія.*** *Для квадрокоптера запропоновано багатовхідний багатовихідний надійний контролер H_∞ для контролю висоти та відстеження бажаного курсу. Для перевірки контролера розробляється середовище моделювання, в якому тривимірна траєкторія відстежується за запропонованою методологією керування.* ***Результати.*** *Результати моделювання показують, що контролер є досить ефективним для досягнення бажаної мети при мінімальних зусиллях контролю.* ***Практична цінність.*** *Щоб переконатися, що запропонований підхід здатний забезпечити стабільність, контроль висоти та відстеження траєкторії в реальних ситуаціях, параметри запропонованого контролю перевіряються за наявності поривів вітру. Здатність контролера усувати порушення протягом кількох секунд і підтримувати як перехідні, так і стабільні показники доводить ефективність контролера.* Бібл. 16, табл. 1, рис. 9.

Ключові слова: ***H_∞* контролер, квадрокоптер з шістьма ступенями свободи, безпілотний літальний апарат, регулювання позиції, нелінійна система, надійне керування.**

1. Introduction. Unmanned Arial Vehicles (UAV) like fixed wing crafts, quadcopters, and helicopters have found applications in several domains [1]. Amongst these, quadcopters and helicopters are commonly used as UAVs due to their hovering ability. These systems possess nonlinear and coupled dynamics, which leads to the challenges in their autonomous control. The dynamics of helicopter can be approximated by a laboratory setup namely Twin Rotor Aerodynamic System (TRAS) [2]. Like helicopter, TRAS has two rotors main and tail rotors. Though in helicopter, main rotor is able to tilt in order to execute forward motion [3].

Control design for UAVs is a difficult task because of the coupling and nonlinearities involved in their mathematical models. In autonomous applications, trajectory tracking is one of the most basic and important tasks. Other equally important scenarios involve e.g., hover control. In [4], four independent proportional–integral–derivative (PID) controllers with independent inputs for control have been designed to achieve the objective of trajectory tracking. Here, real value type genetic algorithm has been used to tune the controller parameters in order to reduce total error and control efficiency. System performance index is used as a fitness function here. In [5], hover control problem is addressed by a control structure that involves feedback and feed forward control. Four impulse input shaper is used for feed forward and PID controller with acceleration feedback input is used for the tracking controller. In [6], robust PID based dead beat control scheme is proposed. As PID controller does not contain the model information, so for small dynamic systems, it performs reasonably well but for higher order system it may lead to oscillations. To

counter these problems, different model-based controllers have been reported in the literature. In [7] an linear–quadratic regulator (LQR) controller is designed. In [8], an integral sliding mode controller using necessary and sufficient conditions has been proposed for the uncertainty handling and trajectory tracking of the quadrotor. A nonlinear PID control strategy is discussed in [9] for the trajectory tracking of the quadrotor. The method proposed here is a novel contribution of nonlinearity in the conventional PID controller based on frequency domain design. A model free control approach is used in [10] for the quadrotor trajectory tracking. Control structure adopted here is based on the internal-external-control-loop structure. Controller uses the conventional sliding mode approach for control effort generation. A super twisting slide mode approach has been used in [11] for trajectory tracking with the nonlinear sliding surface. Experimental validation of the proposed control architecture has also been included. A neural network based self-tuning control structure using double derivative action with proportional control is proposed in [12] for trajectory tracking of the quadrotor UAV. Fractional slide mode control is also proposed for the quadrotor in [13].

The single-input single-output (SISO) linear time invariant (LTI) controllers like proportional–derivative (PD), proportional–integral (PI) and PID require the decoupling of the multi-input multi-output (MIMO) model of the quadrotor which takes the extra computational effort, i.e. one needs to design a de-coupler to obtain multiple SISO models from a single MIMO model of the quadrotor and then design the SISO controller for each model. This may also cause slowing the closed-loop response of the system when connected with hardware and thus can be resulted in an increased control effort and poor tracking. However, the MIMO LTI controllers like LQR, Linear Quadratic Gaussian (LQG), and H_∞ controllers tend to have a larger control effort while trajectory tracking for a quadrotor.

Nonlinear controllers on the other hand require that the desired trajectory be twice differentiable, i.e. 1st and 2nd derivatives of the reference trajectory are required to design the nonlinear controller like slide mode, flatness based, backstepping, twisted slide mode and twisted backstepping controllers. Thus, in case of a fast-changing input trajectory, i.e. reference trajectory with the sharp edges, the value of its 1st and 2nd derivatives become sufficiently high leading to the instability of the closed-loop system. So, the controller designed using these approaches ensures the trajectory tracking only for the smooth reference trajectories and hence the tracking of a circular trajectory, even in 3D is possible with these nonlinear approaches is possible. But the trajectories with sharp edges, i.e. square and triangular trajectories can't be tracked. Also, the nonlinear controller based the system dynamics has the equal computational complexity to that of its nonlinear model and thus for the high nonlinear and more complex system like quadrotor, the computational complexity is increased which may cause slowing the closed-loop response when connected to the hardware for experiments. While the nonlinear controller designed through heuristic and intuitional approaches like neural network and fuzzy logic, one needs to have the complete information and knowledge about the system behavior and design the set of rules to design a controller ensuring the desired performance. One drawback of using these approaches is once the designer misinterprets the system behavior, intentionally or unintentionally, the resulting controller will lead the instability of the closed system. So, one need to have complete information about the system and consider all the ambiguities, disturbances in each operating zone, and understand the system performance under every possible condition. This requires a lot of experience and experimentation.

Aim and objectives of the paper. Motivated by the issue mentioned above a single multi-input multi-output linear time invariant controller has been designed that can ensure both altitude control and trajectory tracking in presence of wind gusts and measurement noise. The main contribution of this work is design of a single robust controller for flight control of the quadrotor, i.e. make it fly to achieve a certain altitude and then track the desired trajectory.

Following objectives are met to reach the stated aim of the research:

- a MIMO H_∞ controller design for the quadrotor model;
- application of designed controller in feedback with the quadrotor model for altitude control and trajectory tracking;
- introduction of wind gusts and measurement noise to verify the controller performance.

Rest of the paper is organized as follows: Section 2 describes the control oriented mathematical modeling of quadrotor. Section 3 briefly discusses the control design approach proposed in the paper. Discussion on the simulation results are presented in Section 4 and, finally, conclusions are drawn in Section 5.

2. Mathematical modeling of the quadrotor. Quadrotor consists of four arms bearing equal weights and length with a DC motor embedded in each of them to achieve the desired motion in a three-dimensional space. The inertial reference frame of a quadrotor system can be seen in Fig. 1.

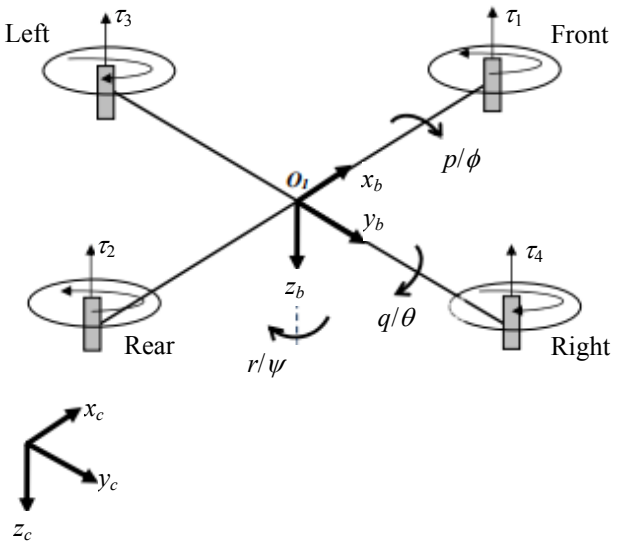

Fig. 1. Inertial reference frame of a quadrotor

Rotor angular positions of the motors can be denoted by Ω_i where i represents the motor on the i^{th} arm of the quadrotor and i = 1, 2, 3, 4. The angular velocities are denoted by ω_i. Rear and front rotors of the quadrotor revolve in counter-clock-wise-direction by angular speeds ω_1 and ω_2, thus generate the thruster torques τ_2 and τ_1 respectively. While motors 2 and 3 rotate in clock-wise-direction generating torques τ_3 and τ_4.

For hovering the quadrotor at a specific height, clock– and counter clock-wise-torques are desired to be the same and thus rotating the respective motors at a same speed, i.e. balancing the body weight of the quadrotor, is the main concern. Since the motor operate as to generate the thruster torques in opposite direction, there is no imbalance of the quadrotor reaction torque, i.e. there is zero imbalance in reaction torque. Roll, pitch and yaw angles, while considering the angular positions of the quadrotor body, are denoted by ϕ, θ and ψ respectively. Roll angle is created by increasing (decreasing) the speed of motor associated with right propeller and decreasing (increasing) that of the left one to make the body roll or turn along its own axis.

Throttle is achieved by rotating all the motors (propellers) in same direction at a same speed. Pitch angle is associated with the angular speed or front and rear motors and yaw movement can be generated by moving the front-rear and left-right propellers. If the speed of one pear, described earlier, is increasing that of the other should be reducing to generate the yaw movement. Three orthogonal movements in space and same number of orthogonal movements of the quadrotor offer six degree-of-freedom (DOF). The state-space of the quadrotor is given in (1). For the detailed study of the mathematical model, reader is referred to [14].

$$\begin{bmatrix}\ddot{\phi}\\ \ddot{\theta}\\ \ddot{\psi}\\ \ddot{x}\\ \ddot{y}\\ \ddot{z}\end{bmatrix}=\begin{bmatrix}1&0&0&0&0&0\\0&1&0&0&0&0\\0&0&1&0&0&0\\0&0&0&A_x&0&0\\0&0&0&0&A_y&0\\0&0&0&0&0&A_z\end{bmatrix}\cdot\begin{bmatrix}\dot{\phi}\\ \dot{\theta}\\ \dot{\psi}\\ \dot{x}\\ \dot{y}\\ \dot{z}\end{bmatrix}-\\ -\begin{bmatrix}0\\0\\0\\0\\0\\-g\end{bmatrix}+\begin{bmatrix}0\\0\\0\\0\\0\\1\end{bmatrix}\cdot\frac{F}{m}. \quad (1)$$

Equation (1) represents the state-space model of the 6-DOF quadrotor. However, the detailed state-space model can be represented by the state-space equations given in (2)-(13) [14]

$$\dot{x}_1 = x_2\,; \quad (2)$$

$$\dot{x}_2 = \frac{l\cdot k\left(\omega_4^2-\omega_2^2\right)}{I_{xx}}; \quad (3)$$

$$\dot{x}_3 = x_4\,; \quad (4)$$

$$\dot{x}_4 = \frac{l\cdot k\left(\omega_3^2-\omega_1^2\right)}{I_{yy}}; \quad (5)$$

$$\dot{x}_5 = x_6\,; \quad (6)$$

$$\dot{x}_6 = \frac{b\left(\omega_1^2-\omega_2^2+\omega_3^2-\omega_4^2\right)}{I_{zz}}; \quad (7)$$

$$\dot{x}_7 = x_8\,; \quad (8)$$

$$\dot{x}_8 = A_x x_1\,; \quad (9)$$

$$\dot{x}_9 = x_{10}\,; \quad (10)$$

$$\dot{x}_{10} = A_y x_3\,; \quad (11)$$

$$\dot{x}_{11} = x_{12}\,; \quad (12)$$

$$\dot{x}_{12} = A_z x_5 - g + \frac{1}{m}\left(\omega_1^2+\omega_2^2+\omega_3^2+\omega_4^2\right); \quad (13)$$

where ω_i represent the angular velocities of the motor on i^{th} arm of the quadrotor; g is the gravitational acceleration; l, b, k, m denote the arm length, coefficient of left and right drag, and mass of the quadrotor respectively; I_{xx}, I_{yy} and I_{zz} denote the moments of inertia in x, y and z axis respectively.

The set of state equations written in (2) – (13) are converted into state-space. The state-space matrices of the system are written as follows:

$$A=\begin{bmatrix}0&1&0&0&0&0&0&0&0&0&0&0\\0&0&0&0&0&0&0&0&0&0&0&0\\0&0&0&0&0&0&0&0&0&0&0&0\\0&0&0&1&0&0&0&0&0&0&0&0\\0&0&0&0&0&1&0&0&0&0&0&0\\0&0&0&0&0&0&0&0&0&0&0&0\\0&0&0&0&0&0&0&1&0&0&0&0\\A_x&0&0&0&0&0&0&0&0&0&0&0\\0&0&0&0&0&0&0&0&0&1&0&0\\0&0&A_y&0&0&0&0&0&0&0&0&0\\0&0&0&0&0&0&0&0&0&0&0&1\\0&0&0&0&A_z&0&0&0&0&0&0&0\end{bmatrix}; \quad (14)$$

$$B=\begin{bmatrix}0&0&0&0\\0&-l\cdot k/I_{xx}&0&l\cdot k/I_{xx}\\0&0&0&0\\-l\cdot k/I_{yy}&0&l\cdot k/I_{yy}&0\\0&0&0&0\\b/I_{zz}&-b/I_{zz}&b/I_{zz}&-b/I_{zz}\\0&0&0&0\\0&0&0&0\\0&0&0&0\\0&0&0&0\\0&0&0&0\\k&k&k&k\end{bmatrix}; \quad (15)$$

$$C=\begin{bmatrix}1&0&0&0&0&0&0&0&0&0&0&0\\0&0&1&0&0&0&0&0&0&0&0&0\\0&0&0&0&1&0&0&0&0&0&0&0\\0&0&0&0&0&0&1&0&0&0&0&0\\0&0&0&0&0&0&0&0&1&0&0&0\\0&0&0&0&0&0&0&0&0&0&1&0\end{bmatrix}. \quad (16)$$

The inputs, states, and outputs of the systems are given in (17)–(19), respectively

$$u=\begin{bmatrix}\omega_1^2 & \omega_2^2 & \omega_3^2 & \omega_4^2\end{bmatrix}^T; \quad (17)$$

$$x=\begin{bmatrix}\phi & \dot{\phi} & \theta & \dot{\theta} & \psi & \dot{\psi} & x & \dot{x} & y & \dot{y} & z & \dot{z}\end{bmatrix}^T; \quad (18)$$

$$y=\begin{bmatrix}\phi & \theta & \psi & x & y & z\end{bmatrix}^T. \quad (19)$$

The angular positions of the motors at quadrotor arms can be given as

$$\Omega_i=\frac{K_m\cdot r_a\cdot\eta\cdot N}{J}\cdot V_i, \quad (20)$$

where V_i is the input voltage for the i^{th} motor and $\omega_i = \dot{\Omega}_i$, rest of the parameters and their corresponding values are given in Table 1.

Table 1

Parameters of the quadrotor

Parameter	Value	Parameter	Value
A_x	0,45	I_{xx}, kg·m^2	$0{,}357\cdot10^{-5}$
A_y		I_{yy}, kg·m^2	
A_z		I_{zz}, kg·m^2	
k	$2{,}98\cdot10^{-6}$	m, kg	1,316
g, m/s^2	9,8	l, m	0,5

This model of the quadrotor is used to design the robust H_∞ controller for the flight control. A brief discussion about the controller design is given in the following section.

3. Robust control design. Controller is placed with the system for controlling the plant according to desired parameters and responses. Main objective general configuration of plant P (to be controlled) with the controller K is shown in Fig. 2.

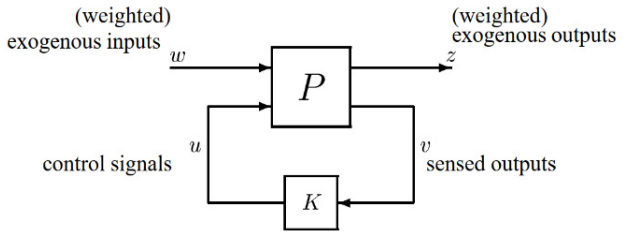

Fig. 2. General plant with controller configuration

Objective is to minimize the norm of transfer function from w to z and the design problem is to find controller gain K based on v which gives u as control signal to the plant which minimize the closed loop norm from w to z. The generalized configuration will then be represented as [15]:

$$\begin{bmatrix}z\\v\end{bmatrix}=P(s)\begin{bmatrix}w\\u\end{bmatrix}=\\=\begin{bmatrix}P_{11}(s) & P_{12}(s)\\P_{21}(s) & P_{22}(s)\end{bmatrix}\begin{bmatrix}w\\u\end{bmatrix}; \quad (21)$$

$$u=K(s)\cdot v. \quad (22)$$

The linear fractional transformation is

$$z=F_l(P,K)w, \quad (23)$$

where

$$F_l(P,K)=P_{11}+P_{12}K(1-P_{22}K)^{-1}P_{21}. \quad (24)$$

3.1. H_∞ controller.

The H_∞ optimal control problem is to find all stabilizing controllers K that minimize [15]

$$\left\|F_l(P,K)\right\|_\infty=\max_w\bar{\sigma}\left(F_l(P,K)\cdot(j\omega)\right). \quad (25)$$

The H_∞ norm has several interpretations in terms of performance. One is that it minimizes the peak of the maximum singular value of $F_l(P(j\omega), K(j\omega))$. In practice, it is usually not necessary to obtain an optimal controller for the H_∞ problem, and it is often computationally (and theoretically) simpler to design a suboptimal one (i.e. one close to the optimal ones in the sense of the H_∞ norm). Let $\gamma_{\min}$ be the minimum value of overall stabilizing controllers K. Then the H_∞ sub-optimal control problem is: given a $\gamma > \gamma_{\min}$, find all stabilizing controllers K such that

$$\left\|F_l(P,K)\right\|_\infty =< \gamma. \quad (26)$$

If we desire a controller that achieves $\gamma_{\min}$, to within a specified tolerance, then we can perform a bisection on γ until its value is sufficiently accurate. The above result provides a test for each value of γ to determine whether it is less than $\gamma_{\min}$ or greater than $\gamma_{\min}$.

Two methods are there for H_∞ controller design: the transfer function shaping approach and the signal-based approach. In the former, H_∞ optimization is used to shape the singular values of specified transfer functions over frequency. The maximum singular values are relatively easy to shape by forcing them to lie below user defined bounds, thereby ensuring desirable and widths and roll-off rates. In the signal-based approach, we seek to minimize the energy in certain error signals given a set of exogenous input signals [16]. The latter might include the outputs of perturbations representing uncertainty, as well as the usual disturbances, noise, and command signals. Both two approaches will be considered again in the remainder of this section. In each case we will examine a problem and formulate it in the general control configuration.

A difficulty that sometimes arises with H_∞ control is the selection of weights such that the H_∞ optimal controller provides a good trade-off between conflicting objectives in various frequency ranges. Thus, for practical designs it is sometimes recommended to perform only a few iterations of the H_∞ algorithm. The justification for this is that the initial design, after one iteration, is like a H_2 design which does trade-off over various frequency ranges. Therefore, stopping the iterations before the optimal value is achieved gives the design H_2 flavor which may be desirable.

4. Results and discussions. For the controller validation, a simulation environment is developed in which a 3D trajectory is tracked by the proposed control methodology.

Figures 3, 4 show the tracking of x and y coordinates. It can be observed from plots that controller reaches and stay on desired x and y coordinates with minimum estimation error.

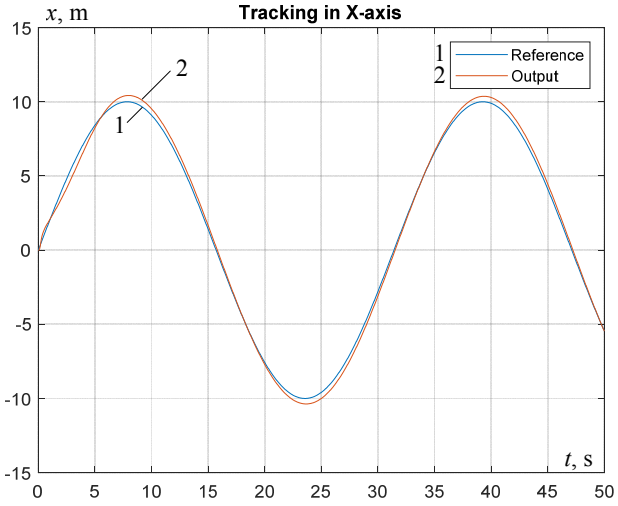

Fig. 3. Tracking of x coordinates

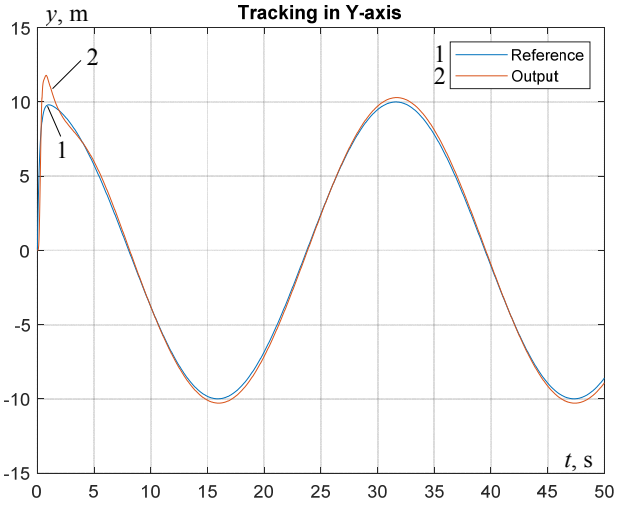

Fig. 4. Tracking of y coordinates

Initially it is assumed that, quadrotor is hovering at zero altitude. Then it is desired that it gains 10 m of height with slowly increasing altitude value as shown in Fig. 5.

After gaining the desired height it is aimed that quadrotor moves in a circular trajectory having radius of 10 m as shown in the Fig. 5. From Fig. 5, 6, it can be observed that initially tracking error is high but few seconds later controller achieves the desired height. Quadrotor reaches desired altitude within 5 s, which is reasonable performance. After gaining desired altitude quadrotor tracks the specified trajectory with minimum estimation error. From Fig. 5, the tracking of circular trajectory can be seen. Despite the tracking of desired trajectory, the most important is that quadrotor maintains its stable attitudes. Stability of attitudes mean that quadrotor do not observe the excessive roll and pitch

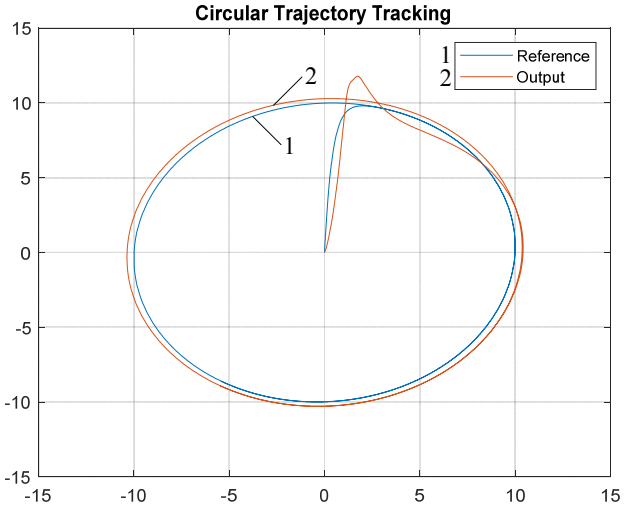

Fig. 5. Tracking of planar trajectory

motion. If quadrotor tracks the desired trajectory under excessive roll and pitch motion, then stability of motion cannot be guaranteed. Actually, it is the best possible case that quadrotor tracks the desired trajectory with minimum roll and pitch angle.

The tracking of desired attitude is displayed in Fig. 6, the plot shows that initially at starting point quadrotor start motion with greater pitch and roll angle but after 1 s of flight it achieves attitudes close to zero. These observation increases the confidence on controller performance and real time implication of designed control scheme. At last the most important observation is the control efforts calculated by controller. In existing case the control efforts are the angular velocities of four motors.

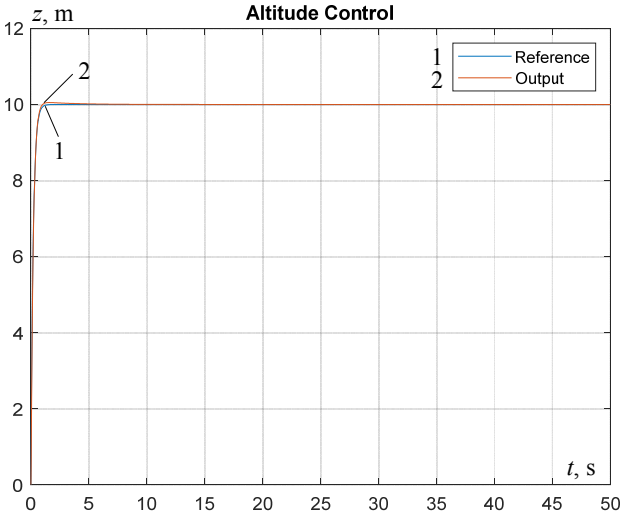

Fig. 6. Tracking of desired altitude

Figures 7–9 show the control effort plots. From the plots it can be seen that controller calculates smooth control inputs for motors with no chattering. Initially large fluctuations in motor speed can be seen but after 2 s they gains the steady value that are consistent with the trajectory tracking and attitude tracking of the quadrotor.

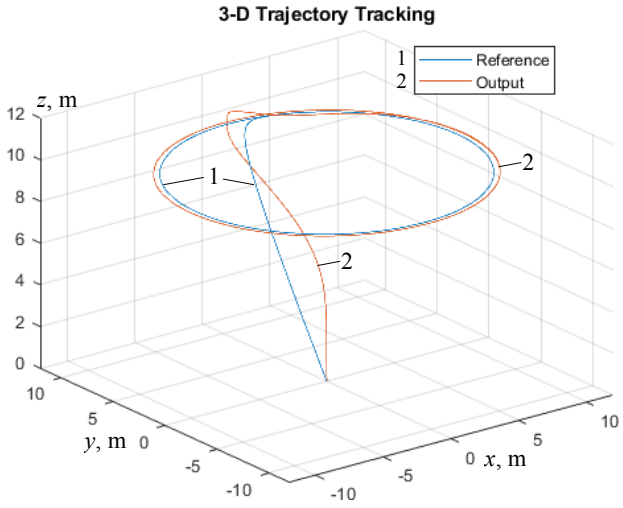

Fig. 7. Tracking of 3D trajectory

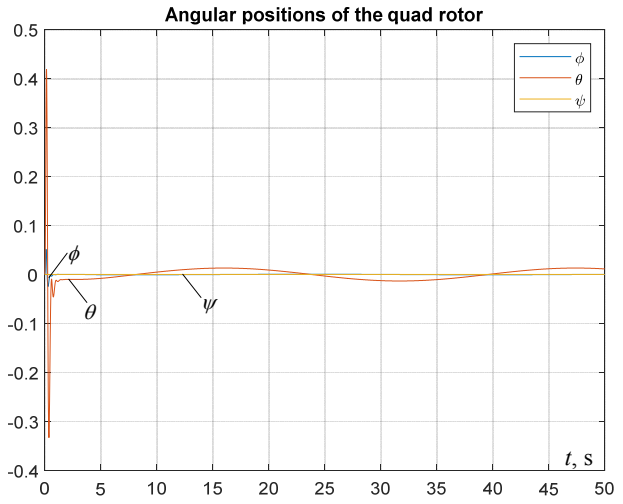

Fig. 8. Attitudes of quadrotor

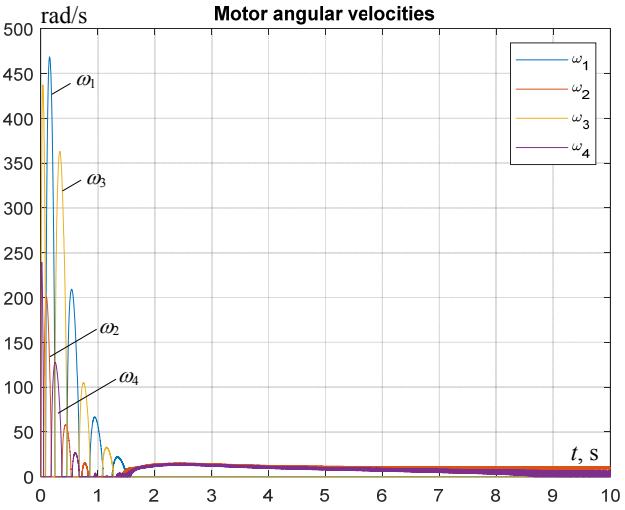

Fig. 9. Quadrotor motor speeds

5. Conclusions.

A robust H_∞ single Multi input multi output linear time invariant controller for six degree of freedom quadrotor has been designed that can ensure both altitude control and trajectory tracking in presence of wind gusts and measurement noise. Quadrotor is first lifted to the height of 10 m and after achieving the desired altitude, it starts moving in circular path which keeping roll and pitch angles at 0°. Roll, pitch and angles are shown in results and discussion section. From the plots it can be seen that controller calculates smooth control inputs for motors with no chattering. Initially large fluctuations in motor speed can be seen but after 2 s they gains the steady value that are consistent with the trajectory tracking and attitude tracking of the quadrotor. In future, same work can be applied to the quadrotor by considering the wind gusts.

Conflict of interest. The authors declare that they have no conflicts of interest.

REFERENCES

1. Valavanis K.P., Vachtsevanos G.J. *Handbook of unmanned aerial vehicles*. Springer Science + Business Media Dordrecht, 2015. doi: https://doi.org/10.1007/978-90-481-9707-1.

2. Luzar M., Korbicz J. Linear parameter-varying two rotor aero-dynamical system modelling with state-space neural network. In: Rutkowski L., Scherer R., Korytkowski M., Pedrycz W., Tadeusiewicz R., Zurada J. (eds) *Artificial Intelligence and Soft Computing. ICAISC 2018. Lecture Notes in Computer Science*, 2018, vol. 10842. Springer, Cham. doi: https://doi.org/10.1007/978-3-319-91262-2_52.

3. Venkatesan C. *Fundamentals of helicopter dynamics*. CRC Press, 2014. 338 p. doi: https://doi.org/10.1201/b17314.

4. Juang J., Huang M., Liu W. PID control using presearched genetic algorithms for a MIMO system. *IEEE Transactions on Systems, Man, and Cybernetics, Part C (Applications and Reviews)*, 2008, vol. 38, no. 5, pp. 716-727. doi: https://doi.org/10.1109/tsmcc.2008.923890.

5. Aldebrez F.M., Alam M.S., Tokhi M.O. Input-shaping with GA-tuned PID for target tracking and vibration reduction. *Proceedings of the 2005 IEEE International Symposium on, Mediterrean Conference on Control and Automation Intelligent Control*, 2005, pp. 485-490, doi: https://doi.org/10.1109/.2005.1467063.

6. Wen P., Lu T.W. 2008. Decoupling control of a twin rotor MIMO system using robust deadbeat control technique. *IET Control Theory & Applications*, 2008, vol. 2, no. 11, pp. 999-1007. doi: http://dx.doi.org/10.1049/iet-cta:20070335.

7. Pratap B., Agrawal A., Purwar S. Optimal control of twin rotor MIMO system using output feedback. *2012 2nd International Conference on Power, Control and Embedded Systems*, 2012, pp. 1-6. doi: https://doi.org/10.1109/icpces.2012.6508113.

8. Thien R.T.Y., Kim Y. Decentralized formation flight via PID and integral sliding mode control. *Aerospace Science and Technology*, 2018, vol. 81, pp. 322-332. doi: https://doi.org/10.1016/j.ast.2018.08.011.

9. Moreno-Valenzuela J., Pérez-Alcocer R., Guerrero-Medina M., Dzul A. Nonlinear PID-type controller for quadrotor trajectory tracking. *IEEE/ASME Transactions on Mechatronics*, 2018, vol. 23, no. 5, pp. 2436-2447. doi: https://doi.org/10.1109/TMECH.2018.2855161.

10. Li Z., Ma X., Li Y. Model-free control of a quadrotor using adaptive proportional derivative-sliding mode control and robust integral of the signum of the error. *International Journal of Advanced Robotic Systems*, 2018, vol. 15, no. 5, p. 172988141880088. doi: https://doi.org/10.1177/1729881418800885.

11. Akbar R., Uchiyama N. Design and experiment of adaptive modified super-twisting control with a nonlinear sliding surface for a quadrotor helicopter. *Advances in Mechanical Engineering*, 2018, vol. 10, no. 10, p. 168781401880493. doi: https://doi.org/10.1177/1687814018804934.

12. Tran T.-T., Ha C. Self-tuning proportional double derivative-like neural network controller for a quadrotor. *International Journal of Aeronautical and Space Sciences*, 2018,

vol. 19, no. 4, pp. 976-985. doi: https://doi.org/10.1007/s42405-018-0091-6.
13. Govea-Vargas A., Castro-Linares R., Duarte-Mermoud M., Aguila-Camacho N., Ceballos-Benavides G. Fractional order sliding mode control of a class of second order perturbed nonlinear systems: application to the trajectory tracking of a quadrotor. *Algorithms*, 2018, vol. 11, no. 11, p. 168. doi: https://doi.org/10.3390/a11110168.
14. Tengis T., Batmunkh A. State feedback control simulation of quadcopter model. *2016 11th International Forum on Strategic Technology (IFOST)*, 2016, pp. 553-557. doi: https://doi.org/10.1109/ifost.2016.7884178.
15. Skogestad S., Postlethwaite I. Multivariable feedback control: analysis and design. New York, Wiley, 2005.
16. John L., Mija S.J. Robust H∞ control algorithm for Twin Rotor MIMO System. *2014 IEEE International Conference on Advanced Communications, Control and Computing Technologies*, 2014, pp. 168-173. doi: https://doi.org/10.1109/ICACCCT.2014.7019402.

Received 13.06.2021
Accepted 28.08.2021
Published 26.10.2021

Zulfiqar Ali Gulshan[1], *Engineer, MS,*
Muhammad Zulqarnain Haider Ali[2], *Engineer, MS,*
Muhammad Shahzaib Shah[2], *Engineer, MS,*
Danish Nouman[2], *Engineer, MS,*
Mehwish Anwar[2], *Engineer, MS,*
Mian Farhan Ullah[3], *PhD Scholar, Lecturer*,
[1] Department of Electrical Engineering,
Fast University CHT-FSD campus,
CHT-FSD, Islamabad, Pakistan,
e-mail: gulshan037@gmail.com
[2] Department of Electrical Engineering,
University of Engineering and Technology, Taxila, Pakistan,
e-mail: mzulqarnain.haider@students.uettaxila.edu.pk;
m.shahzaibshah@students.uettaxila.edu.pk;
danishnouman1@gmail.com;
mehwishanwar4455@gmail.com;
[3] Department of Mechatronics Engineering,
Wah Engineering College, University of Wah,
Quaid Avenue, Wah Cantt, Rawalpindi District,
Punjab 47040, Pakistan.
e-mail: farhan.ullah@wecuw.edu.pk (Corresponding author)

How to cite this article:
Gulshan Z.A., Ali M.Z.H., Shah M.S., Nouman D., Anwar M., Ullah M.F. A robust control design approach for altitude control and trajectory tracking of a quadrotor. *Electrical Engineering & Electromechanics*, 2021, no. 5, pp. 17-23. doi: https://doi.org/10.20998/2074-272X.2021.5.03.

UDC 621.3.013 https://doi.org/10.20998/2074-272X.2021.5.04

B.I. Kuznetsov, T.B. Nikitina, I.V. Bovdui, V.V. Kolomiets, B.B. Kobylianskiy

REDUCTION OF MAGNETIC FIELD LEVEL IN RESIDENTIAL OLD BUILDINGS FROM OVERHEAD POWER LINES BY MEANS OF ACTIVE SCREENING

Aim. *Reduction of the magnetic field induction to the level of modern sanitary standards by means of active screening in residential old buildings which are located near existing typical overhead power lines are considered. Active shielding of the magnetic field inside a single-storey and multi-storey building is considered. During the design the number, configurations, spatial arrangement of the shielding windings, as well as the currents in the shielding windings were determined.* ***Methodology***. *The design problem for the system of active shielding reduced to solving the minimax vector optimization problem. The vector of objective function in this minimax problem is calculated based on Biot-Savart's law. The solution of this problem is based on multi-agent optimization algorithms.* ***Results***. *The results of theoretical and experimental studies of the systems of active shielding of the magnetic field generated by various overhead power lines inside a single and multi-storey building are presented.* ***Originality.*** *The possibility of reducing the induction of the initial magnetic field inside the shielded space to the level of sanitary standards is shown.* ***Practical value***. *From the point of view of the practical implementation for a reasonable choice of the number and spatial arrangement of shielding windings of systems for active shielding of the magnetic field generated by various overhead power lines inside residential buildings of different storey's are given.* References 47, figures 7.
Key words: **overhead power line, magnetic field, system of active screening, computer simulation, experimental research**.

Мета. *Розглянуто зниження індукції магнітного поля до рівня сучасних санітарних норм за рахунок активного екранування в житлових будинках старої забудови, розташованих поблизу існуючих типових повітряних ліній електропередачі. Розглянуто активне екранування магнітного поля всередині одноповерхового і багатоповерхового будинку. При проектуванні визначалися кількість, конфігурація, просторове розташування екрануючих обмоток, а також струми в екрануючих обмотках.* ***Методологія.*** *Завдання проектування системи активного екранування зводиться до вирішення задачі мінімаксної векторної оптимізації. Вектор цільової функції в цій мінімаксній задачі обчислюється на основі закону Біо-Савара. Вирішення цієї проблеми грунтується на алгоритмах багатоагентної оптимізації.* ***Результати.*** *Представлені результати теоретичних і експериментальних досліджень систем активного екранування магнітного поля, що створюється різними повітряними лініями електропередачі всередині одно- і багатоповерхового будинку.* ***Оригінальність.*** *Показана можливість зниження індукції початкового магнітного поля всередині простору, що екранується, до рівня санітарних норм.* ***Практична цінність.*** *З точки зору практичної реалізації представлені рекомендаці для обгрунтованого вибору кількості і просторового розташування екрануючих обмоток систем активного екранування магнітного поля, що створюється різними повітряними лініями електропередач всередині житлових будинків різної поверховості.* Бібл. 47, рис. 7.
Ключові слова: **повітряна лінія електропередачі, магнітне поле, система активного екранування, комп'ютерне моделювання, експериментальні дослідження.**

Introduction. Existing high-voltage overhead power lines, located in residential areas of most developed countries, are the main sources of magnetic field of industrial frequency, which has a massive effect on the population and is more dangerous to health than the electric field [1-4]. Experts of the World Health Organization in the late 20th century discovered the carcinogenic properties of the magnetic field of overhead power lines with its weak but long-lasting effects on humans. Therefore, in the last 20 years the world has been actively implementing and constantly strengthening sanitary norms from the maximum allowable level of induction of magnetic field 50-60 Hz for the population, intensive development of methods for normalization of magnetic field [5-11].

Recently, strict sanitary standards for the induction of a magnetic field of 50 Hz (0,5 μT for the population) were introduced for the first time in the regulations of Ukraine. However, in Ukraine these norms are for most of the existing 10-330 kV overhead power lines, which were built during the last 50 years without taking into account the current requirements for magnetic field, are not fulfilled.

Thus, as shown by the calculations and results of numerous experiments [1, 2], the maximum allowable level of induction of magnetic field at the boundary of the sanitary protection zones of existing substations, previously determined only by electric field, may be exceeded by more than an order of magnitude. This poses a threat to the health of hundreds of thousands of people living closer than 100 m from overhead power lines.

Moreover, often residential old buildings are generally located near power lines, as it is shown in Fig. 1.

Fig. 1. Location of residential old buildings near power lines

This situation requires urgent measures to reduce to a safe level induction of high-voltage overhead power lines in nearby residential houses. Such normalization of

magnetic field can be carried out either by reconstruction of the overhead power lines, or by shielding residential buildings from the magnetic field of overhead power lines.

Reconstruction is the most effective method to reduce to a safe level induction of magnetic field.

Higher shielding efficiency of magnetic field submarines (up to 10) with less metal capacity is possible to provide methods of active shielding of magnetic field [12-18]. Their essence is automatic formation in a closed structure by means of special windings of the compensating magnetic field with such spatial time structure, the superposition of which with magnetic field submarine in the protection zone is minimized to a safe level. Active shielding technology does not allow relatively inexpensive means to solve socially important problems.

The technology of active shielding of magnetic field of operating substations has been used by the majority for more than 10 years developed countries, such as the United States, Italy, Spain and Israel [5-11]. In works [12-18], methods for designing of such systems of active screening based on genetic optimization algorithms were developed. However, these works do not consider the issues of the synthesis of robust systems of active screening, the characteristics of which are not sensitive to changes in the parameters and, possibly, the structure of the control object and the parameters of the original magnetic field [19-22].

In Ukraine in residential buildings of core city buildings single-storey and multi-storey buildings most often are located near existing 10-330 kV overhead power lines including single-circuit overhead power lines with a triangular suspension of wires, double-circuit overhead power lines with a suspension of «barrel»-type wires.

The **purpose of the work** is to reduce the magnetic field induction in residential buildings of old buildings which are located near existing various types overhead power lines to the level of modern sanitary standards by means of active screening.

Statement of the research problem. The mathematical model of the vector induction $\boldsymbol{B}_o(P_i, \boldsymbol{I}_0(t), t)$ of the initial magnetic field [22-28] in the form of the sum of the vector inductions $\boldsymbol{B}_{ol}(P_i, \boldsymbol{I}_l(t))$ generated by all L currents $I_l(t)$ in the conductors l of the power transmission line at a point P_i at a time t is based on the Biot-Savart law in the following form

$$\boldsymbol{B}_o\left(P_i, \boldsymbol{I}_0(t), t\right) = \sum_{l=1}^{L} \boldsymbol{B}_{ol}\left(P_i, I_l(t)\right), \qquad (1)$$

here a vector of power transmission line currents $\boldsymbol{I}_0(t)$ is introduced, the components of which are the currents $I_l(t)$ in l current conductors of the power transmission line $\boldsymbol{I}_0(t) = \{I_l(t)\}$.

The shielding magnetic field induction $\boldsymbol{B}_y(P_i, \boldsymbol{I}_y(t), t)$ generated by M control windings can be calculated similarly as the sum of the inductions $\boldsymbol{B}_{ym}(P_i, I_{ym}(t), t)$ generated by the m currents $I_l(t)$ of the shielding windings at a point P_i at a time t in the following form

$$\boldsymbol{B}_y\left(P_i, \boldsymbol{I}_y(t), t\right) = \sum_{m=1}^{M} \boldsymbol{B}_{ym}\left(P_i, I_{ym}(t), t\right), \qquad (2)$$

here the vector $\boldsymbol{I}_y(t)$ of currents of the shielding windings is introduced, the components of which are $I_l(t)$ the currents in m shielding windings $\boldsymbol{I}_y(t) = \{I_{ym}(t)\}$.

With the help of the M windings of the system of active screening, it is necessary to generate a magnetic field with the induction $\boldsymbol{B}_y(P_i, \boldsymbol{I}_y(t), t)$ at the point P_i of the considered space, with the help of which the induction $\boldsymbol{B}_o(P_i, \boldsymbol{I}_0(t), t)$ of initial magnetic field in the point P_i of considered space is compensated, so that the induction $\boldsymbol{B}(P_i, \boldsymbol{I}_0(t), \boldsymbol{I}_y(t), t)$ of the total magnetic field generated by currents $\boldsymbol{I}_0(t)$ of wires of power lines and currents $\boldsymbol{I}_y(t)$ of control windings at all points P_i, of the considered space

$$\begin{aligned} &\boldsymbol{B}\left(P_i, \boldsymbol{I}_o(t), \boldsymbol{I}_y(t), t\right) = \\ &= \boldsymbol{B}_o\left(P_i, \boldsymbol{I}_0(t), t\right) + \ldots + \boldsymbol{B}_y\left(P_i, \boldsymbol{I}_y(t), t\right), \end{aligned} \qquad (3)$$

does not exceed the level of sanitary standards for all points P_i of the considered screening space.

The task of designing of the system of active shielding is to determine the number and spatial location of the compensating windings, as well as the currents in these windings.

Solution method. In the process of designing of the system of active shielding, it is necessary to determine the amount M of compensating windings and the coordinates $\boldsymbol{X}$ and $\boldsymbol{Y}$ of the spatial arrangement of the compensating windings, as well as the currents $\boldsymbol{I}_y(t)$ in these windings [20]–[23]. Let us introduce a vector of the sought-for design parameters of the system of active shielding, the components of which are the amount M of compensating windings and the coordinates of the $\boldsymbol{X}$ and $\boldsymbol{Y}$ of the spatial arrangement of the compensating windings, as well as the currents of the $\boldsymbol{I}_y(t)$ in these windings. Then, for a given value of the M quantity and the coordinates of the $\boldsymbol{X}$ and $\boldsymbol{Y}$ of the spatial arrangement of the compensating windings, as well as the $\boldsymbol{I}_y(t)$ currents in these windings, the mathematical model of the induction $\boldsymbol{B}_y(P_i, \boldsymbol{I}_y(t), t)$ of the magnetic field generated at the point P_i of the space under consideration by all compensating windings is also based on the Biot-Savart law.

When the system of active shielding operates at the points of the shielding space located closer to the power transmission line, undercompensation of the initial magnetic field is possible, since the induction of the magnetic field generated by the compensation windings decreases faster than the induction of the initial magnetic field generated by the power transmission line. On the other hand, at the points of the shielding space located further from the power transmission line, overcompensation of the initial magnetic field is possible, since the induction of the magnetic field generated by the compensation windings near these windings has a significantly greater value of the induction of the initial magnetic field generated by the power transmission line in these same points [24-28]. Therefore, to reduce the number of points taken into account, you can take a limited number of points in the shielding space near the transmission line and the most distant from the transmission line.

A feature of the design problem is that the parameters of the initial magnetic field, its induction and the spatio-temporal characteristic, due, in particular, to the

currents in the wires of the power transmission line, are not known exactly in advance and changes in time-during the day, the time of the year and others. In addition, the parameters of the active screening system, in particular, the geometric dimensions of the compensating windings and regulators, firstly, are implemented with some error and, secondly, change during the operation of the system of active shielding.

Therefore, the design of system of active shielding must be carried out taking into account the uncertainty of both the parameters of the initial magnetic field and the system of active shielding parameters [29-35]. Let us introduce a vector of uncertainties, the components of which are the deviations of the parameters of the initial magnetic field and the parameters of the system of active shielding from their nominal values adopted in the design of the system of active shielding.

Let's reduce the design of the system of active shielding to solving the optimization problem. In the presence of uncertainties in the system, the design of a robust system is usually reduced to the «worst» case, when the uncertainty vector behaves the most maliciously and maximally degrades the compensation of the initial magnetic field with the help of compensating windings [36-38]. Then the design problem for the system of active shielding can be reduced to solving the following maximin vector optimization problem [39-41]. The vector objective function in this minimax problem is calculated based on Biot-Savart's law.

The solution to this problem is based on multi-agent optimization algorithms [42-47].

Results of modeling and experimental research. In residential buildings of core city buildings which are located near existing typical power lines the most widespread are single-circuit 110 kV transmission lines with a triangular suspension of wires. Moreover, in the area of laying these power lines, single-story residential buildings are most often in the immediate vicinity. The layout of power transmission line, single-story residential building, in which it is necessary to reduce the induction of the initial magnetic field to the level of modern sanitary standards, and compensating windings are shown in Fig. 2. As a result of the design of the system of active shielding two compensating windings was calculated.

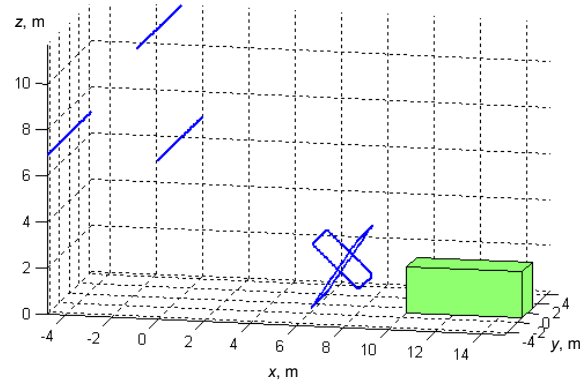

Fig. 2. The layout of single-circuit 110 kV transmission lines, compensating windings and one-story residential building

In Fig. 3 is shown two compensating windings of experimental plant of system of active shielding.

Fig. 3. Location of three compensating windings of experimental plant of system of active shielding

In Fig. 4 are shown modeling and experimental dependences of the induction of the initial and resulting magnetic field as a function of the distance from the power transmission line in the house, where it is necessary to reduce the level of induction of the initial magnetic field generated by the power transmission line. As can be seen from this figure, the level of induction of the initial magnetic field varies from 0,65 μT to 1,5 μT. The induction of the total magnetic field in the shielding zone practically does not exceed the level of sanitary standards.

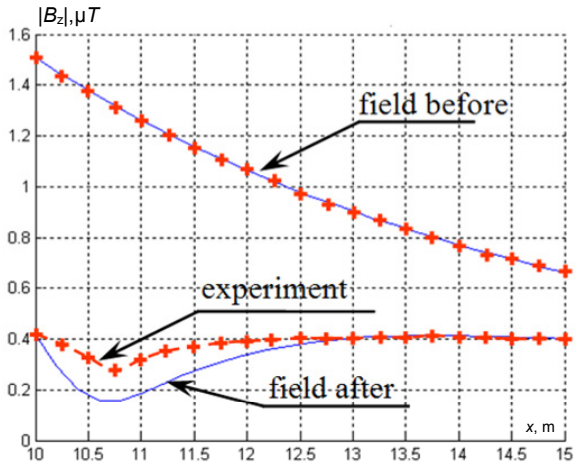

Fig. 4. Comparison of magnetic flux density between measurements and simulations with and without system of active shielding

Single-circuit 110 kV power transmission lines with a triangular suspension of wires often run near multi-storey buildings of core city buildings. The layout of such a power transmission line, compensating windings and a multi-storey residential building, in which it is necessary to reduce the induction of the initial magnetic field to the level of modern sanitary standards, are shown in Fig. 5. As a result of design of the system of active shielding, the coordinates of three compensating windings were calculated.

In Fig. 6 are shown three compensating windings of experimental plant of system of active shielding.

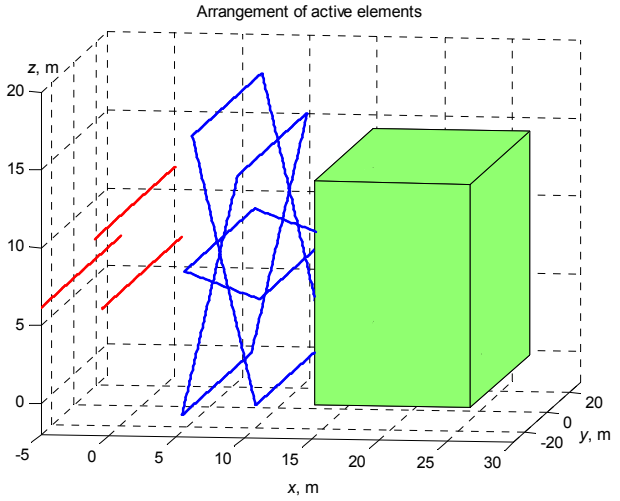

Fig. 5. The layout of single-circuit 110 kV transmission lines with a triangular suspension of wires and multi-storey residential building

Fig. 6. Location of three compensating windings of experimental plant of system of active shielding

Results of modeling and experimental dependences of the initial and resulting magnetic field induction as a function of the distance from the power transmission line are shown in Fig. 7 The level of the initial magnetic field induction varies from 2,25 μT to 0,8 μT.

The level of the total magnetic field induction in the house, where it is necessary to reduce the level of the initial magnetic field induction does not exceed the sanitary standards level.

Double-circuit overhead power lines with a suspension of «barrel»-type wires also often run near single-storey and multi-storey buildings of city core buildings.

Such overhead power lines generate a weakly polarized magnetic field, the space-time characteristic of which is a highly elongated ellipse. To effectively compensate for such a magnetic field, one screening winding is sufficient. Such a winding generates magnetic field, the space-time characteristic of which is a straight line. Therefore, with the help of such a shielding winding, it is possible to compensate for the major axis of the space-time characteristic ellipse of the initial magnetic field and to realize a sufficiently high shielding efficiency.

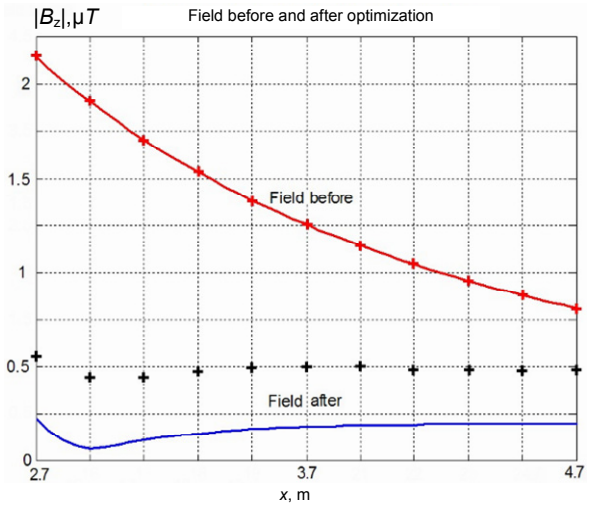

Fig. 7. Comparison of magnetic flux density between measurements (solid lines) and simulations (+) with and without system of active shielding

As a result of design of the system of active shielding for such overhead power lines the coordinate's only single compensating winding were calculated. During modeling and experimental research of such system of active shielding with only single compensating winding was shown the possibility to reduce the induction of the initial magnetic field to the level of modern sanitary standards in residential buildings of city core buildings including single-storey and multi-storey buildings which are located near existing double-circuit overhead power lines with a suspension of «barrel»-type wires.

Conclusions.

1. The method for the design problem for the system of active screening has been developed. During the design the number, configuration, spatial arrangement of the shielding windings and the currents in the shielding windings were determined. The design problem is reduced to solving the maximin vector optimization problem. The vector objective function in this minimax problem is calculated based on Biot-Savart's law. The solution of this problem is based on multi-agent optimization algorithms.

2. On the basis of the developed method the design of the different type of systems of active screening to reduce the magnetic field induction to the level of modern sanitary standards for residential buildings of core city buildings have been carried out. These systems contain different number screening coils and include single-storey and multi-storey buildings which are located near existing typical power lines including single-circuit overhead power lines with a triangular suspension of wires, double-circuit overhead power lines with a suspension of «barrel»-type wires.

3. As a result of computer simulation and experimental studies of the synthesized systems of active screening, it is shown that with the help of the synthesized systems, the level of induction of the magnetic field in single-storey and multi-storey buildings generated by different types of high-voltage power lines are reduced to the sanitary standards of Ukraine.

Conflict of interest. The authors declare that they have no conflicts of interest.

REFERENCES

1. Rozov V.Yu., Grinchenko V.S., Yerisov A.V., Dobrodeyev P.N. Efficient shielding of three-phase cable line magnetic field by passive loop under limited thermal effect on power cables. *Electrical Engineering & Electromechanics*, 2019, no. 6, pp. 50-54. doi: https://doi.org/10.20998/2074-272x.2019.6.07.

2. Rozov V., Grinchenko V. Simulation and analysis of power frequency electromagnetic field in buildings closed to overhead lines. *2017 IEEE First Ukraine Conference on Electrical and Computer Engineering (UKRCON)*, Kyiv, UKraine, 2017, pp. 500-503. doi: https://doi.org/10.1109/ukrcon.2017.8100538.

3. Rozov V.Yu., Kundius K.D., Pelevin D.Ye. Active shielding of external magnetic field of built-in transformer substations. *Electrical Engineering & Electromechanics*, 2020, no. 3, pp. 24-30. doi: https://doi.org/10.20998/2074-272x.2020.3.04.

4. Rozov V.Y., Zavalnyi A.V., Zolotov S.M., Gretskikh S.V. The normalization methods of the static geomagnetic field inside houses. *Electrical Engineering & Electromechanics*, 2015, no. 2, pp. 35-40. doi: https://doi.org/10.20998/2074-272x.2015.2.07.

5. Salceanu A., Paulet M., Alistar B.D., Asiminicesei O. Upon the contribution of image currents on the magnetic fields generated by overhead power lines. *2019 International Conference on Electromechanical and Energy Systems (SIELMEN).* 2019. doi: https://doi.org/10.1109/sielmen.2019.8905880.

6. Del Pino Lopez J.C., Romero P.C. Influence of different types of magnetic shields on the thermal behavior and ampacity of underground power cables. *IEEE Transactions on Power Delivery*, Oct. 2011, vol. 26, no. 4, pp. 2659-2667. doi: https://doi.org/10.1109/tpwrd.2011.2158593.

7. Ippolito L., Siano P. Using multi-objective optimal power flow for reducing magnetic fields from power lines. *Electric Power Systems Research*, Feb. 2004, vol. 68, no. 2, pp. 93-101. doi: https://doi.org/10.1016/s0378-7796(03)00151-2.

8. Barsali S., Giglioli R., Poli D. Active shielding of overhead line magnetic field: Design and applications. *Electric Power Systems Research*, May 2014, vol. 110, pp. 55-63. doi: https://doi.org/10.1016/j.epsr.2014.01.005.

9. Bavastro D., Canova A., Freschi F., Giaccone L., Manca M. Magnetic field mitigation at power frequency: design principles and case studies. *IEEE Transactions on Industry Applications*, May 2015, vol. 51, no. 3, pp. 2009-2016. doi: https://doi.org/10.1109/tia.2014.2369813.

10. Beltran H., Fuster V., García M. Magnetic field reduction screening system for a magnetic field source used in industrial applications. *9 Congreso Hispano Luso de Ingeniería Eléctrica (9 CHLIE)*, Marbella (Málaga, Spain), 2005, pp. 84-99. Available at: https://www.researchgate.net/publication/229020921_Magnetic_field_reduction_screening_system_for_a_magnetic_field_source_used_in_industrial_applications (Accessed 22.06.2021).

11. Bravo-Rodríguez J., Del-Pino-López J., Cruz-Romero P. A Survey on Optimization Techniques Applied to Magnetic Field Mitigation in Power Systems. *Energies*, 2019, vol. 12, no. 7, p. 1332. doi: https://doi.org/10.3390/en12071332.

12. Canova A., del-Pino-López J.C., Giaccone L., Manca M. Active Shielding System for ELF Magnetic Fields. *IEEE Transactions on Magnetics*, March 2015, vol. 51, no. 3, pp. 1-4. doi: https://doi.org/10.1109/tmag.2014.2354515.

13. Canova A., Giaccone L. Real-time optimization of active loops for the magnetic field minimization. *International Journal of Applied Electromagnetics and Mechanics*, Feb. 2018, vol. 56, pp. 97-106. doi: https://doi.org/10.3233/jae-172286.

14. Canova A., Giaccone L., Cirimele V. Active and passive shield for aerial power lines. *Proc. of the 25th International Conference on Electricity Distribution (CIRED 2019)*, 3-6 June 2019, Madrid, Spain. Paper no. 1096. Available at: https://www.cired-repository.org/handle/20.500.12455/290 (Accessed 28.10.2020).

15. Canova A., Giaccone L. High-performance magnetic shielding solution for extremely low frequency (ELF) sources. *CIRED - Open Access Proceedings Journal*, Oct. 2017, vol. 2017, no. 1, pp. 686-690. doi: https://doi.org/10.1049/oap-cired.2017.1029.

16. Celozzi S. Active compensation and partial shields for the power-frequency magnetic field reduction. *2002 IEEE International Symposium on Electromagnetic Compatibility*, Minneapolis, MN, USA, 2002, vol. 1, pp. 222-226. doi: https://doi.org/10.1109/isemc.2002.1032478.

17. Celozzi S., Garzia F. Active shielding for power-frequency magnetic field reduction using genetic algorithms optimization. *IEE Proceedings - Science, Measurement and Technology*, 2004, vol. 151, no. 1, pp. 2-7. doi: https://doi.org/10.1049/ip-smt:20040002.

18. Celozzi S., Garzia F. Magnetic field reduction by means of active shielding techniques. *WIT Transactions on Biomedicine and Health*, 2003, vol. 7, pp. 79-89. doi: https://doi.org/10.2495/ehr030091.

19. Martynenko G. Practical application of the analytical method of electromagnetic circuit analysis for determining magnetic forces in active magnetic bearings. *2020 IEEE Problems of Automated Electrodrive. Theory and Practice (PAEP)*, 2020, pp. 1-4, doi: https://doi.org/10.1109/paep49887.2020.9240774.

20. Martynenko G., Martynenko V. Modeling of the dynamics of rotors of an energy gas turbine installation using an analytical method for analyzing active magnetic bearing circuits. *2020 IEEE KhPI Week on Advanced Technology (KhPIWeek)*, 2020, pp. 92-97 .doi: https://doi.org/10.1109/KhPIWeek51551.2020.9250156.

21. Buriakovskyi S.G., Maslii A.S., Pasko O.V., Smirnov V.V. Mathematical modelling of transients in the electric drive of the switch – the main executive element of railway automation. *Electrical Engineering & Electromechanics*, 2020, no. 4, pp. 17-23. doi: https://doi.org/10.20998/2074-272X.2020.4.03.

22. Ostroverkhov M., Chumack V., Monakhov E., Ponomarev A. Hybrid Excited Synchronous Generator for Microhydropower Unit. *2019 IEEE 6th International Conference on Energy Smart Systems (ESS)*, Kyiv, Ukraine, 2019, pp. 219-222. doi: https://doi.org/10.1109/ess.2019.8764202.

23. Ostroverkhov M., Chumack V., Monakhov E. Ouput Voltage Stabilization Process Simulation in Generator with Hybrid Excitation at Variable Drive Speed. *2019 IEEE 2nd Ukraine Conference on Electrical and Computer Engineering (UKRCON)*, Lviv, Ukraine, 2019, pp. 310-313. doi: https://doi.org/10.1109/ukrcon.2019.8879781.

24. Tytiuk V., Chornyi O., Baranovskaya M., Serhiienko S., Zachepa I., Tsvirkun L., Kuznetsov V., Tryputen N. Synthesis of a fractional-order $PI^{\lambda}D^{\mu}$-controller for a closed system of switched reluctance motor control. *Eastern-European Journal of Enterprise Technologies*, 2019, no. 2 (98), pp. 35-42. doi: https://doi.org/10.15587/1729-4061.2019.160946.

25. Zagirnyak M., Chornyi O., Zachepa I. The autonomous sources of energy supply for the liquidation of technogenic accidents. *Przeglad Elektrotechniczny*, 2019, no. 5, pp. 47-50. doi: https://doi.org/10.15199/48.2019.05.12.

26. Chornyi O., Serhiienko S. A virtual complex with the parametric adjustment to electromechanical system parameters. *Technical Electrodynamics*, 2019, pp. 38-41. doi: https://doi.org/10.15407/techned2019.01.038.

27. Shchur I., Kasha L., Bukavyn M. Efficiency Evaluation of Single and Modular Cascade Machines Operation in Electric Vehicle. *2020 IEEE 15th International Conference on Advanced Trends in Radioelectronics, Telecommunications and Computer Engineering (TCSET)*, Lviv-Slavske, Ukraine, 2020, pp. 156-161. doi: https://doi.org/10.1109/tcset49122.2020.235413.

28. Shchur I., Turkovskyi V. Comparative Study of Brushless DC Motor Drives with Different Configurations of Modular Multilevel Cascaded Converters. *2020 IEEE 15th International Conference on Advanced Trends in Radioelectronics,*

Telecommunications and Computer Engineering (TCSET), Lviv-Slavske, Ukraine, 2020, pp. 447-451. doi: https://doi.org/10.1109/tcset49122.2020.235473.
29. Ostroumov I., Kuzmenko N., Sushchenko O., Pavlikov V., Zhyla S., Solomentsev O., Zaliskyi M., Averyanova Y., Tserne E., Popov A., Volosyuk V., Ruzhentsev N., Dergachov K., Havrylenko O., Kuznetsov B., Nikitina T., Shmatko O. Modelling and simulation of DME navigation global service volume. *Advances in Space Research*, 2021, vol. 68, no. 8, pp. 3495-3507. doi: https://doi.org/10.1016/j.asr.2021.06.027.
30. Averyanova Y., Sushchenko O., Ostroumov I., Kuzmenko N., Zaliskyi M., Solomentsev O., Kuznetsov B., Nikitina T., Havrylenko O., Popov A., Volosyuk V., Shmatko O., Ruzhentsev N., Zhyla S., Pavlikov V., Dergachov K., Tserne E. UAS cyber security hazards analysis and approach to qualitative assessment. In: Shukla S., Unal A., Varghese Kureethara J., Mishra D.K., Han D.S. (eds) *Data Science and Security. Lecture Notes in Networks and Systems*, 2021, vol. 290, pp. 258-265. Springer, Singapore. doi: https://doi.org/10.1007/978-981-16-4486-3_28.
31. Zaliskyi M., Solomentsev O., Shcherbyna O., Ostroumov I., Sushchenko O., Averyanova Y., Kuzmenko N., Shmatko O., Ruzhentsev N., Popov A., Zhyla S., Volosyuk V., Havrylenko O., Pavlikov V., Dergachov K., Tserne E., Nikitina T., Kuznetsov B. Heteroskedasticity analysis during operational data processing of radio electronic systems. In: Shukla S., Unal A., Varghese Kureethara J., Mishra D.K., Han D.S. (eds) *Data Science and Security. Lecture Notes in Networks and Systems*, 2021, vol. 290, pp. 168-175. Springer, Singapore. doi: https://doi.org/10.1007/978-981-16-4486-3_18.
32. Sushchenko O.A. Robust control of angular motion of platform with payload based on H_∞-synthesis. *Journal of Automation and Information Sciences*, 2016, vol. 48, no. 12, pp. 13-26. doi: https://doi.org/10.1615/jautomatinfscien.v48.i12.20.
33. Chikovani V., Sushchenko O. Self-compensation for disturbances in differential vibratory gyroscope for space navigation. *International Journal of Aerospace Engineering*, 2019, vol. 2019, Article ID 5234061, 9 p. doi: https://doi.org/10.1155/2019/5234061.
34. Gal'chenko, V.Y., Vorob'ev, M.A. Structural synthesis of attachable eddy-current probes with a given distribution of the probing field in the test zone. *Russian Journal of Nondestructive Testing*, Jan. 2005, vol. 41, no. 1, pp. 29-33. doi: https://doi.org/10.1007/s11181-005-0124-7.
35. Halchenko, V.Y., Ostapushchenko, D.L. & Vorobyov, M.A. Mathematical simulation of magnetization processes of arbitrarily shaped ferromagnetic test objects in fields of given spatial configurations. *Russian Journal of Nondestructive Testing*, Sep. 2008, vol. 44, no. 9, pp. 589-600. doi: https://doi.org/10.1134/S1061830908090015.
36. Ostroumov I., Kuzmenko N., Sushchenko O., Zaliskyi M., Solomentsev O., Averyanova Y., Zhyla S., Pavlikov V., Tserne E., Volosyuk V., Dergachov K., Havrylenko O., Shmatko O., Popov A., Ruzhentsev N., Kuznetsov B., Nikitina T. A probability estimation of aircraft departures and arrivals delays. In: Gervasi O. et al. (eds) *Computational Science and Its Applications – ICCSA 2021. ICCSA 2021. Lecture Notes in Computer Science*, vol. 12950, pp. 363-377. Springer, Cham. doi: https://doi.org/10.1007/978-3-030-86960-1_26.
37. Chystiakov P., Chornyi O., Zhautikov B., Sivyakova G. Remote control of electromechanical systems based on computer simulators. *2017 International Conference on Modern Electrical and Energy Systems (MEES)*, Kremenchuk, Ukraine, 2017, pp. 364-367. doi: https://doi.org/10.1109/mees.2017.8248934.
38. Zagirnyak M., Bisikalo O., Chorna O., Chornyi O. A Model of the Assessment of an Induction Motor Condition and Operation Life, Based on the Measurement of the External Magnetic Field. *2018 IEEE 3rd International Conference on Intelligent Energy and Power Systems (IEPS)*, Kharkiv, 2018, pp. 316-321. doi: https://doi.org/10.1109/ieps.2018.8559564.
39. Ummels M. *Stochastic Multiplayer Games Theory and Algorithms*. Amsterdam University Press, 2010. 174 p.
40. Shoham Y., Leyton-Brown K. *Multiagent Systems: Algorithmic, Game-Theoretic, and Logical Foundations.* Cambridge University Press, 2009. 504 p.
41. Ray T., Liew K.M. A Swarm Metaphor for Multiobjective Design Optimization. *Engineering Optimization*, 2002, vol. 34, no. 2, pp. 141-153. doi: https://doi.org/10.1080/03052150210915.
42. Zilzter Eckart. *Evolutionary algorithms for multiobjective optimizations: methods and applications*. PhD Thesis Swiss Federal Institute of Technology, Zurich, 1999. 114 p.
43. Xiaohui Hu, Eberhart R.C., Yuhui Shi. Particle swarm with extended memory for multiobjective optimization. *Proceedings of the 2003 IEEE Swarm Intelligence Symposium*. SIS'03 (Cat. No.03EX706), Indianapolis, IN, USA, 2003, pp. 193-197. doi: https://doi.org/10.1109/sis.2003.1202267.
44. Pulido G.T., Coello C.A.C. A constraint-handling mechanism for particle swarm optimization. *Proceedings of the 2004 Congress on Evolutionary Computation* (IEEE Cat. No.04TH8753), Portland, OR, USA, 2004, vol. 2, pp. 1396-1403. doi: https://doi.org/10.1109/cec.2004.1331060.
45. Michalewicz Z., Schoenauer M. Evolutionary Algorithms for Constrained Parameter Optimization Problems. *Evolutionary Computation*, 1996, vol. 4, no. 1, pp. 1-32. doi: https://doi.org/10.1162/evco.1996.4.1.1.
46. Parsopoulos K.E., Vrahatis M.N. Particle swarm optimization method for constrained optimization problems. *Proceedings of the Euro-International Symposium on Computational Intelligence*, 2002, pp. 174-181.
47. Xin-She Yang, Zhihua Cui, Renbin Xiao, Amir Hossein Gandomi, Mehmet Karamanoglu. *Swarm Intelligence and Bio-Inspired Computation: Theory and Applications*, Elsevier Inc., 2013. 450 p.

Received 20.08.2021
Accepted 25.09.2021
Published 26.10.2021

B.I. Kuznetsov[1], *Doctor of Technical Science, Professor,*
T.B. Nikitina[2], *Doctor of Technical Science, Professor,*
I.V. Bovdui[1], *PhD, Senior Research Scientist,*
V.V. Kolomiets[3], *PhD, Associate Professor,*
B.B. Kobylianskiy[3], *PhD, Associate Professor,*
[1] State Institution «Institute of Technical Problems of Magnetism of the National Academy of Sciences of Ukraine», 19, Industrialna Str., Kharkiv, 61106, Ukraine.
e-mail: kuznetsov.boris.i@gmail.com (Corresponding author)
[2] Kharkov National Automobile and Highway University, 25, Yaroslava Mudroho Str., Kharkov, 61002, Ukraine,
e-mail: tatjana55555@gmail.com
[3] Educational scientific professional pedagogical Institute of Ukrainian Engineering Pedagogical Academy, 9a, Nosakov Str., Bakhmut, Donetsk Region, 84511, Ukraine,
e-mail: nnppiuipa@ukr.net

How to cite this article:
Kuznetsov B.I., Nikitina T.B., Bovdui I.V., Kolomiets V.V., Kobylianskiy B.B. Reduction of magnetic field level in residential old buildings from overhead power lines by means of active screening. *Electrical Engineering & Electromechanics*, 2021, no. 5, pp. 24-29. doi: https://doi.org/10.20998/2074-272X.2021.5.04.

UDC 621.3 https://doi.org/10.20998/2074-272X.2021.5.05

B. Bourouis, H. Djeghloud, H. Benalla

ENERGY EFFICIENCY OF A 3-LEVEL SHUNT ACTIVE POWER FILTER POWERED BY A FUEL-CELL / BATTERY DC BUS WITH REGULATED DUTY CYCLES

Introduction. *Nowadays, electrical energy is indispensable in industrial, tertiary and domestic appliances. However, its efficiency is becoming affected by the presence of the disturbances that appear in the electrical networks such as harmonics, unbalance, sags/swells, flickers …etc. Indeed, the disturbances cause a decrease in the power factor and an increase in the power losses. In this paper, the harmonic disturbance is considered and a 3-level shunt active power filter powered by a hybrid fuel-cell/battery DC is applied to mitigate current harmonic components from the electrical feeder.* ***Aim***. *Studying the energy efficiency of a system based on a 3-level shunt active filter powered by a hybrid fuel-cell / battery DC bus.* ***Methodology.*** *It is a matter of finding the suitable formulas that express the efficiency and the relative power losses according to the load factor (which is the ratio between the short-circuit active power and the load active power) and the load power factor. The DC bus energy is controlled using an energy management algorithm that contributes in generating the required reference input currents and output voltages of the fuel-cell and the battery. The DC/DC converters control circuits are performed in a closed loop by means of regulated duty cycles.* ***Results.*** *The simulation results carried-out under MATLAB/Simulink environment show better filtering quality if compared with the case of open loop control of the DC/DC converters and lesser differences between the fuel-cell power, the battery power and their respective reference powers. Which concerns the energy efficiency, the results demonstrate that higher efficiency and lower relative power losses can be achieved only when higher load factor and load power factor are attained. Therefore, the compensating system of the power factor is very important to improve the energy efficiency.* References 13, tables 1, figures 14.

Key words: **3-level shunt active power filter, hybrid fuel-cell / battery DC bus, energy efficiency, power quality, efficiency, relative power losses.**

Вступ. *У наш час електрична енергія є незамінною для промислових, проміжних і побутових приладів. Однак на її ефективність впливає наявність порушень, що виникають в електричних мережах, таких як гармоніки, дисбаланс, провисання/розбухання, мерехтіння тощо. Дійсно, порушення викликають зменшення коефіцієнта потужності та збільшення втрат потужності. У цій роботі розглянуто гармонічні порушення та застосовано 3-рівневий шунтуючий фільтр активної потужності з живленням від гібридного паливного елемента/акумулятора постійного струму для пом'якшення струмових гармонічних компонентів з електропостачанням від електричного фідера.* ***Мета***. *Дослідження енергоефективності системи на основі 3-рівневого шунтуючого активного фільтра з живленням від гібридної шини постійного струму з паливним елементом/акумулятором.* ***Методика***. *Потрібно знайти відповідні формули, які виражають ефективність та відносні втрати потужності у відповідності до коефіцієнта навантаження (це відношення активної потужності короткого замикання та активної потужності навантаження) та коефіцієнта потужності навантаження. Енергія шини постійного струму контролюється за допомогою алгоритму управління енергією, який сприяє формуванню необхідних опорних вхідних струмів та вихідних напруг паливного елемента й акумулятора. Схеми управління DC/DC перетворювачами виконуються у замкненому контурі за допомогою регульованих робочих циклів.* ***Результати***. *Результати моделювання, проведеного у середовищі MATLAB/Simulink, показують кращу якість фільтрації у порівнянні з випадком управління з відкритим контуром DC/DC перетворювачів та менші відмінності між потужністю паливних елементів, потужністю акумулятора та їх відповідною порівняльною потужністю. Що стосується енергоефективності, результати показують, що більший ККД та менші відносні втрати потужності можна досягти лише тоді, коли досягаються більший коефіцієнт навантаження та коефіцієнт потужності навантаження. Тому компенсуюча система коефіцієнта потужності дуже важлива для підвищення енергоефективності.* Бібл. 13, табл. 1, рис. 14.

Ключові слова: **3-рівневий шунтуючий фільтр активної потужності, гібридна шина постійного струму з паливним елементом/акумулятором, енергоефективність, якість електроенергії, ККД, відносні втрати потужності.**

1. Introduction. The study of the electrical systems energy efficiency is very important since electricity is the most flexible type of energy and one of the most significant energies used in industry and in domestic appliances. Particularly, for systems containing power quality compensators based on power electronics interfaces, it is interesting to study the influence on the global system efficiency. Indeed, when the power quality is poor, power losses increase which decreases the efficiency [1-3]. Active power filters (APFs) are classified among the most effective power quality compensators that can reduce the power losses according to the adopted compensation approach and consequently improve the energy efficiency [4, 5]. Particularly, the shunt active power filter (SAPF) generates a current which reactive component goes into the non-linear load whereas the active component flows into the source while guarantying less power losses and near-unity power factor (in spite of the energy losses in the APF electronic devices) [6, 7]. The study of the energy efficiency of a compensated power system can be performed depending on the power system topology, the existent disturbances that increase the power losses and the compensation approach. In the literature most studies concern the energy efficiency of four-wire power systems taking into account the neutral current in presence of harmonic disturbance and considering the instantaneous power theory in the compensation approach [4, 6-8]. Especially, the study presented by Artemenko and Batrak in [6] establishes new formulas that call the load factor (ratio between the short-circuit power and the load active power) and the load power factor when expressing the system global efficiency and relative power losses. The study demonstrates that more the load factor and the power factor are higher, the efficiency is higher and the relative

power losses are lower which means better energy efficiency.

In the present work, the formulas of Artemenko and Batrak are adopted on a three-phase three-wire system considering a 3-level neutral point clamped (NPC) SAPF powered by a hybrid fuel-cell (FC) / battery DC bus which power is supervised by a management energy algorithm associated to DC/DC boost and buck converters where the duty cycles are closed-loop controlled.

The **purpose** of the work is studying the energy efficiency of a system based on a 3-level shunt active filter powered by a hybrid fuel-cell / battery DC bus.

The present work is organized as follows. Section 2 describes the global system. Section 3 is dedicated to the SAPF and the DC bus topologies and control strategies. Section 4 establishes the theoretical study of the energy efficiency according to Artemenko and Batrak approach. Section 5 presents and discusses the simulation results carried-out using MATLAB/Simulink.

2. Active filtering system description. The considered system is depicted in Fig. 1. The system contains the electric feeder (with its electromotive force (EMF) e_s, its series R_s, L_s impedance, and its current i_s) to be cleaned from harmonic currents (produced by the load), the non-linear load (a diode rectifier and a DC R_l, L_l load) and the proposed 3-level NPC IGBT's active power filter configuration (with its output filter R_f, L_f, C_f and its upstream filter R_u, L_u) which DC bus (including the filtering capacity C_{dc} with its shunt resistor R_{dc}) is fed with a DC voltage V_{dc} through a hybrid system of a FC and a battery, power electronically interfaced by DC/DC boost and buck converters. The detailed description of this hybrid power DC bus and the energy management system are presented in [9]. Duty cycles controllers of DC/DC converters and energy efficiency of the AC side are shown in the following sections.

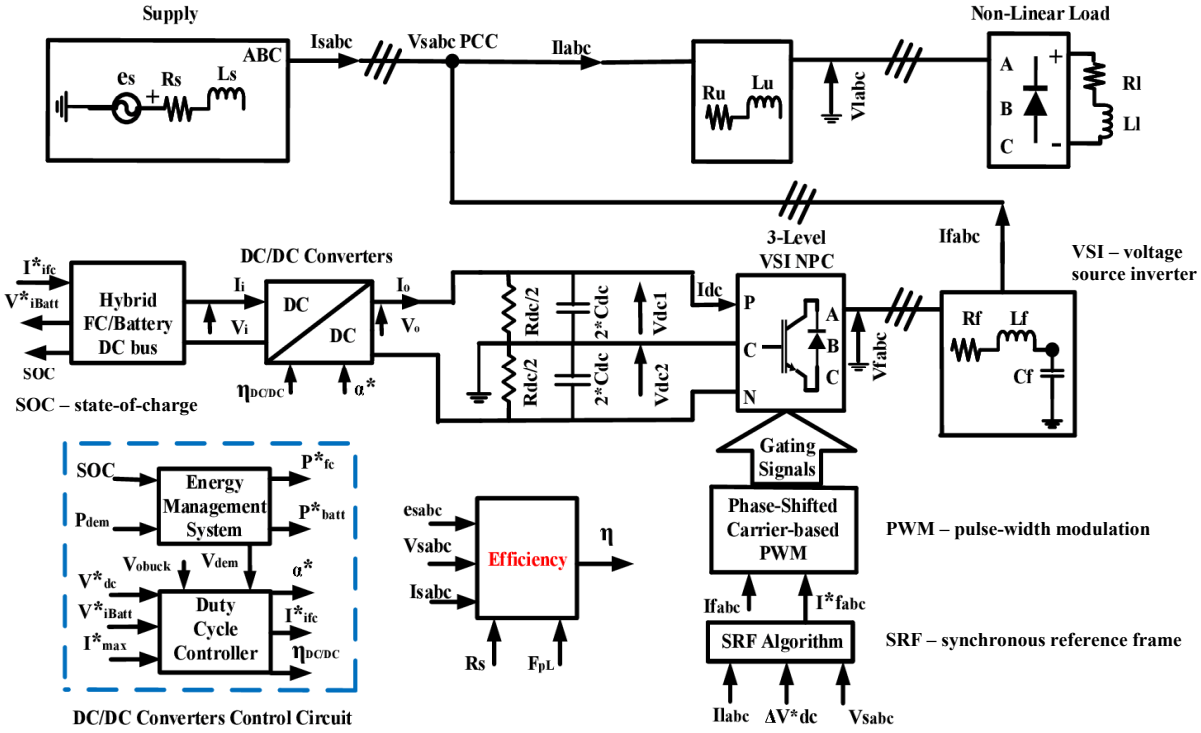

Fig. 1. Description of system

3. SAPF and DC/DC converters topologies and control strategies. As said previously, the SAPF is based on a NPC 3-level voltage inverter and the DC bus feeding the SAPF with DC voltage. The DC bus is based on an association of a FC, a battery and DC/DC boost and buck converters. Topologies and control strategies of the SAPF and the DC/DC converters are presented in this section.

3.1. SAPF. Figure 2 illustrates the power circuit of the SAPF constituted of a DC voltage bus, a NPC 3-level voltage inverter and an output RLC filter. The control strategy of the SAPF is shows in Fig. 3. It uses the synchronous reference frame (SRF) to detect the reference harmonic current I^*_f, PI correctors to regulate the input DC voltage V_{dc} and the output AC current I_f, and a phase-shifted carrier-based modulator for gating signals generation. The PI correctors coefficients of the voltage regulator (K_{pVdc}, K_{iVdc}) and the current regulator (K_{pIf}, K_{iIf}) are designed using Bode method. Their expressions are extracted by the help of (1) to (8) [10] starting from the open loop transfer functions (OLTF) of the DC voltage $OLTF_{Vdc}(p)$ and the AC current $OLTF_{If}(p)$.

3.2. V_{dc} regulator

$$OLTF_{V_{dc}}(p) = \left(1 + \frac{K_{pV_{dc}}}{K_{iV_{dc}}} s\right) \Big/ \frac{a}{K_{iV_{dc}}} s^2; \quad (1)$$

where

$$a = \frac{C_{dc} \cdot V^*_{dc}}{3V_{srms}}; \quad (2)$$

$$K_{pV_{dc}} = \frac{K_{iV_{dc}}}{\omega_1}, \quad K_{iV_{dc}} = a \cdot \omega_0^2; \quad (3)$$

$$\omega_1 = \frac{\omega_c}{\tan(\phi_1(\omega_c)+\pi)}; \quad (4)$$

$$\omega_0 = \frac{\omega_c}{e^{0.25\cdot\log(10)\cdot\log_{10}\left(1+\left(\frac{\omega_c}{\omega_1}\right)^2\right)}}, \quad (5)$$

where ω_c is the cutting frequency in the DC state generally chosen inferior to the fundamental frequency; $\phi_1(\omega_c)$ is the angle belonging to the phase margin, and ω_0, ω_1 are the particular frequencies of the Bode diagram.

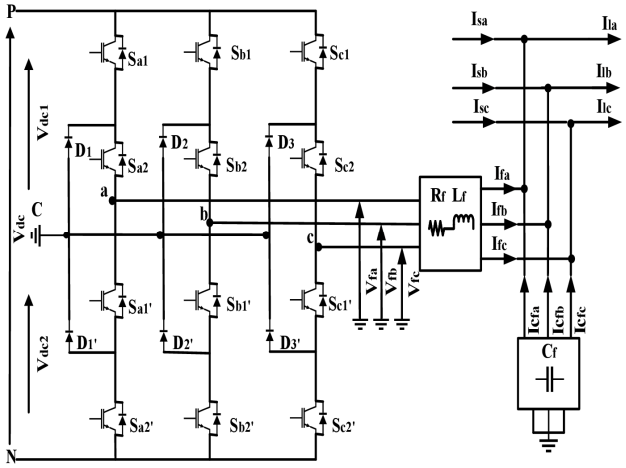

Fig. 2. SAPF topology

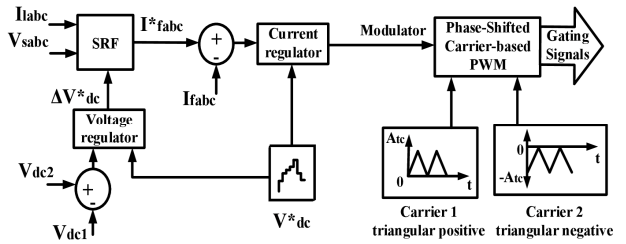

Fig. 3. SAPF control strategy

3.3. I_f regulator

$$OLTF_{I_f}(p) = \left(1+\frac{K_{pI_f}}{K_{iI_f}}s\right) \Big/ \frac{b}{K_{iI_f}}s^2; \quad (6)$$

where

$$b = \frac{20A_{tci}\cdot L_f}{V_{dc}^*}; \quad (7)$$

where A_{tci} is the amplitude of the triangular carrier.

In the case of the PI regulation of the AC output current I_f, and in order to reduce the dragging error between I_f and its reference I_f^*, the passing-band of the PI regulator should be inferior to the cutting frequency f_c. Practically, ω_c is taken $0.5\pi\cdot f_c$ [11].

3.4. DC/DC converters. Figure 4 exhibits the topology of DC/DC converters. The FC DC/DC converter is unidirectional and operates in boost mode, whereas that of the battery is bidirectional and operates in boost and buck modes [9]. The power circuits in both operating modes are based on the average model allowing controlling the input voltage V_i and the output current I_o using regulated duty cycles α^*_{boost}, α^*_{buck} and the efficiencies η_{boost}, η_{buck} obtained from a 2-D look-up table which data is provided by the manufacturer BRUSA [12]

$$V_i^* = (1-\alpha^*_{boost})\cdot V_o; \quad (8)$$

$$I_o^* = \eta_{boost}(1-\alpha^*_{boost})\cdot I_i; \quad (9)$$

where V_i, I_i are the voltage and current at the low voltage side; V_o, I_o are the voltage and current at the high voltage side.

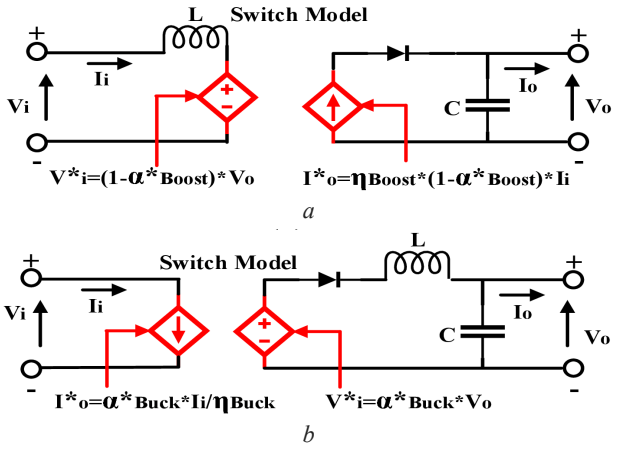

Fig. 4. DC/DC power circuit:
a – Boost mode; *b* – Buck mode

Figure 5 summarizes the principle of the control circuit with voltage and current regulators of FC and battery in boost mode (Fig. 5,*a*,*b*) and battery in buck mode (Fig. 5,*c*). One can deduce that α^*_{boost} is regulated starting from V^*_{dc} while α^*_{buck} can be regulated from V^*_{ibatt}.

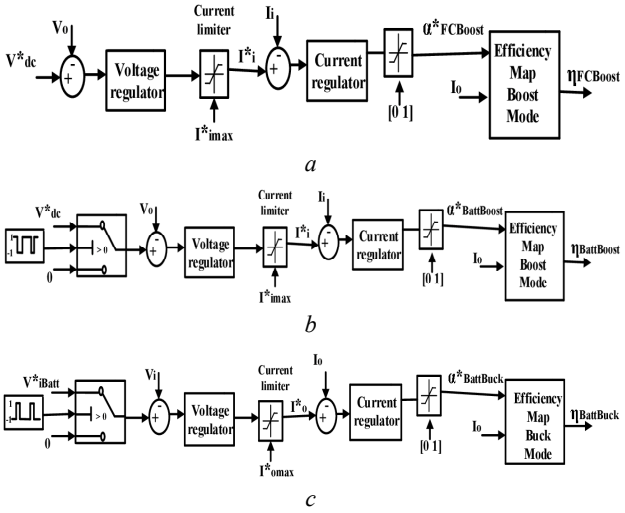

Fig. 5. DC/DC control circuit:
a – fuel-cell; *b* – Battery in Boost mode;
c – Battery in Buck mode

Dimensioning of voltage and current regulators. The inductor L voltage and capacitor C current can be expressed as:

$$L\frac{dI_i}{dt} = V_i - (1-\alpha^*_{boost})\cdot V_o; \quad (10)$$

$$C\frac{dV_o}{dt} = \eta_{boost}(1-\alpha^*_{boost})\cdot I_i - I_o. \quad (11)$$

This gives the inductor current and capacitor voltage in Laplace domain as:

$$I_i(s) = \frac{V_i - (1-\alpha^*_{boost})\cdot V_o}{L\cdot s}; \quad (12)$$

$$V_o(s) = \frac{\eta_{boost}(1-\alpha^*_{boost})\cdot I_i - I_o}{C\cdot s}; \quad (13)$$

$$\Rightarrow V_o(s) = \frac{\eta_{boost}\left(\frac{V_i^*}{V_0}\right)\cdot I_i - I_o}{C\cdot s}. \quad (14)$$

Then, the open loop transfer functions are given by:

$$OLTF_I(s) = \frac{K_{PI}s + K_{II}}{s}\cdot\frac{1}{L\cdot s}; \quad (15)$$

$$OLTF_V(s) = \frac{K_{PV}s + K_{IV}}{s}\cdot\frac{1}{C\cdot s}; \quad (16)$$

where the proportional gains K_{PI}, K_{PV} and integral gains K_{II}, K_{IV} are determined knowing the regulator response times as [13]:

$$K_{PI} = 2\zeta\omega_{NI}L, K_{II} = \omega_{NI}^2 L; \quad (17)$$

$$K_{PV} = 2\zeta\omega_{NV}C, K_{IV} = \omega_{NV}^2 C; \quad (18)$$

where

$$\zeta\omega_{NI} = \frac{-\ln\left(0.05\sqrt{1-\zeta^2}\right)}{T_{RI}}; \quad (19)$$

$$\zeta\omega_{NV} = \frac{-\ln\left(0.05\sqrt{1-\zeta^2}\right)}{T_{RV}}, \quad (20)$$

where ω_{NI}, ω_{NV} are the current and voltage controller bandwidth respectively; ζ is the damping coefficient; T_{RI}, T_{RV} are the current and voltage controller response times respectively. T_{RI} is chosen to be one tenth of T_{RV}.

Similar to the model of the DC/DC boost converter, the DC/DC buck converter is shown in Fig. 4,b

$$V_o = \alpha^*_{buck}\cdot V_i^*; \quad (21)$$

$$I_o^* = \frac{I_i\cdot\eta_{buck}}{\alpha^*_{buck}}. \quad (22)$$

From the average model, the inductor L current and capacitor C voltage can be expressed in Laplace domain as:

$$I_o(s) = \frac{\alpha^*_{buck}V_i^* - V_o}{L\cdot s}; \quad (23)$$

$$V_o(s) = \frac{I_o - \eta_{buck}\left(\frac{V_i}{V_o}\right)\cdot I_i}{C\cdot s}. \quad (24)$$

Similar to the DC/DC boost converter control. The PI controllers gains of the buck converter control circuit are also determined using (15)–(20).

4. Study of the energy efficiency. In this section, the study aims to extract the relative power losses X and the efficiency η depending on the load factor K_L and the load power factor P_F [6, 7]. Since the power losses are mainly caused by the dispersed power in the wires resistances in the source, then in the following equations development only the source resistance R_s will be considered.

The load factor is defined as the ratio between the short-circuit power P_0 and the load power P_l:

$$K_L = P_0/P_l; \quad (25)$$

where P_0 is the maximum power that can be provided to the disturbing load without reaction of the protecting equipment (fuses and circuit-breakers). Its expression is given by:

$$P_0 = \frac{1}{T}\int_0^T e_s^T(t)R_s^{-1}e_s(t)dt; \quad (26)$$

where e_s is the vector of the instantaneous values of the source voltage:

$$e_s(t) = \begin{bmatrix} e_{sa}(t) \\ e_{sb}(t) \\ e_{sc}(t) \end{bmatrix}; \quad (27)$$

where R_s is the matrix of resistance losses in the cables of the power system:

$$R_s = \begin{bmatrix} R_s & 0 & 0 \\ 0 & R_s & 0 \\ 0 & 0 & R_s \end{bmatrix}; \quad (28)$$

where P_l is the load power formulated by:

$$P_l = \frac{1}{T}\int_0^T V_s^T(t)I_l(t)dt; \quad (29)$$

where V_s, I_l are the respective vectors of instantaneous values of common coupling point voltage and load current:

$$V_s(t) = \begin{bmatrix} V_{sa}(t) \\ V_{sb}(t) \\ V_{sc}(t) \end{bmatrix}, \quad I_l(t) = \begin{bmatrix} I_{la}(t) \\ I_{lb}(t) \\ I_{lc}(t) \end{bmatrix}; \quad (30)$$

where P_F is conventionally defined as the ratio between P_l and the apparent power S given by [6]:

$$S = \sqrt{\frac{1}{T}\int_0^T V_s^T(t)R_s^{-1}V_s(t)dt\int_0^T I_s^T(t)R_sI_s(t)dt}; \quad (31)$$

where I_s is the vector of instantaneous values of the source current:

$$I_s(t) = \begin{bmatrix} I_{sa}(t) \\ I_{sb}(t) \\ I_{sc}(t) \end{bmatrix}. \quad (32)$$

The power losses ΔP are the difference between the source power P_s given by:

$$P_s = \frac{1}{T}\int_0^T e_s(t)I_s(t)dt; \quad (33)$$

and P_l:

$$\Delta P = P_s - P_l; \quad (34)$$

on the other hand ΔP can be expressed by:

$$\Delta P = \frac{1}{T}\int_0^T I_s^T(t)R_sI_s(t)dt \Rightarrow \frac{S^2}{\frac{1}{T}\int_0^T V_s^T(t)R_s^{-1}V_s(t)dt}. \quad (35)$$

The term $1/T\int_0^T V_s^T(t)R_s^{-1}V_s(t)dt$ corresponds to the useful power at the common coupling point P_u:

$$P_u=\frac{1}{T}\int_0^T V_s^T(t)R_s^{-1}V_s(t)dt=$$

$$=P_u=\frac{1}{T}\int_0^T[e_s(t)-R_sI_s(t)]R_s^{-1}[e_s(t)-R_sI_s(t)]dt=$$

$$=\frac{1}{T}\int_0^T e_s^T(t)R_s^{-1}e_s(t)dt-\frac{1}{T}\int_0^T I_s^T(t)R_sR_s^{-1}e_s(t)dt-$$

$$-\frac{1}{T}\int_0^T e_s^T(t)R_s^{-1}R_sI_s(t)dt+\frac{1}{T}\int_0^T I_s^T(t)R_sR_s^{-1}R_sI_s(t)dt= \quad (36)$$

$$=\frac{1}{T}\int_0^T e_s^T(t)R_s^{-1}e_s(t)dt-\frac{1}{T}\int_0^T I_s^T(t)e_s(t)dt-$$

$$-\frac{1}{T}\int_0^T e_s^T(t)I_s(t)dt+\frac{1}{T}\int_0^T I_s^T(t)R_sI_s(t)dt=$$

$$=P_0-P_s-P_s+\Delta P=P_0-P_s-P_s+P_s-P_l;$$

$$\Rightarrow P_u=P_0-P_s-P_l.$$

The efficiency η is the ratio between the load power and the source power:

$$\eta=\frac{P_l}{P_s}=\frac{P_l}{P_l+\Delta P}=\frac{1}{1+\frac{\Delta P}{P_l}}; \quad (37)$$

From $P_F=P_l/S$, one can conclude that:

$$\Delta P=\frac{S^2}{P_u}=\frac{P_l^2}{P_F^2+P_u}; \quad (38)$$

$$\eta=\frac{1}{1+\frac{P_l}{P_F^2(P_0-P_s-P_l)}}; \quad (39)$$

$$\Rightarrow \eta P_F^2P_0-\eta P_F^2P_s-\eta P_F^2P_l+\eta P_l- \quad (40)$$
$$-P_F^2P_0+P_F^2P_s+P_F^2P_l=0;$$

$$\Rightarrow \eta P_F^2\frac{P_0}{P_l}-\eta P_F^2\frac{P_s}{P_l}-\eta P_F^2+\eta- \quad (41)$$
$$-P_F^2\frac{P_0}{P_l}+P_F^2\frac{P_s}{P_l}+P_F^2=0;$$

$$\Rightarrow \eta^2\left(1+(P_F^2(K_L-1))\right)-P_F^2K_L\eta+P_F^2=0. \quad (42)$$

The determinant of (42) is given by:

$$\Delta=\left(K_L^2-4K_L+4\right)P_F^4-4P_F^2>0; \quad (43)$$

$$\Delta>0\Rightarrow\frac{K_L^2}{4}-K_L+1-\frac{2}{P_F^2}>0 \quad (44)$$
$$\Rightarrow K_L>2+\frac{2}{P_F};$$

$$\Rightarrow \eta=\frac{P_FK_L+\sqrt{(K_L-2)^2P_F^2-4}}{2\left(\frac{1}{P_F}+P_F(K_L-1)\right)}. \quad (45)$$

On the other hand and using the relative power losses X ($X=\Delta P/P_l$) in the efficiency formula:

$$\eta=\frac{1}{1+X}\Rightarrow X=\frac{1}{\eta}-1. \quad (46)$$

5. Simulation results discussion. In this section simulation works about the previous study are presented. They were carried out using MATLAB/Simulink software and considering the parameters reported in Table 1.

Table 1

Simulation parameters

Parameter	Value
$P_{fc\text{nom}}$, $P_{bat\max}$	24 kW, 21 kW
P_{fclow}, P_{fchigh}	1.6452 kW, 13.348 kW
P_{fcidle}, initial SOC	316.2 W, 80.1 %
AC supply voltage, f	$V_{sl\text{-}l\max}$ = 400 V, f = 50 Hz
Maximum source current	$I_{s\max}$ = 60.01 A
Supply impedance	R_s = 0.5414 Ω, L_s = 1.7 mH
Rectifier load	R_l = 8.4 Ω, L_l =50 mH
Output filter impedance	R_f = 2.063 Ω, L_f = 1 mH, C_f = 30 μF
Upstream impedance	R_u = 0.42 Ω, L_u = 41.563 mH
DC-bus	$V_{dc\max}$ = 1694 V, C_{dc} = 617.18 μF, R_{dc} = 60 Ω, L_{dc} = 0.5 mH
PI voltage	f_{cVdc} = 20 Hz, ϕ_{cVdc} = 89.9°
PI current	f_{clf} = 10 kHz, ϕ_{clf} = 89.9°

Figure 6 present the imposed values of the state-of-charge SOC (Fig. 6,*a*) and the regulated duty cycles $\alpha^*_{FCBoost}$, $\alpha^*_{BattBoost}$ and $\alpha^*_{BattBuck}$ (Fig. 6,*b*).

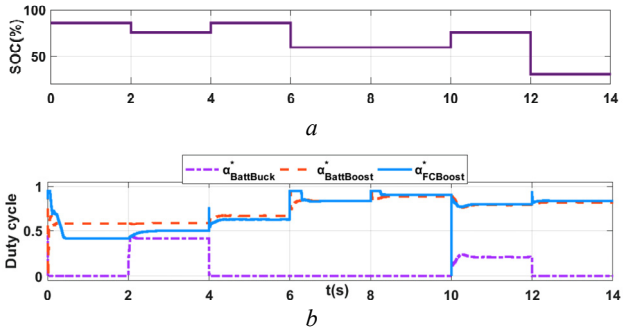

Fig. 6. *a* – the imposed state-of-charge (SOC); *b* – regulated duty cycles of DC/DC FC and battery converters

The imposed SOCs were chosen to meet the energy management algorithm cases [9]; their values vary between 35 % to 85 %. Accordingly, the regulated duty cycles of the boost mode of the DC/DC converters vary between 0.41 and 0.9 for the FC converter and between 0.58 and 0.88 for the battery converter. In the case of the battery buck mode, the duty cycle varies between 0 and 0.4. Since the battery begins alone to feed the DC bus until the

FC enters in operation, $\alpha^*_{BattBoost}$ is superior to $\alpha^*_{FCBoost}$. Then, the two duty cycles become superimposed in their evolution once the FC is operational. For the case of $\alpha^*_{BattBuck}$, one can observe that it is null all the time except when the battery is in the charging mode (case of $P_{fcidle}<P_{dem}<P_{fclow}$ and SOC<80 %, and $P_{dem}>P_{fclow}$ and SOC<80 % [9]). The value of $\alpha^*_{BattBuck}$ is low because of the low percentage of the battery discharge.

Now, which concerns the different considered powers (P_{dem}, P_{fc}, P_{batt}), the results are displayed in Fig. 7. The results are presented into two shutters. The first one deals with the obtained powers before regulating the duty cycles (Fig. 7,*a*) while the second one shows the powers after activating the duty cycle regulation loops (Fig. 7,*b*). It is obvious that there are some differences, especially for P_{fc} and P_{batt} from their respective reference values obtained from the energy management algorithm [9], before regulating the DC/DC converters duty cycles (Fig. 7,*a*). However, the differences disappear when the duty cycles are regulated (Fig. 7,*b*).

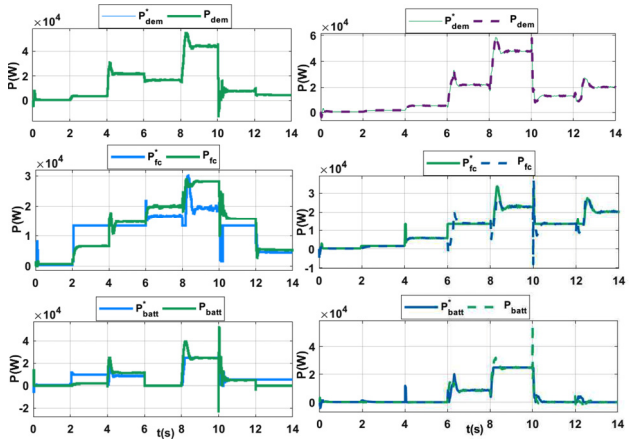

a *b*

Fig. 7. Reference and measured powers of the demand, the FC and the battery.
a – before duty cycles regulation; *b* – after duty cycles regulation

Figure 8 depicts the input/output currents and voltages, with their respective references, of the DC/DC converters. Figure 8,*a* shows the FC input reference current I^*_{ifc}, the FC input measured I_{ifc} and the measured output current I_{ofc}. Notably, I_{ifc} is perfectly following its reference I^*_{ifc}. Which concerns I_{ofc}, it is all time inferior to I_{ifc} because of the boost mode of the FC DC/DC converter. The same observation can be pointed-out for Fig. 8,*b* concerning the battery currents in the boost mode of its converter. Figure 8,*c* shows the battery currents when its converter is in the buck mode where low values are noted compared to the boost mode values. Figure 8,*d* presents the demand current measured I_{dem} in the DC bus which is the sum of I_{ofc} and I_{obatt}. Similar remarks can be given for the different input/output voltages (Fig. 8,*e* to Fig. 8,*g*), only this time, output voltages are superior to input voltages in the boost mode (Fig. 8,*e* and Fig. 8,*f*) and vice-versa in the buck mode (Fig. 8,*g*). Finally, Fig. 8,*h* portrays the demand voltage superimposed to its reference. Different reference voltage levels were imposed in order to meet the energy management algorithm cases [9].

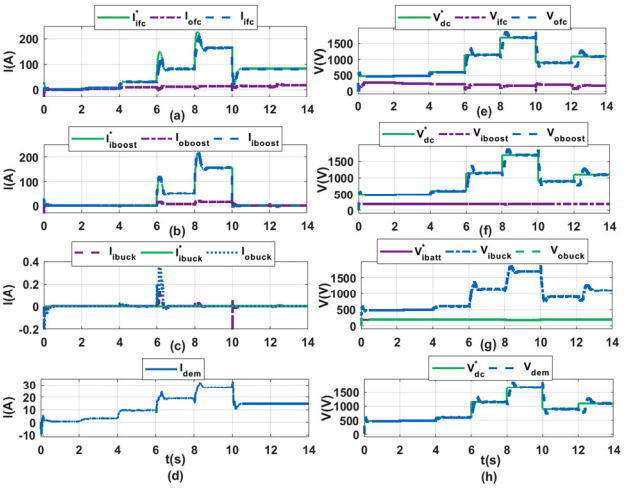

Fig. 8. Input and output measured and reference currents and voltages of DC/DC converters:
a – DC/DC FC boost converter currents;
b – DC/DC battery boost converter currents;
c – DC/DC battery buck converter currents;
d – the demand current;
e – DC/DC FC boost converter voltages;
f – DC/DC battery boost converter voltages;
g – DC/DC battery buck converter voltages;
h – the demand voltage

Figure 9 concerns the filtering instantaneous results in the AC feeder of Fig. 1 after inserting the SAPF. The displayed curves are related to the 3-phase current absorbed by nonlinear load (Fig. 9,*a*), the AC source 3-phase current (Fig. 9,*b*) and the 3-phase point of common coupling (PCC) voltage (Fig. 9,*c*). It is noted that the load current is hardly distorted while the source current and voltage are near-sinusoidal waves.

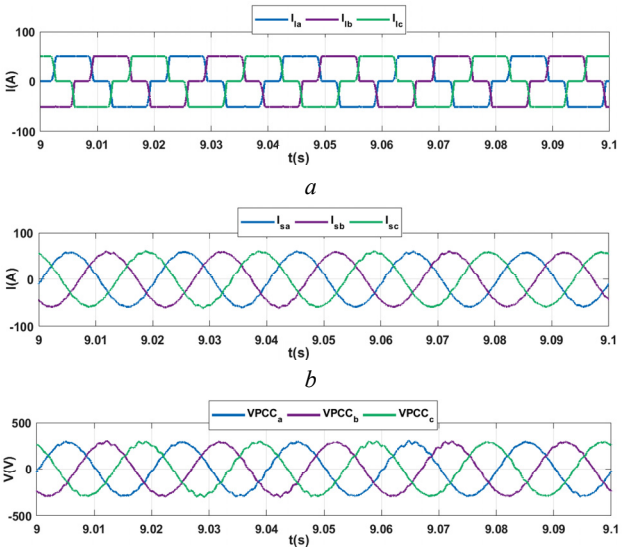

a

b

c

Fig. 9. Results after inserting the SAPF:
a – load current; *b* – source current; *c* – PCC voltage

The harmonic spectrums shown in Fig. 10 provide frequency analysis before and after inserting the

regulation loops of the DC/DC converters duty cycles. The total harmonic distortion (THD) of the load current is around 25 % (Fig. 10,*a*), the THD of the source current before regulating the duty cycles is 2.38 % (Fig. 10,*b*) and the source voltage THD is 3.03 % (Fig. 10,*c*). After inserting the duty cycles regulation loops the source current and voltage THDs % decrease respectively to 2.08 % (Fig. 10,*d*) and 2.92 % (Fig. 10,*e*) which means an improvement in the filtering quality when activating the regulation of the DC/DC converters duty cycles.

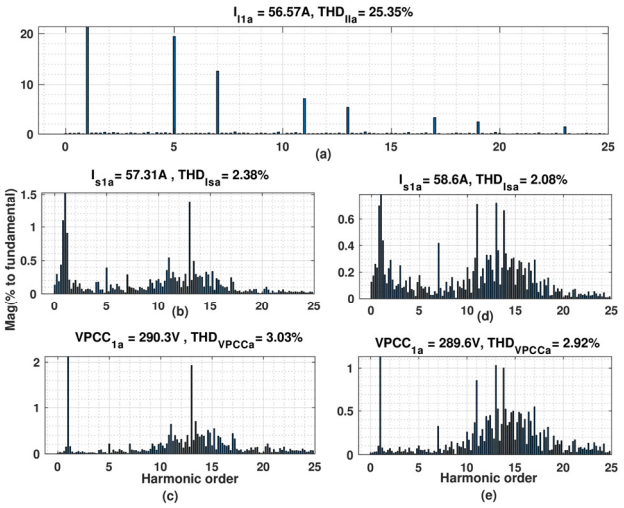

Fig. 10. Harmonic spectrum of: *a* – load current. Before duty cycles regulation: *b* – source current; c – PCC voltage. After duty cycles regulation: *d* – source current; *e* – PCC voltage

In Fig. 11 the results concerning the SAPF are presented.

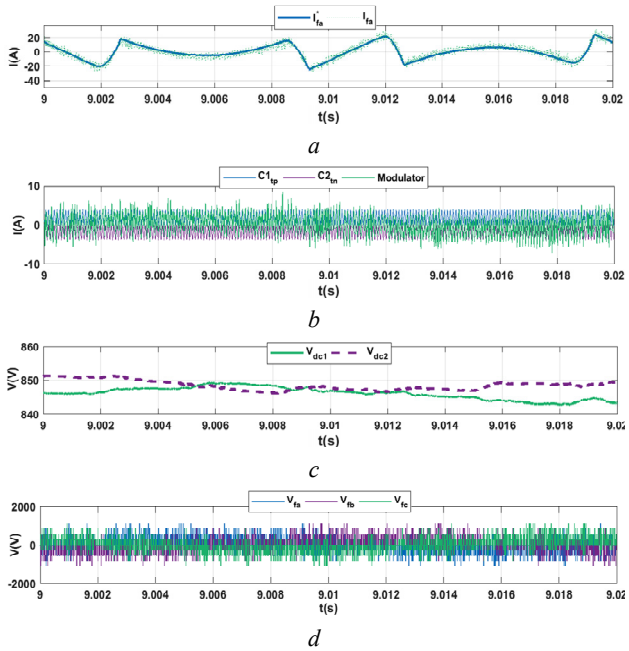

Fig. 11. A zoom in for V^*_{dc} = 1694 V: *a* – the APF current I_f with its reference; *b* – modulator with carriers; *c* – DC-bus voltage levels; *d* – output filter voltage

Figure 11,*a* shows the current of the SAPF with perfect agreement with its reference. Figure 11,*b* illustrates the modulating signal ($I^*_f - I_f$) varying inside its carrier signal which means a satisfying operation of the considered pulse-width modulation (PWM) strategy. In Fig. 11,*c* the regulated two voltages of the DC bus V_{dc1} and V_{dc2} are presented. One can observe that they evolve in an opposite manner around $V^*_{dc}/2$ (the case of V^*_{dc} = 1694 V is considered). Finally, the output voltages of the SAPF are shown in Fig. 11,*d* where 3-levels can be read: $\approx 2V^*_{dc}/3$ (1126 V), $\approx V^*_{dc}/2$ (845 V), and $\approx V^*_{dc}/3$ (565 V) which demonstrates a good behavior of the 3-level SAPF.

Figure 12 concerns the power quality characterization using the instantaneous THDs of the source current and voltage (Fig. 12,*a*), the source current unbalance rate (CUR) (Fig. 12,*b*) and both power factors of the source and load (Fig. 12,*c*). During a transient state of 4 s, the THDs are exceeding the standardization limits (5 %). After that, they remain below the limit. The CUR is all time low, and the source power factor is near-unity.

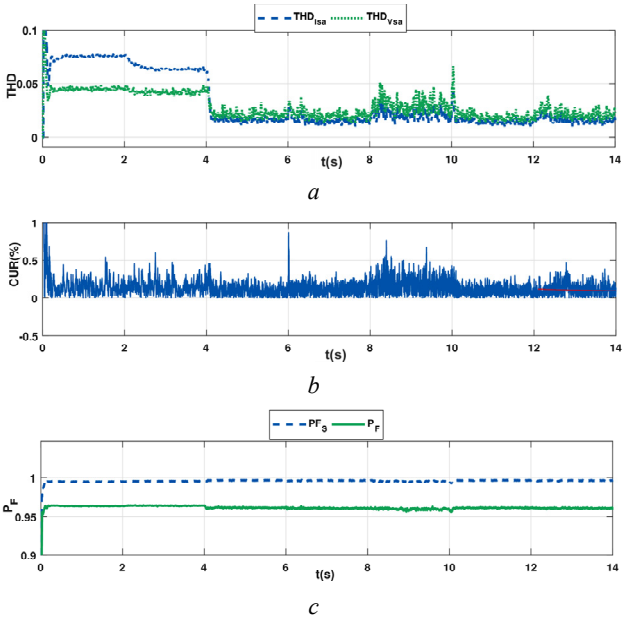

Fig. 12. Curves: *a* – total harmonic distortion THD; *b* – current unbalance rate (CUR); *c* – power factor

Figure 13 presents the obtained result from the energy efficiency study of the system of Fig. 1.

Figure 13,*a* depicts the short-circuit power P_0 that increases linearly from 0 and stabilizes at 293 kW after 0.02 s. Figure 13,*b* shows the load power P_l which stabilizes at 23.31 kW. Figure 13,*c* illustrates the ratio between P_0 and P_l describing a decreasing curve that stabilizes at 12.36 while the power factor P_F of Fig. 13,*d* is an increasing curve that trends towards 0.96 (near-unity value). In Fig. 13,*e* one can observe that (44) (K_L>2+(2/P_F)) is satisfied all-time.

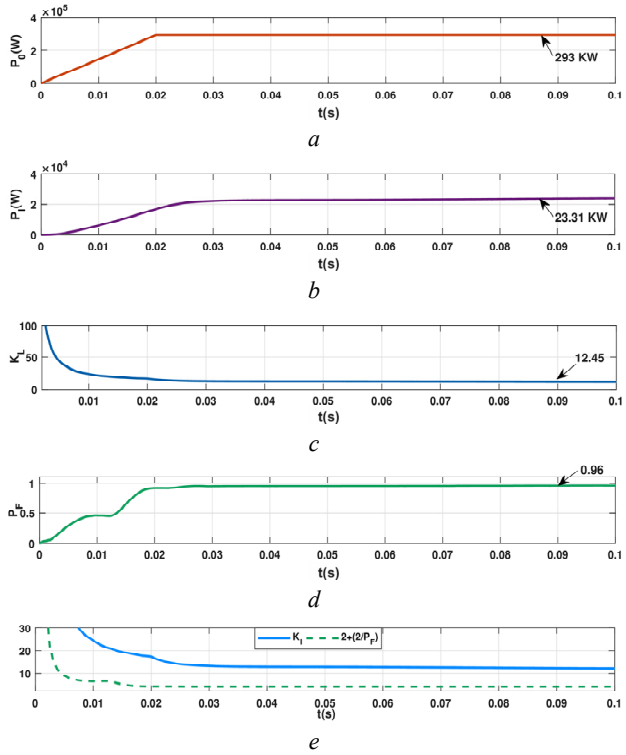

Fig. 13. The instantaneous: *a* – short-circuit power; *b* – load power; *c* – load factor; *d* – load power factor; *e* – K_L and $2+(2/P_F)$

Figure 14 concerns the results about the relative power losses X and the efficiency η. As shown in Fig. 14,*a* presenting X vs. P_F for different values of K_L, the relative power losses X decrease when both P_F and K_L increase. The same observation can be pointed-out for X vs. K_L for different values of P_F (Fig. 14,*b*). Now, for the efficiency η, one can observe that it increases when P_F and K_L increase as portrayed in Fig. 14,*c* (η vs. P_F for different values of K_L) and Fig. 14,*d* (η vs. K_L for different values of P_F).

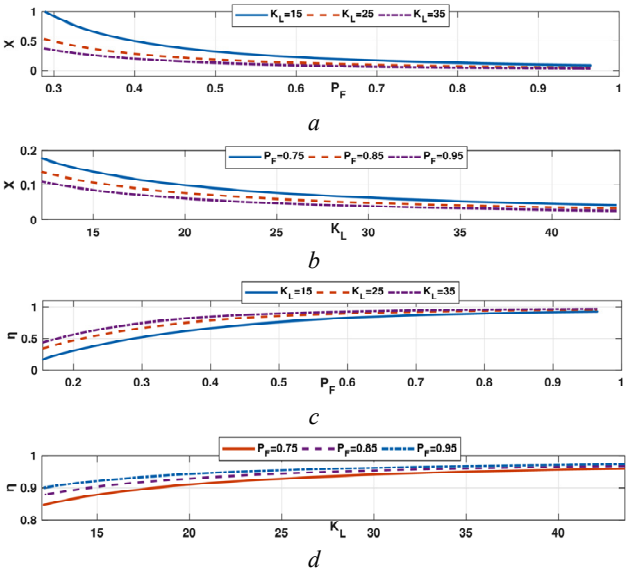

Fig. 14. Variation of: *a* – the power losses X vs. P_F for different value of K_L; *b* – the power losses X vs. K_L for different value of P_F; *c* – the efficiency η vs. P_F for different value of K_L; *d* – the efficiency η vs. K_L for different value of P_F

Conclusions.

In this paper, the focus was on studying the energy efficiency of a system based on a 3-level shunt active filter powered by a hybrid FC/battery DC bus. The first part of the presented and discussed works concerned the duty cycles regulation of the DC/DC converters controlling the powers of the FC, the battery and the demand together with an energy management algorithm. When comparing the obtained powers before and after regulation of the duty cycles, it was obvious that better following of these powers to their references (obtained from the energy management algorithm) is reached for a regulated duty cycle. The second part of the works concerned the energy efficiency study tacking into-account the short circuit power, the load power; the ratio between them noted the load factor and the load power factor. The studies were established on the relative power losses and the efficiency. The theoretical equations and simulation results demonstrate that more the load factor and the load power factor are increasing, more the power losses decrease and the efficiency increases. Future works are based on developing an optimization algorithm that improves the whole system behavior.

Conflict of interest. The authors declare that they have no conflicts of interest.

REFERENCES

1. Sumper A., Baggini A. *Electrical Energy Efficiency: Technologies and Applications*. John Wiley & Sons, Ltd, 2012. 402 p. doi: https://doi.org/10.1002/9781119990048.

2. Kuznetsov V., Tryputen N., Kuznetsova Y. Evaluating the effect of electric power quality upon the efficiency of electric power consumption. *2019 IEEE 2nd Ukraine Conference on Electrical and Computer Engineering (UKRCON)*, 2019, pp. 556-561. doi: https://doi.org/10.1109/ukrcon.2019.8879841.

3. Toader C., Postolache P., Golovanov N., Porumb R., Mircea I., Mircea P. Power quality impact of energy-efficient electric domestic appliances. *2014 International Conference on Applied and Theoretical Electricity (ICATE)*, 2014, pp. 1-8. doi: https://doi.org/10.1109/icate.2014.6972627.

4. Montano J.-C., Salmeron P., Thomas J.P. Analysis of power losses for instantaneous compensation of three-phase four-wire systems. *IEEE Transactions on Power Electronics*, 2005, vol. 20, no. 4, pp. 901-907. doi: https://doi.org/10.1109/TPEL.2005.850956.

5. Rajalakshmi R., Rajasekaran V. Improvement of energy efficiency through power quality by the compensation of harmonics with shunt active power filter. *2011 International conference on recent advancements in electrical, electronics and control engineering*, 2011, pp. 324-327. doi: https://doi.org/10.1109/ICONRAEeCE.2011.6129820.

6. Artemenko M.Y., Batrak L.M. The new formula for apparent power and power losses of three-phase four-wire system. *2017 IEEE 37th International Conference on Electronics and Nanotechnology (ELNANO)*, 2017, pp. 389-393. doi: https://doi.org/10.1109/ELNANO.2017.7939784.

7. Artemenko M.Y., Batrak L.M., Polishchuk S.Y., Mykhalskyi V.M., Shapoval I.A. The effect of load power factor on the efficiency of three-phase four-wire power system with shunt active filter. *2016 IEEE 36th International Conference on Electronics and Nanotechnology (ELNANO)*, 2016, pp. 277-282. doi: https://doi.org/10.1109/ELNANO.2016.7493067.

8. Artemenko M.Y., Batrak L.M., Domaskina N.I. Apparent power of three-phase four-wire system in sinusoidal asymmetric mode and energy effectiveness of shunt active filters. *2015*

IEEE 35th International Conference on Electronics and Nanotechnology (ELNANO), 2015, pp. 469-474. doi: https://doi.org/10.1109/ELNANO.2015.7146952.

9. Bourouis B., Djeghloud H., Benalla H. An innovative algorithm for a hybrid FC/battery system energy management. *Electrical Engineering & Electromechanics*, 2020, no. 6, pp. 35-44. doi: https://doi.org/10.20998/2074-272x.2020.6.06.

10. Bourouis B., Djeghloud H., Benalla H. Three-Level NPC Shunt Active Filter Powered by a Hybrid Fuel-Cell/Battery DC Bus Voltage. *2021 18th International Multi-Conference on Systems, Signals & Devices (SSD)*, 2021, pp. 330-339. doi: https://doi.org/10.1109/ssd52085.2021.9429308.

11. Ladoux P., Olle G. *Compensateur d'harmoniques et de puissance réactive*. RESELEC Publ., 2002. 45 p. (Fra). Available at: https://eduscol.education.fr/sti/sites/eduscol.education.fr.sti/files/ressources/techniques/3877/3877-compensateur-harmoniques.pdf (accessed 12 March 2021).

12. Available at: https://www.brusa.biz/portfolio/bdc546/?lang=en (accessed 12 March 2020).

13. Motapon S.N. *Design and simulation of a fuel cell hybrid emergency power system for a more electric aircraft: evaluation of energy management schemes*. PhD Thesis Presented to École de Technologie Supérieure, Montreal, March 2013. Available at: https://www.proquest.com/docview/1501641145 (accessed 12 March 2021).

Received 05.07.2021
Accepted 31.08.2021
Published 26.10.2021

Billel Bourouis[1]*, PhD Student,*
Hind Djeghloud[2]*, Lecturer,*
Hocine Benalla[1]*, Professor,*
[1] Laboratory of Electrotechnics of Constantine (LEC),
Mentouri Brothers University, Constantine 1,
Campus Ahmed Hamani Zerzara,
Route d'Ain el Bey, Constantine, 25000, Algeria,
e-mail: billelbourouis1@outlook.com (Corresponding author),
benalladz@yahoo.fr
[2] Laboratory of Electrical Engineering of Constantine (LGEC),
Mentouri Brothers University, Constantine 1,
Campus Ahmed Hamani Zerzara,
Route d'Ain el Bey, Constantine, 25000, Algeria.
e-mail: hinddjeghloud@yahoo.fr

How to cite this article:
Bourouis B., Djeghloud H., Benalla H. Energy efficiency of a 3-level shunt active power filter powered by a fuel cell / battery DC bus with regulated duty cycles. *Electrical Engineering & Electromechanics*, 2021, no. 5, pp. 30-38. doi: https://doi.org/10.20998/2074-272X.2021.5.05.

UDC 681.586 https://doi.org/10.20998/2074-272X.2021.5.06

A.A. Mohamad Yusoff, K.A. Ahmad, S.N. Sulaiman, Z. Hussain, N. Abdullah

AIR CAVITY-BASED VIBRATIONAL PIEZOELECTRIC ENERGY HARVESTERS

Introduction. *Known vibrational energy harvesting methods use a source of vibration to harvest electric energy. Piezoelectric material works as a sensing element converted mechanical energy (vibration) to electrical energy (electric field). The existing piezoelectric energy harvesting (PEHs) devices have low sensitivity, low energy conversion, and low bandwidth.* ***The novelty*** *of the proposed work consists of the design of PEH's structure. Air cavity was implemented in the design where it is located under the sensing membrane to improve sensitivity. Another novelty is also consisting in the design structure where the flexural membrane was located at the top of electrodes. The third novelty is a new design structure of printed circuit board (PCB). The* ***purpose*** *of improvised design is to increase the stress in between the edges of PEH and increase energy conversion. With the new structure of PCB, it will work as a substrate that absorbs surrounding vibration energy and transfers it to sensing element.* ***Methods.*** *Three techniques were successfully designed in PEH and fabricated namely PEH A, PEH B, and PEH C were characterized by two experiments: load and vibration. The load experiment measured load pressure towards the PEH, whereas the vibration experiment measured stress towards the PEH.* ***Results.*** *PEH C has the highest induced voltage for a weight of 5.2 kg at the frequency of 50 Hz and the highest stored voltage for a period of 4 min. The three techniques applied in PEHs were showed improvement in transducer sensitivity and energy conversion.* ***Practical value.*** *A piezoelectric acoustic generator was used in the experiment to compare the performance of the designed PEH with available piezoelectric transducers in the market. The new flexible membrane worked as a sensing element was worked as a cantilever beam. PVDF was used as a sensing element due to the flexibility of the polymer material, which is expected to improve sensitivity and operating bandwidth.* References 21, tables 6, figures 19.

Key words: **piezoelectric energy harvester, air cavity, flexural membrane.**

Вступ. *Відомі методи збору вібраційної енергії використовують джерело вібрації для збору електричної енергії. П'єзоелектричний матеріал працює як чутливий елемент, перетворюючи механічну енергію (вібрацію) в електричну енергію (електричне поле). Існуючі пристрої збору п'єзоелектричної енергії (ЗПЕ) мають низьку чутливість, низьке перетворення енергії і малу смугу пропускання.* ***Новизна*** *запропонованої роботи полягає в проектуванні конструкції ЗПЕ. У конструкції реалізована повітряна порожнина, яка розташована під чутливої мембраною для підвищення чутливості. Ще один елемент новизни полягає в конструкції, в якій вигиниста мембрана розташована у верхній частині електродів. Третя новизна - це нова конструкція друкованої плати.* ***Мета*** *запропонованої конструкції - збільшити механічну напругу між краями ЗПЕ і підвищити перетворення енергії. Завдяки новій конструкції друкованої плати вона буде працювати як підкладка, яка поглинає навколишню енергію вібрації і передає її на чутливий елемент.* ***Методи***. *Три методи були успішно використані для проектування ЗПЕ, і відповідно названі виготовлені ЗПЕ А, ЗПЕ Б і ЗПЕ В були описані двома експериментальними характеристиками: навантаження і вібрація. В експерименті з навантаженням вимірювався тиск навантаження на ЗПЕ, в той час як в експерименті з вібрацією вимірювалася механічна напруга на ЗПЕ.* ***Результати***. *ЗПЕ В має найвищу індуковану напругу для ваги 5,2 кг при частоті 50 Гц і найвищу збережену напругу протягом 4 хвилин. Три методи, що застосовуються для ЗПЕ, показали поліпшення чутливості перетворювача і перетворення енергії.* ***Практична цінність***. *В експерименті використовувався п'єзоелектричний акустичний генератор для порівняння характеристик розробленого ЗПЕ з доступними на ринку п'єзоелектричними перетворювачами. Нова гнучка мембрана працювала як чутливий елемент, що представляв собою консольну балка. В якості чутливого елемента використовувався полівініліден фторид завдяки гнучкості полімерного матеріалу, який, як очікується, поліпшить чутливість і робочу смугу пропускання.* Бібл. 21, табл. 6, рис. 19.

Ключові слова: **збирач п'єзоелектричної енергії, повітряна порожнина, вигиниста мембрана.**

Introduction. Energy harvesting is a process to collect and store energy from energy sources, such as wind [1], solar [2], thermal [3], vibration [4], and biomechanical [5] sources. The facilities for harvesting wind, solar, and thermal energy are designed in huge sizes and generate high energy, whereas the components for harvesting vibration and biomechanical energy are designed in small sizes and sometimes generate energy in microvolts only. Vibration is an energy source that can be harvest at any place. Among the examples are vibration energy created by bridges [6], machines [7, 8], compressors [9], airport walkways [10] and railway tracks [11]. These vibrational energy sources are wasted if not harvested. Two methods that can harvest vibration energy are electromagnetic energy harvesters (EEHs) [9, 10] and piezoelectric energy harvesters (PEHs) [10, 11]. The basic components of an EEH consist of a spring, a coil, and a permanent magnet.

A vibrational force is applied to the spring to make it swing and the permanent magnet moves through the coil. An induced voltage is generated by the coil during the movement of the permanent magnet through the coil [12]. Some design has used a ring to replace the spring to make the permanent magnet move freely [13]. However, these designs suffer from the limitation of ageing, such as a spring loses its stiffness with time and a permanent magnet also loses its magnetization with time. Hence, PEHs are used to solve these problems [14]. A PEH consists of a piezoelectric material, a cantilever beam, and a proof mass. The piezoelectric material is a sensing element to convert mechanical energy to electrical energy. It was attached together with cantilever beam which is worked as a swinging component. Proof mass was placed at the end of the cantilever worked as a load that makes the cantilever beam swing after a vibration force is acted to the cantilever. When the cantilever beam swings, it causes stress inside the sensing material; subsequently, an induced voltage is generated.

PEH consists of the cantilever beam and the proof mass was free at the end and mounted beneath its base, which is known as base-mounted piezoelectric (BMP)

harvesters. A BMP harvester with a 0.267 mm thick layer of PZT5H was attached to a polymer beam (1.6 mm × 4.9 mm × 20.0 mm) and a steel tip mass. The peak voltages increased to 6.20, 15.1, 29.2, and 54.3 V with resonant frequencies of 45 Hz at 0.25 g to 44 Hz at 1 g. Shorter beams were preferred in the design to improve electromechanical coupling and generate more induced voltage [15]. A cantilever beam consisted of a sensing element called piezoelectric bimorph and an electrode called copper with the dimension of 79 mm × 1.55 mm (length × thickness) and attached to the proof mass with the dimension of 20 mm × 4 mm (length × thickness). This device generated an induced voltage of 37 V and output power at 145 Hz. It was installed under a smart road system [16]. For a low mechanical damping ratio, a vacuum package energy harvester (VPH) was designed to cater the problem of 50 % power drop, corresponding to 2 % deviation of frequency. The VPH was similar to the design previously which was consisted of a piezoelectric bimorph with the dimension of 28.6 × 12.7 × 0.508 mm^3 and stiffness of K = 760 N/m. The VPH generated output power of 90.3 μW at the frequency of 50 Hz [17].

A multi-degree of freedom vibration system has been added in the design of PEHs to improve the wideband performance. This design offers high power density and increases the generated induced voltage. Three proof masses were located at the centre, top left, and bottom right. Then, the cantilevers were attached to the mass centre, top left mass, and bottom right mass. The bandwidths were increased to 5.3, 9.8, 14, and 16 Hz for the acceleration of 0.2, 0.5, 0.7, and 1 m/s^2, respectively. The average power harvested by the PEHs were 0.34–2.80 μW [18]. Two parallel beam structures were designed to improve the operating bandwidth of PEH. Each beam consisted of a top electrode and a bottom electrode, then a zinc oxide (ZnO) was a sensing element with a thickness of 2.73 μm sandwiched between the electrodes. This PEH generated an induced voltage of 18 V at the frequency of 142 Hz with a bandwidth of 15 Hz [19]. A cantilever beam was sandwiched with two sensing element and one end of the cantilever beam was installed with a tip mass, whereas the other end was nailed to the wall. The PEHs generated an average power of 25 μW at the frequency range of 33–35 Hz [20]. This type of design can be applied for slow swinging movement.

The goal of the paper is to design a new flexible membrane worked as sensing element called piezoelectric polymers, polyvinylidene fluoride (PVDF) were attached together with a printed circuit board (PCB) and it was worked as a cantilever beam. PVDF was used as a sensing element due to the flexibility of the polymer material, which is expected to improve sensitivity and operating bandwidth. A PEH with good sensitivity can generate a high induced voltage. A new technique of substrate, PCB was used to absorb impact of surrounding vibration and transfer it to flexible sensing element which to improve sensitivity and bandwidth.

Subject of investigations. The PEH design focused on the design of the electrode circuit. Figure 1 shows the interdigitated electrode (IDE) circuit designed on a PCB. The IDE circuit consists of the IDE finger, the IDE path, and a terminal pad. The IDE finger used generated an induced voltage together with the sensing element, PVDF. Then, the IDE path lays the current to the terminal pad.

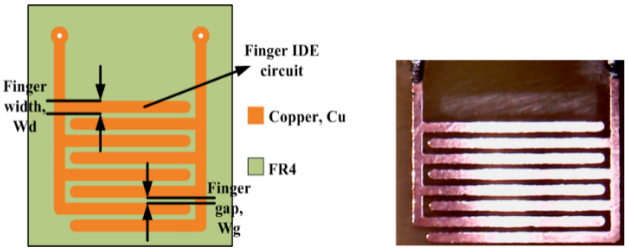

a *b*

Fig. 1. IDE design circuit on a PCB: (*a*) schematic diagram and (*b*) digital microscope image of the IDE circuit on a PCB

Three different electrode finger widths were fabricated and the width of electrode fingers were 0.5, 1, and 2 mm. The gap between the electrode fingers for all designs was fixed to 0.5 mm and the number of electrode finger pairs was 4. Three fabricated designs were namely PEH A, PEH B, and PEH C. They are shown in Table 1.

Table 1

Parameters of the IDE circuit for PEH A, PEH B, and PEH C

PEH design	Finger width, W_d, mm	Finger gap, W_g, mm	Area of PVDF, mm^2
A	0.5	0.5	142.5
B	1		218.5
C	2		370.5

The IDE design constructed using Proteus software is shown in Fig. 2.

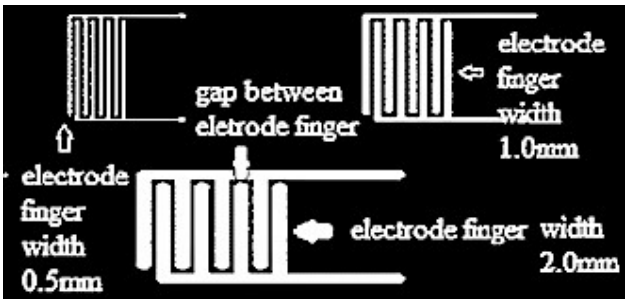

Fig. 2. IDE circuit design constructed using Proteus

***D_{33}* mode piezoelectric energy harvester.** The new design structure of PEH using the method of d_{33} mode piezoelectric material was implemented in the design. The first number of d_{33} mode indicates the voltage generated at z-axis and the second number indicates the force applied to the piezoelectric material that causes stress inside the piezoelectric material. A new design structure applied in PEH was the flexible sensing element placed at the top IDE electrode. The substrate of PEH was PCB used to absorb surrounding vibration energy and transfer to flexible sensing element, thus the sensing element got stress and converted to electric field. D_{33} component inside sensing element was converted two times energy compared to d_{31} mode.

Two new techniques approach, (1) flexible sensing element on top of electrode, and (2) substrate made of PCB were improved energy conversion and sensitivity. The operation of d_{33} mode piezoelectric material on the PEH is shown in Fig. 3.

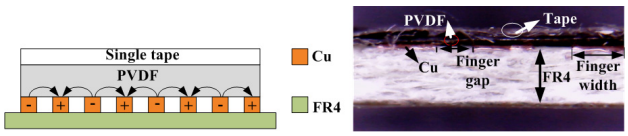

a *b*

Fig. 3. D_{33} mode piezoelectric energy harvester: (*a*) schematic diagram and (*b*) cross-sectional digital microscope image of the PEH

The operation of d_{33} mode polarization is that when stress occurs between the electrodes in three directions, polarization is also created between the electrodes in three directions. The electron *e* moves from low potential (negative terminal) to high potential (positive terminal) and the movement of electrons induces voltage, as shown in Fig. 3,*a*. Figure 3,*b* illustrates the cross-section of the PEH, where the top of the PEH is a single tape, followed by PVDF, a row of copper and air space, and lastly the FR4. The new design structure of backing layer called air cavity was placed under sensing element and in between of finger electrodes. When the cantilever beam moves up and down, more stress occurs at the sensing element at cavity side and generated more induced voltage, as illustrated in Fig. 4.

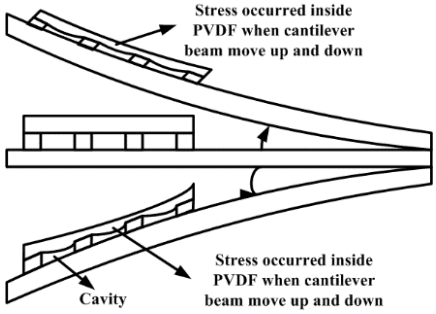

Fig. 4. Schematic diagram of stress occurring inside PVDF during the movement of the cantilever beam

Development of readout circuitry. The induced AC voltage accumulates at the terminal of PEH, and then the readout circuitry is rectified, filtered, and stored the DC voltage in a capacitor. Figure 5 shows the schematic diagram of the parallel synchronized switching harvesting inductor circuit (SSHI) readout circuit introduced by [21], which consisted of the PEH, a switch (S), an inductor (L) of 22 μH, bridge diodes (D1 – D4) of Schottky type, a capacitor (C) of 12 nF, and resistor of 600 kΩ. The maximum working voltage for the capacitor is 35 V. A multimeter was used to measure the output DC voltage at $V_c(t)$. Diodes D1 to D4 worked as full-wave rectifiers to rectify all AC to DC.

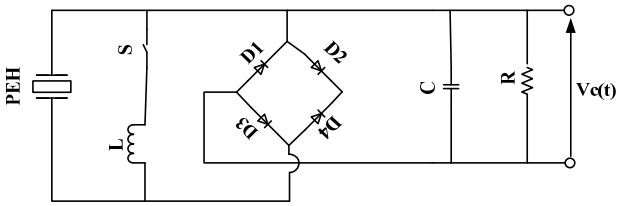

Fig. 5. Schematic diagram of a parallel SSHI readout circuit for energy harvesting

Fabrication. The overview of the fabrication process is shown in Fig. 6.

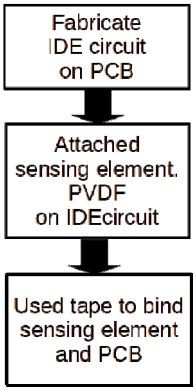

Fig. 6. Flowchart of the fabrication process

The steps presented in Fig. 6 were the flow of PEH fabrication. First, the IDE circuit was fabricated on a PCB, as shown in Fig. 7. Next, a PCB was cleaned using a brushing machine. The final step of the fabrication process was attaching PVDF on top of the fabricated IDE circuit using 3M single tape. The terminal pad was soldered with two wires and the completed fabricated PEH is shown in Fig 8.

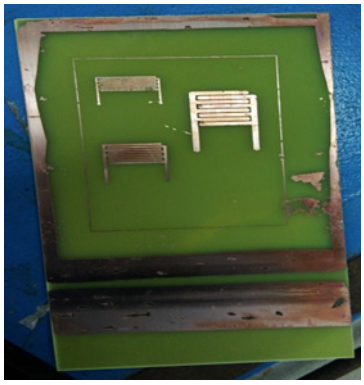

Fig. 7. Fabricated IDE circuits

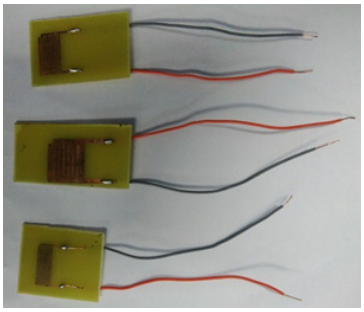

Fig. 8. Fabricated piezoelectric energy harvesters

Experimental setup. The PEH was characterized using load and vibration experiments. The load experiment measured load pressure towards the PEH, whereas the vibration experiment measured stress towards the PEH. A piezoelectric acoustic generator was used in the experiment to compare the performance of the designed PEH with available piezoelectric transducers in the market. The parameters of the piezoelectric acoustic generator are listed in Table 2.

Table 2

Diameter and area of the piezoelectric acoustic generator

Parameter	Value
Diameter of piezo ceramic, mm	20
Area of piezo ceramic, mm^2	314.16

Figure 9 presents the piezoelectric acoustic generator. The diameter of the piezoelectric ceramic was 20 mm, which was sandwiched between two copper layers.

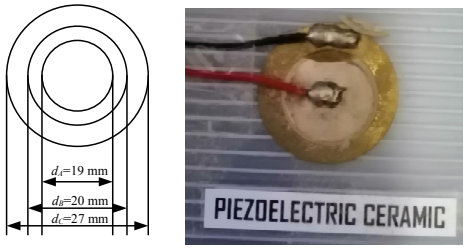

a *b*

Fig. 9. Illustration of a piezoelectric acoustic generator: (*a*) schematic diagram and (*b*) camera image

Load experiment. The experiment was carried out by obtaining the output from different mass ranges of 200 g to 5.2 kg with a step of 1 kg placed on top of the PEH. The study investigated the induced voltage for different weights and designs of PEHs. The equation for pressure P in load experiment is:

$$P = f/A, \quad (1)$$

where f is the gravitational force; and A is the area of PVDF surface.

The equation of gravitational force is:

$$f = m \cdot g, \quad (2)$$

where m is the mass; g is the gravity acceleration (9.81 m/s^2).

Six different weights were used: 200 g, 1.2 kg, 2.2 kg, 3.2 kg, 4.2 kg, and 5.2 kg. The load experiment is shown in Fig. 10. Figure 10,*a* shows the schematic diagram of the load experiment setup; Fig. 10,*b* shows the use of 200 g and 1 kg loads. Meanwhile, Fig. 10,*c* shows the DC voltage measurement setup using a digital multimeter and an energy harvester circuit.

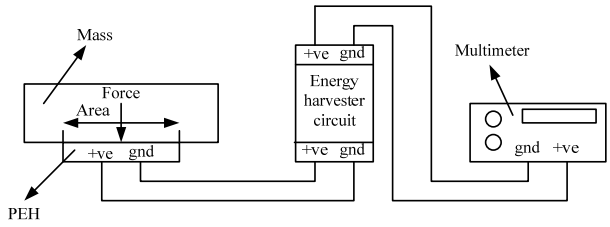

a

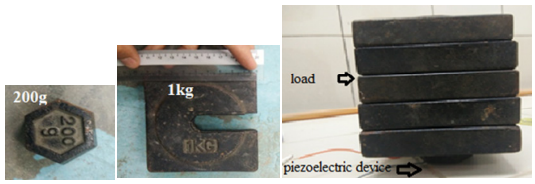

b

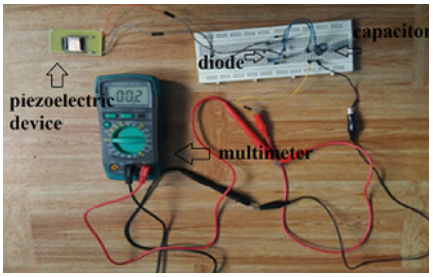

c

Fig. 10. Load experiment setup: (*a*) schematic diagram; (*b*) 200 g and 1 kg loads; (*c*) DC voltage measurement setup at the output of the energy harvester circuit using a digital multimeter

For load experiment, the loads were placed on the PEH and the output of the PEH was rectified and stored in a capacitor using an energy harvester circuit. The output of the energy harvester circuit was measured using a digital multimeter. For every measurement of load, three readings were recorded and the average reading for each load was recorded in a table.

Vibration experiment. The experiment was carried out by placing the PEH on a vibration machine. This experiment investigated the induced voltage generated by the PEH during vibration. A sieve shaker was used as a vibrator machine at 50 Hz and the AC voltage of the PEH output was measured using an oscilloscope. The vibration experiment setup is presented in Fig. 11.

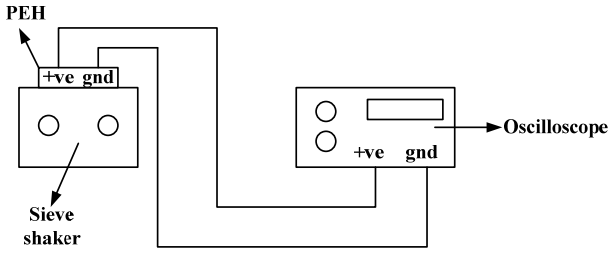

a

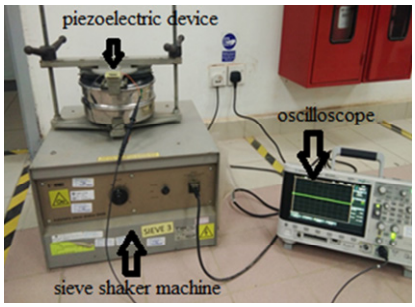

b

Fig. 11. Vibration experiment setup: (*a*) schematic diagram and (*b*) digital image of vibration experiment setup

Three different designs of PEHs were investigated in this experiment. A sieve shaker was set at 4 min of vibration and the generated AC output voltage of the PEH was recorded every minute. Two parts of measurement were conducted in this experiment, namely the measurement of the generated voltage versus input frequency and the measurement of the generated voltage for a period of time. The input frequency was set to 50 Hz because almost all vibration equipment in Malaysia used 50 Hz as an input of the machine.

Results and discussion. This section is divided into two parts, which are induced DC output voltage from load experiment and induced AC output voltage from vibration experiment. Both parts are discussed in terms of the performance of output voltage produced by the PEH.

DC output voltage from load experiment. The DC output voltage for all PEH designs (PEH A, PEH B, and PEH C) with different mass ranges of 0.2 g to 5.2 kg was measured and the mean values of the recorded voltage are shown in Table 3, 4, 5, respectively. Each table presents the weight, mean output voltage, and standard error for the particular design. The mean output voltage was calculated from three readings of the same weight measurement and divided by the number of readings. For this experiment, three readings were taken for calculating the mean output

value and the standard error was a standard deviation of the mean value. The pressure was calculated from the input weight and area of PVDF.

Table 3

Results for PEH A

Weight, kg	Mean output, voltage, mV	Standard error, %	Pressure, f/A, N/m^2
0.2	0.202	5	1401.43
1.2	0.402	6	8408.57
2.2	0.607	3	15415.71
3.2	0.810	4	22422.86
4.2	1.097	5	29430
5.2	1.123	3	36437.14

The standard error for all readings is acceptable because the error is less than 10 %. The highest standard error of 6 % was recorded for the load weight of 1.2 kg. The mean induced voltage increased proportionally with the input pressure given by load weight. Figure 12 shows that at the pressure of 29430 to 36437.14 N/m^2, the mean output voltage was saturated at 1.123 mV. The mean output from 0.202 to 1.097 mV was proportional with the increase of pressure from 1400 to 29430 N/m^2, respectively.

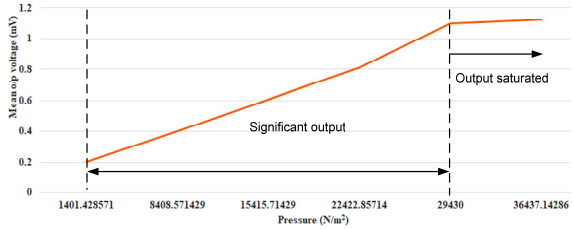

Fig. 12. Plot of mean output value versus pressure for PEH A

The results for PEH B are tabulated in Table 4. The readings are also acceptable because the standard error is less than 10 %. The input pressure started at a lower value of 897.94 N/m^2 compared to PEH A of 1401.429 N/m^2 and until the final load of PEH B, the input pressure was less than the final load of PEH A.

Table 4

Results for PEH B

Weight, kg	Mean output, voltage, mV	Standard error, %	Pressure, f/A, N/m^2
0.2	0.306	2	897.94
1.2	0.904	3	5387.64
2.2	1.103	3	9877.35
3.2	1.303	5	14367.05
4.2	2.004	4	18856.75
5.2	2.301	5	23346.45

Figure 13 shows a significant output voltage because the mean output voltage from the range of 0.306 to 2.301 mV increased proportionally with the input pressure from 897.94 to 23346.45 N/m^2. The mean output voltage of PEH B was higher than PEH A for the low pressure input. It is shown that PEH B is more sensitive and generated more induced voltage than PEH A.

Table 5 shows the tabulated results for PEH C. The mean output voltage was generated in the range of 0.7 to 2.5 mV for the pressure range of 529 to 13768 N/m^2. The standard error shows that the readings are in the acceptable range for PEH C.

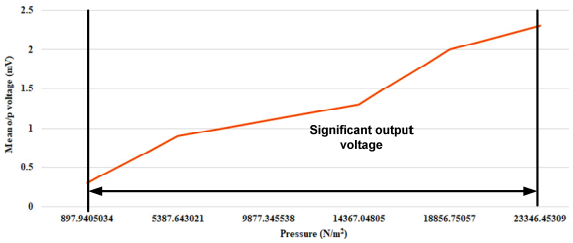

Fig. 13. Plot of mean output voltage versus pressure for PEH B

Table 5

Results for PEH C

Weight, kg	Mean output, voltage, mV	Standard error, %	Pressure, f/A, N/m^2
0.2	0.702	3	529.55
1.2	0.903	4	3177.33
2.2	1.199	3	5825.10
3.2	1.504	3	8427.87
4.2	1.901	5	11120.65
5.2	2.502	5	13768.42

Figure 14 shows that PEH C is more sensitive compared to PEH B and PEH A. The low pressure input generated high induced voltage. PEH C has the widest IDE electrode finger width, followed by PEH B and PEH A. Furthermore, the highest generated induced voltage was obtained by PEH C, followed by PEH B and PEH A. Therefore, the width of finger electrodes improved the generated induced voltage and sensitivity of PEH.

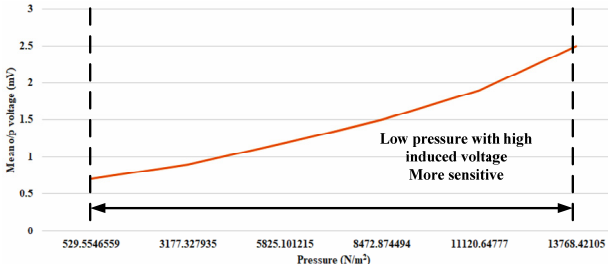

Fig. 14. Plot of mean output voltage versus pressure for PEH C

Table 6 tabulates the results for the commercial piezoelectric acoustic generator. The mean output voltage generated by the piezoelectric acoustic generator was in the range of 0.124 to 0.365 mV for the range of input pressure input of 6248 N/m^2 to 162458.6 N/m^2.

Table 6

Results for piezoelectric acoustic generator

Weight, kg	Mean output, voltage, mV	Standard error, %	Pressure, f/A, N/m^2
0.2	0.124	3	6248.41
1.2	0.185	2	37490.45
2.2	0.191	2	68732.48
3.2	0.212	2	99974.52
4.2	0.255	3	131216.60
5.2	0.365	3	162458.60

Figure 15 shows the mean output voltage for the piezoelectric acoustic generator. The generator has low sensitivity due to the low generated induced voltage as high pressure input was introduced to the acoustic generator. All PEH designs have high sensitivity compared to the piezoelectric acoustic generator. The IDE design shows good performance compared to a simple sandwiched piezoelectric acoustic generator. Although the

area of the electrode of the piezoelectric acoustic generator is larger than the area for PEH A, this design has more induced voltage compared to the piezoelectric acoustic generator.

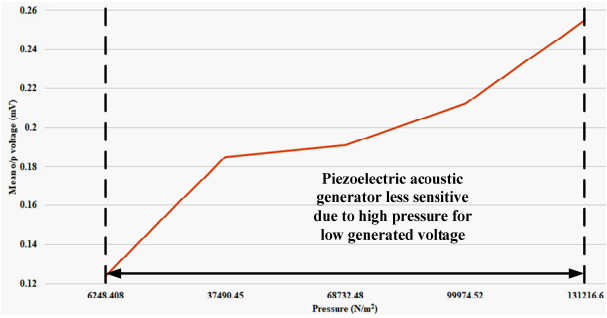

Fig. 15. Plot of mean output voltage versus pressure for piezoelectric acoustic generator

Output voltage from vibration experiment. For vibration experiment, two parts of the results were obtained. Part B.1 shows the results of the generated output voltage versus input frequency of 50 Hz and part B.2 shows the results of the generated voltage for the given period.

Output voltage versus input frequency. Figure 16 shows the generated output voltage versus the input frequency of 50 Hz for PEH A. The generated output voltage generated fluctuated from 0.23 to 0.28 mV.

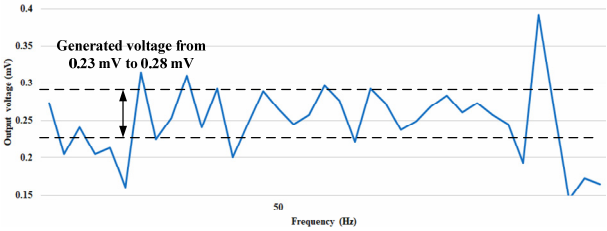

Fig 16. Generated output voltage versus input frequency for PEH A

Figure 17 shows the generated output voltage versus the input frequency of 50 Hz for PEH B. The generated output voltage fluctuated from 0.25 to 0.52 mV for the input frequency of 50 Hz. The generated voltage of PEH B consists of two parts: 0.25 to 0.30 mV and 0.45 to 0.50 mV.

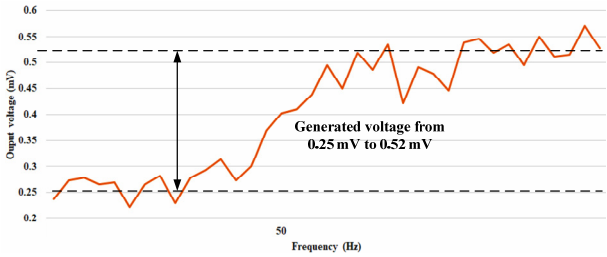

Fig 17. Generated output voltage versus input frequency for PEH B

Figure 18 shows the generated output voltage for PEH C for the given input frequency of 50 Hz. The pattern of PEH C output is almost similar to the pattern of PEH B output, where the generated output of PEH C oscillated from 0.28 to 0.55 mV. The generated voltage of PEH C also consists of two parts: 0.28 to 0.30 mV and 0.50 to 0.55 mV.

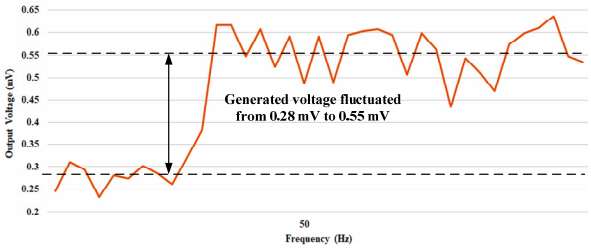

Fig. 18. Generated output voltage versus input frequency for PEH C

All three plotted graphs show that the generated output of load weight is higher compared to vibration. In this experiment, PEH C has higher generated voltage than PEH B and PEH A, where PEH C recorded the generated voltage of 0.55 mV.

Output voltage versus period of time. The results of generated voltage for the period of time are shown in Fig. 19. The generated voltage for all design of PEHs increased significantly at 3 to 4 min. The highest energy stored in the capacitor was generated by PEH C with 34560 mV.

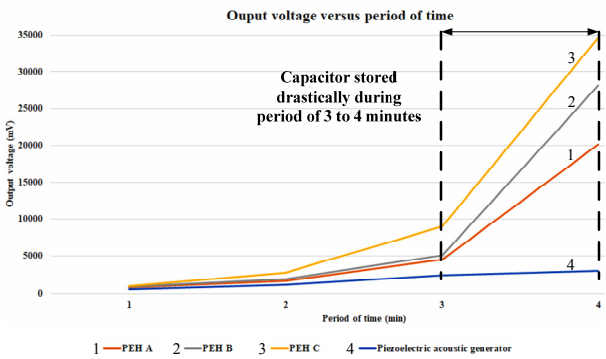

Fig. 19. Generated voltage stored versus period of time

Conclusions.

1. A new design structure of PEH using flexible sensing element, PVDF and PCB substrate with IDE circuits were successfully design, fabricated and characterized in this project. Three PEHs with different IDE circuit width were fabricated together with a PVDF sheet and single transparent tape.

2. All designs namely PEH A, PEH B, and PEH C were successfully characterized by two experiments namely load and vibration experiments. PEH C generated the highest voltage in load experiment of 2.502 mV for the weight of 5.2 kg. In vibration experiment, PEH C generated the highest voltage of 0.55 mV for the input frequency of 50 Hz. PEH C also stored the highest voltage of 34560 mV for the time period of 4 min.

3. PEH C is the best design of an energy harvester if applied for a vibration machine of 50 Hz or from footsteps in the walking area of an airport. For future recommendations, this device can be installed in the walking area of an airport and used as a free energy source for charging a small electronic device. The device can be placed under the walking area, and then the energy is harvested and stored in a battery bank.

Conflict of interest. The authors declare that they have no conflicts of interest.

REFERENCES

1. Zhao L., Tang L., Liang J., Yang Y. Synergy of wind energy harvesting and synchronized switch harvesting interface circuit. *IEEE/ASME Transactions on Mechatronics*, 2017, vol. 22, no. 2, pp. 1093-1103. doi: https://doi.org/10.1109/tmech.2016.2630732.

2. Shekhar A., Kumaravel V.K., Klerks S., De Wit S., Venugopal P., Narayan N., Bauer P., Isabella O., Zeman M. Harvesting roadway solar energy – performance of the installed infrastructure integrated PV bike path. *IEEE Journal of Photovoltaics*, 2018, vol. 8, no. 4, pp. 1066-1073. doi: https://doi.org/10.1109/jphotov.2018.2820998.

3. Camboim M.M., Oliveira V.S., Villarim M.R., Villarim A.W.R., Catunda S.Y.C., Baiocchi O.R., De Souza C.P. An online remote verification system of thermal sources for energy harvesting application. *IEEE Transactions on Instrumentation and Measurement*, 2020, vol. 69, no. 10, pp. 7962-7973. doi: https://doi.org/10.1109/tim.2020.2986105.

4. He W., Zhang J., Yuan S., Yang A., Qu C. A three-dimensional magneto-electric vibration energy harvester based on magnetic levitation. *IEEE Magnetics Letters*, 2017, vol. 8, pp. 1-3, art no. 6104703. doi: https://doi.org/10.1109/lmag.2017.2669300.

5. Todaro M.T., Guido F., Algieri L., Mastronardi V.M., Desmaele D., Epifani G., De Vittorio M. Biocompatible, flexible, and compliant energy harvesters based on piezoelectric thin films. *IEEE Transactions on Nanotechnology*, 2018, vol. 17, no. 2, pp. 220-230. doi: https://doi.org/10.1109/TNANO.2017.2789300.

6. Khan F.U., Iqbal M. Electromagnetic bridge energy harvester utilizing bridge's vibrations and ambient wind for wireless sensor node application. *Journal of Sensors*, 2018, vol. 2018, art. no. 3849683. doi: https://doi.org/10.1155/2018/3849683.

7. Chaudhuri D., Kundu S. MEMS piezoelectric energy harvester to power wireless sensor nodes for machine monitoring application. *2017 Devices for Integrated Circuit (DevIC)*, 2017, pp. 584-588. doi: https://doi.org/10.1109/devic.2017.8074018.

8. Shin A., Radhakrishna U., Yang Y., Zhang Q., Gu L., Riehl P., Chandrakasan A.P., Lang J.H. A MEMS magnetic-based vibration energy harvester. *Journal of Physics: Conference Series*, 2018, vol. 1052, p. 012082. doi: https://doi.org/10.1088/1742-6596/1052/1/012082.

9. Rodriguez J.C., Nico V., Punch J. A vibration energy harvester and power management solution for battery-free operation of wireless sensor nodes. *Sensors*, 2019, vol. 19, no. 17, p. 3776. doi: https://doi.org/10.3390/s19173776.

10. Correia D., Ferreira A. Energy harvesting on airport pavements: state-of-the-art. *Sustainability*, 2021, vol. 13, no. 11, p. 5893. doi: https://doi.org/10.3390/su13115893.

11. Hosseinkhani A., Younesian D., Eghbali P., Moayedizadeh A., Fassih A. Sound and vibration energy harvesting for railway applications: A review on linear and nonlinear techniques. *Energy Reports*, 2021, vol. 7, pp. 852-874. doi: https://doi.org/10.1016/j.egyr.2021.01.087.

12. Lee H., Noh M.D., Park Y. Optimal Design of Electromagnetic Energy Harvester Using Analytic Equations. *IEEE Transactions on Magnetics*, 2017, vol. 53, no. 11, pp. 1-5, art no. 8207605. doi: https://doi.org/10.1109/TMAG.2017.2708130.

13. Cai M., Liao W.-H. Design, modeling, and experiments of electromagnetic energy harvester embedded in smart watch and wristband as power source. *IEEE/ASME Transactions on Mechatronics*, 2021, vol. 26, no. 4, pp. 2104-2114. doi: https://doi.org/10.1109/tmech.2020.3032536.

14. Nabavi S., Zhang L. Nonlinear multi-mode wideband piezoelectric MEMS vibration energy harvester. *IEEE Sensors Journal*, 2019, vol. 19, no. 13, pp. 4837-4848. doi: https://doi.org/10.1109/jsen.2019.2904025.

15. Koven R., Mills M., Gale R., Aksak B. Low-frequency and broadband vibration energy harvesting using base-mounted piezoelectric transducers. *IEEE Transactions on Ultrasonics, Ferroelectrics, and Frequency Control*, 2017, vol. 64, no. 11, pp. 1735-1743. doi: https://doi.org/10.1109/TUFFC.2017.2739745.

16. Subbaramaiah R., Al-Jufout S.A., Ahmed A., Mozumdar M.M. Design of vibration-sourced piezoelectric harvester for battery-powered smart road sensor systems. *IEEE Sensors Journal*, 2020, vol. 20, no. 23, pp. 13940-13949. doi: https://doi.org/10.1109/JSEN.2020.3000489.

17. Abasian A., Tabesh A., Rezaei-Hosseinabadi N., Nezhad A.Z., Bongiorno M., Khajehoddin S.A. Vacuum-packaged piezoelectric energy harvester for powering smart grid monitoring devices. *IEEE Transactions on Industrial Electronics*, 2019, vol. 66, no. 6, pp. 4447-4456. doi: https://doi.org/10.1109/TIE.2018.2860557.

18. Nabavi S., Zhang L. Nonlinear multi-mode wideband piezoelectric MEMS vibration energy harvester. *IEEE Sensors Journal*, 2019, vol. 19, no. 13, pp. 4837-4848. doi: https://doi.org/10.1109/JSEN.2019.2904025.

19. Naval S., Sinha P.K., Das N.K., Anand A., Kundu S. Bandwidth increment of piezoelectric energy harvester using multi-beam structure. *2019 Devices for Integrated Circuit (DevIC)*, 2019, pp. 370-373. doi: https://doi.org/10.1109/devic.2019.8783724.

20. Rubes O., Hadas Z. Design and simulation of bistable piezoceramic cantilever for energy harvesting from slow swinging movement. *2018 IEEE 18th International Power Electronics and Motion Control Conference (PEMC)*, 2018, pp. 663-668. doi: https://doi.org/10.1109/EPEPEMC.2018.8521846.

21. Lu S., Boussaid F., Law M. Efficient parallel-SSHI interface circuit for piezoelectric energy harvesting. *2013 IEEE 11th International New Circuits and Systems Conference (NEWCAS)*, 2013, pp. 1-4. doi: https://doi.org/10.1109/NEWCAS.2013.6573658.

Received 15.08.2021
Accepted 21.09.2021
Published 26.10.2021

Ahmad Azrul Mohamad Yusoff[1], *MS,*
Khairul Azman Ahmad[1], *Senior Lecturer,*
Siti Noraini Sulaiman[1], *Associate Professor,*
Zakaria Hussain[1], *Associate Professor,*
Noramalina Abdullah[2], *Senior Lecturer,*

[1] School of Electrical Engineering, College of Engineering,
Universiti Teknologi MARA,
Cawangan Pulau Pinang, Permatang Pauh,
13500 Pulau Pinang, Malaysia
e-mail: bnc_azrol@yahoo.com.my,
azman062@uitm.edu.my,
sitinoraini@uitm.edu.my,
zakaria183@uitm.edu.my,
[2] School of Electric and Electronic Engineering,
Engineering Campus, Universiti Sains Malaysia,
14300, Nibong Tebal, Pulau Pinang, Malaysia
e-mail: eenora@usm.my (Corresponding author)

How to cite this article:
Mohamad Yusoff A.A., Ahmad K.A., Sulaiman S.N., Hussain Z., Abdullah N. Air cavity-based vibrational piezoelectric energy harvesters. *Electrical Engineering & Electromechanics*, 2021, no. 5, pp. 39-45. doi: https://doi.org/10.20998/2074-272X.2021.5.06.

UDC 621.315.615.2 https://doi.org/10.20998/2074-272X.2021.5.07

O. Shutenko, S. Ponomarenko

ANALYSIS OF DISTRIBUTION LAWS OF TRANSFORMER OIL INDICATORS IN 110-330 kV TRANSFORMERS

Introduction. *Ensuring the operational reliability of power transformers is an urgent task for the power industry in Ukraine and for most foreign countries. One of the ways to solve this problem is the correction of maximum permissible values of insulation parameters. However, such a correction is fundamentally impossible without an analysis of the laws of distribution of diagnostic indicators in the equipment with different states.* ***The purpose of the research*** *is to analyse the laws of distribution of the quality indicators of transformer oil with different states in 110 and 330 kV transformers.* ***Novelty***. *It was found that both 330 kV autotransformers and 110 kV transformers have the displacements between the mathematical expectations of the distribution density of usable oil indicators. It caused by different service life of the analysed transformers and different values of load factors. This indicates the need to consider the influence of these factors when correcting the maximum permissible values of oil indicators. Also, the presence of displacement between the distribution densities of some indicators of usable oil in 110 kV transformers and 330 kV autotransformers has been revealed. It indicates a different intensity of oxidation reactions in transformers with different voltage class. In order to reduce the heterogeneity of initial data the procedure of statistical processing of in-service test results has been proposed as a* ***method***. *This procedure combines the use of a priori information about the service life of equipment and values of load factors with the elements of statistical hypothesis testing. The* ***results*** *of the analysis of the distribution laws of transformer oil indicators with different states have shown that for both usable and unusable oil the values of oil indicators obey the Weibull distribution. Values of the shape and scale parameters for each of the obtained indices arrays have been obtained, as well as calculated and critical values of the goodness-of-fit criteria.* ***Practical value***. *Obtained values of the distribution law parameters of the transformer oil indicators with different states, considering the service life and operating conditions allow to perform the correction of the maximum permissible values of the indicators using the statistical decision-making methods.* References 38, tables 7, figures 5.

Key words: **transformer oil, oil indicators, operating time, statistical analysis, distribution laws, goodness-of-fit criteria, Weibull distribution, density functions.**

У статті наведено результати аналізу законів розподілу показників трансформаторних масел у трансформаторах 110 і 330 кВ. Встановлено, що розподіл показників для масла як придатного, так і непридатного до експлуатації, незалежно від класу напруги трансформаторів підпорядковуються закону розподілу Вейбула. Виконаний аналіз показав, що і в автотрансформаторах напругою 330 кВ, і в трансформаторах напругою 110 кВ має місце зміщення між математичними очікуваннями щільності розподілу показників масел придатного до експлуатації. Наявність даного зміщення дозволяє використовувати отриманні з урахуванням умов експлуатації значення параметрів законів розподілу для оцінки відпрацьованого ресурсу масел, а також для прогнозування та планування термінів обслуговування та ремонту обладнання. Бібл. 38, табл. 7, рис. 5.

Ключові слова: **трансформаторне масло, показники масел, тривалість експлуатації, статистичний аналіз, закони розподілу, критерії згоди, розподіл Вейбула, функції щільності розподілу.**

В статье приведены результаты анализа законов распределения показателей трансформаторных масел в трансформаторах 110 и 330 кВ. Установлено, что распределение показателей как для масла годного, так и негодного к эксплуатации, вне зависимости от класса напряжения трансформаторов подчиняются закону распределения Вейбулла. Выполненный анализ показал, что и в автотрансформаторах напряжением 330 кВ, и в трансформаторах напряжением 110 кВ имеет место смещение между математическими ожиданиями плотностей распределения показателей масел годного к эксплуатации. Наличие данного смещения позволяет использовать полученные с учетом условий эксплуатации, значения параметров законов распределения для оценки отработанного ресурса масел, а также для прогнозирования и планирования сроков обслуживания и ремонта оборудования. Библ. 38, табл. 7, рис. 5.

Ключевые слова: **трансформаторное масло, показатели масел, длительность эксплуатации, статистический анализ, законы распределения, критерии согласия, распределение Вейбулла, функции плотности распределения.**

Introduction. Accidental damage of high-voltage power transformers is accompanied by significant economic damage and in some cases can have serious consequences [1]. Given the significant ageing of high-voltage power transformers in Ukraine and in most foreign countries, as well as the extremely low rate of equipment replacement that has reached the end of its life, ensuring the operational reliability of transformers is an important scientific and practical task. One of the elements of insulation of high-voltage power transformers is petroleum insulating oils. As shown in [2, 3], the condition of transformer oils has a significant role in ensuring the operational reliability of transformers. Oil oxidation products have a negative effect not only on the electrical strength of the liquid insulation, but also contribute to a reduction in the mechanical strength of the cellulose insulation, which leads to a reduction in the transformer service life. In this regard, the improvement of methods for assessing the condition of transformer oils is an urgent task. The solution of this problem will increase the operational reliability of high-voltage power transformers and extend their service life.

Publication analysis and research problem statement. At present, a great deal of research is devoted

to the improvement of methods for diagnosing the condition of transformer oils. Improvement is carried out in two main directions – the use of new methods of measurement (for example, [4-8]) and improvement of decision-making methods. For example, in [9-12] neural networks of different configurations are proposed to diagnose the condition and predict the values of transformer oil indicators. In [13, 14], oil condition assessment was performed using Markov networks. In [15, 16] fuzzy logic was applied, and in [17-19] regression models were used. Considering that under real operating conditions the condition of oils is evaluated by comparing the measured values of indicators with maximum permissible values (MPV), which are regulated by international or national standards [20, 21], in [22-24] a correction of MPV indicators of transformer oils was performed. However, in these studies, integral distribution functions were used to correct MPV, and the laws themselves were not analysed. At the same time, as shown in [25, 26], the use of statistical decision methods, taking into account the distribution laws of diagnostic indicators to correct MPV allows to significantly reduce the risks compared to the method of integral functions. In addition, the parameters of distribution laws are widely used in the development of models for predicting the residual life of equipment, e.g. [27]. Meanwhile, the analysis showed that the analysis of distribution laws of transformer oil indicators has not found sufficient coverage in the literature. An exception is the research carried out in [28] according to which oil indicators such as organic acid content (OAC), breakdown voltage (BDV), interfacial tension, oil resistivity and water content can be described by a Weibull distribution. However, the differences in the values of the oil distribution parameters obtained before filling and aged oils are insignificant, which requires further verification. Therefore, this paper presents the results of the analysis of distribution laws for the whole set of transformer oil parameters in the tanks of 110 kV transformers and 330 kV autotransformers.

Statistical processing of periodic test results. The results of periodic transformer oil BDV monitoring for the 231 transformers of 110 kV and 49 autotransformers of 330 kV were used as input data. The total volume of the analysed sample amounted to 21062 values, of which 17408 were obtained for 110 kV transformers, while 3654 were obtained for 330 kV autotransformers. The list of transformer oil indicators and the volume of sample values for each indicator are shown in Table 1.

The sample presented in Table 1 is heterogeneous both in terms of the number of transformers and of the total number of indicator values. This heterogeneity is due to several factors. For example, for such indicator as the transformer oil colour, the current Ukrainian standard [21] regulates the maximum permissible values only for new oil, and for in-service control such values are not regulated, but must be taken into account when assessing the condition of oils. This circumstance is one of the reasons that the oil colour is monitored not in all power companies in Ukraine. Insignificant amounts of sampling values for such indicators as water-soluble acids, mechanical impurities and water content are because the current standards allowed the use of several methods to determine the values of these indicators: indicative (absent or present) and quantitative (determined quantitative content of these indicators in mg KOH/g or g/t). Since the diagnosis «absent» using indicator methods is not equivalent to zero, only the results of quantitative methods were used for further analysis.

Table 1

List of indicators for transformer oils and volume of sample values for each indicator

No.	Oil quality indicator	Volume of sample values	
		Number of transformers	Number of values
110 kV transformers			
1	Flash point	230	3746
2	Acid number	231	3741
3	BDV	231	3723
4	tgδ at 20 °C	31	268
5	tgδ at 70 °C	50	426
6	tgδ at 90 °C	60	570
7	Oil colour	121	2108
8	Water-soluble acid content	46	1191
9	Water content	73	1635
330 kV autotransformers			
1	Flash point	49	887
2	Acid number	48	850
3	BDV	49	852
4	tgδ at 90 °C	45	543
5	Water content	30	400
6	Contamination content	20	122

Since the test results were obtained in different laboratories and the transformers analysed have different service lives, are operated with different loads and are filled with different oil types, it is obvious that the oil ageing intensity in the analysed transformers varies considerably. In other words, the raw data is statistically heterogeneous. As an example, Fig. 1,*a* shows the dielectric dissipation factor of transformer oils measured at 90 °C for 330 kV autotransformers. The heterogeneity of the raw data in the figure is due to both differences in the quality of the oil filled (relatively high values of tgδ measured at 90 °C at the start of operation) and differences in operating conditions (low values of this indicator were obtained with a fairly long service life). In addition, there are errors in the test results. The heterogeneity of the raw data leads to the empirical distribution histogram distortion (Fig. 1,*b*), which does not allow an evaluation of the distribution laws for transformer oils.

In this regard, there is a task of forming homogeneous arrays of transformer oil indicators. At the first stage, from the initial data set were selected values of indicators that go beyond the area of MPV, regulated by the current normative document in Ukraine [21]. Using basic terms from the theory of technical diagnostics [29], denote the data set, consisting of the results of tests for an oil usable by the values of indicators as D_1. Data set consisting of test results for unusable oil as D_2.

Two approaches are used to generate homogeneous indicator arrays. The first approach is based on the use of mathematical models of variance analysis and, as shown in [30, 31], allows obtaining sufficiently correct integral distribution functions of diagnostic attributes. A significant limitation of this approach is the limited information about the operating modes of transformers, the specifics of their design, the materials used. This may cause erroneous conclusions. The second approach is based on the use of statistical hypothesis tests and, as shown in [32], allows estimating the distribution laws of diagnostic attributes. The disadvantage of this approach is the difficulty in establishing the relationship between the parameters of the distribution laws of diagnostic indicators and the factors affecting the ageing intensity.

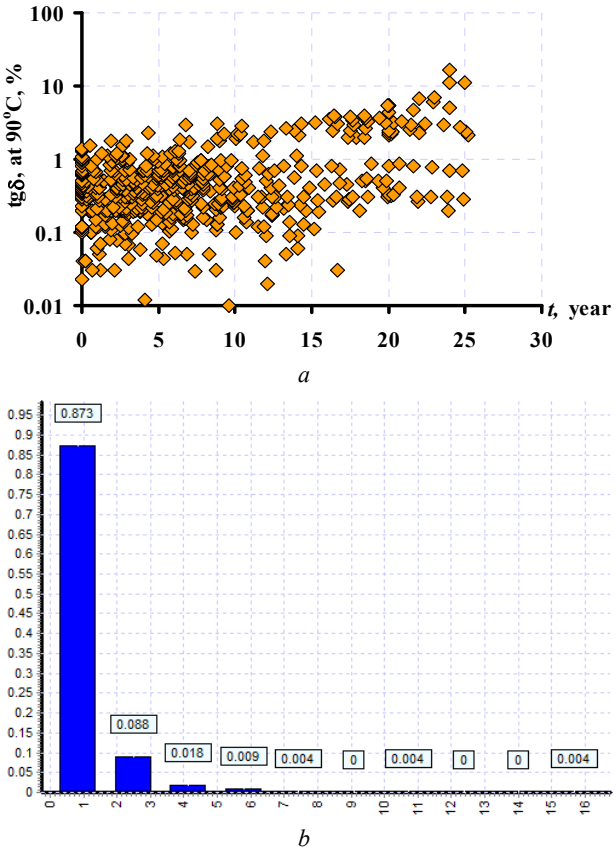

Fig. 1. Dependence of the dielectric dissipation factor of transformer oils measured at 90 °C in 330 kV autotransformers on the operating time for the original data set (*a*) and the corresponding empirical distribution histogram (*b*)

It is known [33] that the main factors influencing the intensity of oil oxidation are temperature, air oxygen content, duration of oxidation and the influence of some structural materials (copper, varnished insulating fabric, not oil resistant rubber, etc.). Considering that the date of oil filling is known for each of the transformers under consideration, the duration of oil ageing is not very difficult to account for. However, during long-term operation, the oil can be dried, regenerated, refilled or replaced both oil and silica gel, which leads to a distortion of the performance dependence on the operating time. In order to eliminate this problem, the results of the periodic tests for such transformers were divided into several groups (for example, from the time of oil filling and to the regeneration date and from the regeneration date to the date of the last test) in a preliminary statistical processing step. The insulation temperature of power transformers [34, 35] depends on both the value of load currents and the ambient temperature, as well as on the transformer cooling system. The transformers under consideration are operated in the same climatic zone with similar values of average daily temperatures, and have an identical cooling system (with oil natural and air forced for 110 kV transformers, and with oil forced and air forced for 330 kV autotransformers). Therefore, it is logical to assume that differences in oil oxidation intensity caused by different operating temperature values, which are due to differences in load currents [36]. Under conditions where transformer load information is partially available, a statistical hypothesis test approach was used to generate homogeneous arrays of indicators.

Arrays with homogeneous periodic test results were generated by using three statistical criteria [32]:

1. *Wilcoxon rank-sum test* (*W*) is used to test the statistical hypothesis of similarity of distribution laws of two independent samples:

$$W = \sum_{i=1}^{n} s(r_i), \tag{1}$$

where r_i are the ranks of the diagnostic indicators in the overall variation series; $s(r_i)$ is one of the possible $N!$ permutations of rank r_i.

2. *Z-criterion* (*Z*) is used to test the statistical hypothesis of equality of mathematical expectations of two independent samples:

$$Z_{\text{obs}} = \frac{\bar{x}_1 - \bar{x}_2}{\sqrt{\frac{\delta_1^2}{n} + \frac{\delta_2^2}{m}}}, \tag{2}$$

where $\bar{x}_1$ and $\bar{x}_2$ are the selective mean of the diagnostic indicator calculated from the first and second transformer test results respectively; δ_1^2 and δ_2^2 are the selective variance of the diagnostic indicator calculated from the first and second transformer test results respectively; n and m are the number of observations of the diagnostic indicator for the first and second transformer respectively.

3. *Fisher-Snedecor F distribution* (*F*) is used to test the statistical hypothesis of dispersions equality of two independent samples:

$$F_{\text{obs}} = \frac{\delta_{\max}^2}{\delta_{\min}^2}, \tag{3}$$

where $\delta_{\max}^2$ and $\delta_{\min}^2$ are the values of the maximum and minimum sampling variance.

Two independent samples were considered homogeneous if the following statistical hypotheses were not rejected by the test results at the given significance level $\alpha = 0.05$:

1. about similarity of distribution laws of two independent samples ($W_1 > W_{n1, n2, 0,025}$, $W_2 < W_{n1, n2, 0,975}$);

2. about equality of mathematical expectations of two independent samples ($Z_{obs}<Z_{crit,\,0,95}$);

3. about dispersions equality of two independent samples ($F_{obs}<F_{(n1-1),\,(n2-1),\,0,95}$).

The above algorithm for statistical processing of test results was implemented as the author's software «Odnorodn» [37], which significantly reduces the time required for statistical processing of raw data. Using this software in relation to the analysed data sample allowed forming several arrays of indicators with close values of sample means, sample variance and similar distribution laws. The volume of sample values (N), values of sample mean (M_x), sample variance (D_x) as well as skewness (j_s) and kurtosis (j_k) coefficients for the original data sets (D_{10}) and those obtained from statistical processing (D_{11}-D_{1n}) of usable oil indicators for 110 kV transformers are given in Table 2 and for 330 kV autotransformers in Table 3.

Comparison of statistical characteristics of initial arrays of oil indicators with similar characteristics of indicators from the arrays obtained after statistical processing showed that using statistical processing procedure allowed significantly reducing the D_x, as well as the j_s and j_k for almost all indicators. Analysis of statistical characteristics of the arrays of indicators obtained through statistical processing shows that the values of mathematical expectation of the usable oil indicators differ significantly. This indicates both different quality of transformer oil and different oil ageing intensity, that is, differences in transformer operation modes. As can be seen from Tables, negative skewness coefficients (the «long part» of the distribution curve is to the left of the mathematical expectation) are obtained mainly for the indicators which decrease in value during ageing (flash point and BDV). For the oil indicators which increase with oil ageing (organic and water-soluble acid content, tgδ, oil colour, water content, contamination content), the majority of the obtained arrays show positive skewness values («long part» of the distribution curve is to the right of the mathematical expectation).

The presence of a negative skewness for some of the indicator data sets indicates a deterioration in the condition of the transformer oil; there are more «high values» of the indicators than low ones. As can be seen from the tables, there is a positive kurtosis coefficient for all indicator arrays, indicating that the distribution curve has a higher and «sharper» peak than the curve of the normal law. The obtained empirical values of skewness and kurtosis coefficients indirectly indicate that the distribution of usable oil indicators may differ from the normal law.

The analysis showed that the homogeneous arrays were formed by testing transformers with close operating times and similar values of load factors. This made it possible to establish an unambiguous relationship between the operating conditions of the transformers and the values of the distribution law parameters.

The processing of the results of periodic tests on oils which have exceeded the MPV (unusable oil) was carried out in the following sequence. First, data sets were

Table 2

Statistical characteristics of homogeneous arrays of 110 kV transformer usable oil

Array	N	M_x	D_x	j_s	j_k
Flash point					
D_{10}	3746	143.579418	13.06904	0.809	4.281
D_{11}	284	140.059859	2.866135	–0.346	3.693
D_{12}	364	142.931319	2.030997	–0.385	4.521
D_{13}	185	144.535135	3.600117	–0.144	2.361
D_{14}	188	146.930851	15.968623	–0.088	3.404
D_{15}	280	149.089286	9.988457	–0.172	3.308
Organic acid content					
D_{10}	3339	0.034848	0.000592	0.817	2.685
D_{11}	218	0.015311	0.000087	0.587	2.472
D_{12}	198	0.027884	0.00007	0.711	3.303
D_{13}	250	0.045944	0.000395	0.175	2.262
D_{14}	129	0.046434	0.000192	–0.175	2.907
D_{15}	156	0.051679	0.000446	0.224	2.462
D_{16}	361	0.045917	0.000500	0.807	3.988
D_{17}	333	0.064655	0.001557	0.690	2.978
BDV					
D_{10}	3435	58.262667	116.058219	0.109	2.627
D_{11}	135	49.038519	44.673183	0.0748	2.423
D_{12}	609	60.654351	115.838869	–0.249	2.468
D_{13}	360	68.110833	123.619522	–0.350	2.620
D_{14}	286	69.421678	109.698341	–0.524	2.902
D_{15}	204	71.066176	124.016356	–0.657	3.038
tgδ at 20 °C					
D_{10}	268	0.182246	0.067281	7.962	83.730
D_{11}	109	0.141835	0.008986	0.793	3.075
D_{12}	141	0.188596	0.014915	0.959	3.713
tgδ at 70 °C					
D_{10}	426	0.917268	2.170500	7.513	82.291
D_{11}	112	0.290446	0.038860	0.951	3.284
D_{12}	161	0.593634	0.162197	1.051	3.892
D_{13}	140	0.850321	0.306149	0.991	4.229
tgδ at 90 °C					
D_{10}	570	1.297158	12.095330	13.686	219.667
D_{11}	148	0.485811	0.126923	1.189	4.664
D_{12}	159	0.548679	0.133394	1.071	4.527
D_{13}	152	1.504605	1.133087	0.793	3.119
D_{14}	99	1.863737	1.848464	0.893	3.297
Oil colour					
D_{10}	2108	2.574953	1.769050	0.822	2.870
D_{11}	650	1.896923	0.597837	0.391	2.606
D_{12}	484	3.026860	3.096386	0.587	2.354
D_{13}	657	3.060122	1.917618	0.128	2.131
Water–soluble acid content					
D_{10}	1191	0.006106	0.000281	11.835	257.889
D_{11}	108	0.004359	0.000005	1.452	6.673
D_{12}	231	0.005529	0.000006	0.025	2.611
D_{13}	92	0.006315	0.000009	0.194	2.655
D_{14}	116	0.006892	0.000008	0.182	2.301
D_{15}	91	0.007679	0.000007	–0.120	2.684
Water content					
D_{10}	1635	14.381787	116.663877	2.723	10.436
D_{11}	284	7.963	13.993306	0.511	2.773
D_{12}	546	9.2768	20.054587	0.469	2.375
D_{13}	520	10.748	16.643352	0.028	2.363

generated for each of the indicators for which a deterioration of the MPV values was detected. To ensure «equality» between the different transformers, a strictly fixed number of observations was selected for each of the indicators for each transformer.

Table 3

Statistical characteristics of homogeneous arrays of 330 kV autotransformer usable oil

Array	N	M_x	D_x	j_s	j_k
Flash point					
D_{10}	856	141.848131	10.217590	0.471	3.210
D_{11}	174	148.063218	4.358072	–0.481	3.198
D_{12}	131	146.122137	2.534701	–0.495	2.794
D_{13}	241	144.792531	1.873969	–0.282	4.092
D_{14}	100	139.360000	2.590400	–0.408	2.882
Organic acid content					
D_{10}	850	0.015665	0.000662	15.882	356.965
D_{11}	180	0.007010	0.000007	0.253	3.007
D_{12}	99	0.007542	0.000009	0.090	2.585
D_{13}	110	0.008343	0.000010	0.104	2.497
D_{14}	114	0.008546	0.000010	–0.015	2.636
D_{15}	206	0.019877	0.000140	0.794	3.373
BDV					
D_{10}	852	68.995188	84.716867	–1.481	10.952
D_{11}	210	74.162857	60.864239	–0.193	3.252
D_{12}	240	68.347500	53.851160	–0.267	3.169
D_{13}	149	66.809396	68.887612	–0.286	2.630
D_{14}	130	65.853077	93.476029	0.0193	2.441
tgδ at 90 °C					
D_{10}	543	0.836640	2.408043	6.572	62.575
D_{11}	162	0.212093	0.018112	0.986	3.825
D_{12}	67	0.701701	0.124185	1.465	5.622
D_{13}	133	0.833985	0.432406	1.486	4.726
D_{14}	138	1.691609	0.984824	0.473	2.499
Contamination content					
D_{10}	122	7.893852	32.249573	2.624	11.631
D_{11}	65	7.239231	9.591576	0.835	4.23
D_{12}	53	10.146226	59.996212	1.549	5.378
Water content					
D_{10}	400	10.123280	30.923324	1.702	11.803
D_{11}	95	4.725653	9.111732	1.987	8.985
D_{12}	155	9.543226	17.576746	0.227	2.332

Similar to [32], an approach based on the extraction of gross omissions from a number of similar measurements was used to further process of the unusable oil indicators values. For this purpose, the Irwin criterion was used, which can be applied when the distribution law of a random variable is unknown or differs from the normal distribution. The values of the oil indicators were sorted in descending order for this purpose, after which the «suspicious» values of the BDV at the boundaries of the variation series were evaluated. The value of the Irwin criterion was defined as:

$$\eta_{\text{calc}} = \frac{\left(x_k - x_{k\ \text{prev}}\right)}{S}, \tag{4}$$

where x_k is the suspicious value; $x_{k\ \text{prev}}$ is the previous value in the variation series.

The calculated value of the Irwin criterion was compared with the table value η_{table}. If $\eta_{\text{calc}} > \eta_{\text{table}}$, then the considered value was rejected and the next value was checked. The test was continued until $\eta_{\text{calc}} < \eta_{\text{table}}$.

By analogy with Tables 2 and 3, Table 4 shows the same attributes for the data sets obtained during statistical processing of unusable oil values for 110 kV transformers. In the table, array D_{21} is based on the results of transformers with less than 20 years of service life, and array D_{22} is based on the results of transformers with more than 20 years of service life.

Table 4

Statistical characteristics of homogeneous arrays of indicators of unusable oil

Array	N	M_x	D_x	j_s	j_k
110 kV transformers					
Organic acid content					
D_{21}	303	0.177673	0.001155	–0.176	2.421
D_{22}	141	0.283191	0.000225	–0.092	2.402
BDV					
D_2	275	27.647	19.814	–0.653	3.083
Water–soluble acid content					
D_2	192	0.035904	0.000154	0.550	3.040
Water content					
D_2	164	36.333659	100.10887	0.505	3.097
330 kV autotransformer					
Organic acid content					
D_2	136	0.137456	0.000273	–0.0113	3.200
BDV					
D_2	123	41.550894	4.880138	–0.666	2.875
Water content					
D_2	132	29.287879	22.728261	–0.0120	2.237

By comparing the statistical characteristics for the respective indicators for usable and unusable oil, it can be seen that the main difference between them is the values of the sample means.

Analysis of the distribution laws for transformer oils. To test the hypothesis that the theoretical distribution law corresponds to empirical data, the software «ZR» developed at the Electric Power Transmission Department of National Technical University «Kharkiv Polytechnic Institute» was used [37]. This software allows splitting the range of variation of a random variable into intervals, for which the Sturges′ rule is used by default:

$$L = 1 + 3{,}322 \cdot \lg N, \tag{5}$$

where N is the volume of sample values.

If necessary, the user can set the required number of intervals himself. A histogram of the empirical distribution is then drawn. The parameters for the normal, beta, exponential, extremal, gamma, Laplace, logistic, logarithmic normal, Rayleigh, Weibull and Pareto distribution laws are then estimated from the sample values. For each of the 11 distribution laws, the theoretical distribution law is checked for consistency with the empirical data, using two statistical criteria [38]:

1) *Pearson's chi-squared test* (χ^2):

$$\chi^2 = \sum_{i=1}^{k} \frac{(n_i - n_i')^2}{n_i'} \qquad (6)$$

where n_i are values of empirical frequencies; n'_i are values of theoretical frequencies; k is the number of intervals.

To test the main hypothesis, the sample value of criterion χ^2 is calculated and the critical point of criterion χ^2 distribution, the given significance level α and the number of degrees of freedom f are determined by the critical point $\chi^2_{\text{crit}}(\alpha; f)$. The number of degrees of freedom f is defined as $f = k - 1 - r$, where k is the number of sample groups (partial intervals); r is the number of estimated distribution parameters that are estimated from the sample data.

If the calculated value of χ^2 criterion is less than the critical value, the main hypothesis – the general population is distributed according to the given law – is not rejected and vice versa.

2) *Kolmogorov-Smirnov test*:

$$D_n = \sup_x \left| F_n(x) - F(x) \right|, \qquad (7)$$

where $F_n(x)$ is the empirical distribution function; $F(x)$ is the theoretical distribution function.

The main hypothesis is rejected if $\sqrt{n} \cdot D_n$ exceeds the distribution quantile $K\alpha$ of the given significance level α, and is not rejected otherwise [38].

Analysis by the software showed that both usable and unusable oil values could be described by a Weibull distribution, with a distribution density as follows:

$$p(x;\alpha;\beta) = \frac{\beta}{\alpha^{\beta}} \cdot x^{\beta-1} \cdot e^{-\left(\frac{x}{\alpha}\right)^{\beta}}, \qquad (8)$$

where α and β are distribution law parameters, interpreted as scale and shape parameter, respectively.

The value of the α and β parameters was defined as:

$$\alpha = \frac{M(x)}{1 - 0.427 \cdot (\beta - 1) \cdot \beta^{-1.9}};$$

$$\beta = \frac{N-1}{N} \cdot \left(0.465 \cdot \frac{\left[\frac{1}{N} \cdot \sum_{i=1}^{N} (x_i - M(x))^2 \right]^{\frac{1}{2}}}{M(x)} + \right.$$

$$\left. + 1.282 \cdot \frac{M(x)}{\left[\frac{1}{N} \cdot \sum_{i=1}^{N} (x_i - M(x))^2 \right]^{\frac{1}{2}}} - 0.7 \right),$$

where N is the volume of sample values; M_x is the sample mean; x_i is the indicator value.

However, during the analysis, for some of the arrays the main hypothesis was not rejected for several distribution laws. Thus, for distributions with positive skewness, in addition to the Weibull distribution, the empirical data were fit to the log-normal, gamma and Rayleigh distribution laws.

As an example, Fig. 2 shows histograms of the empirical distribution and the theoretical density functions

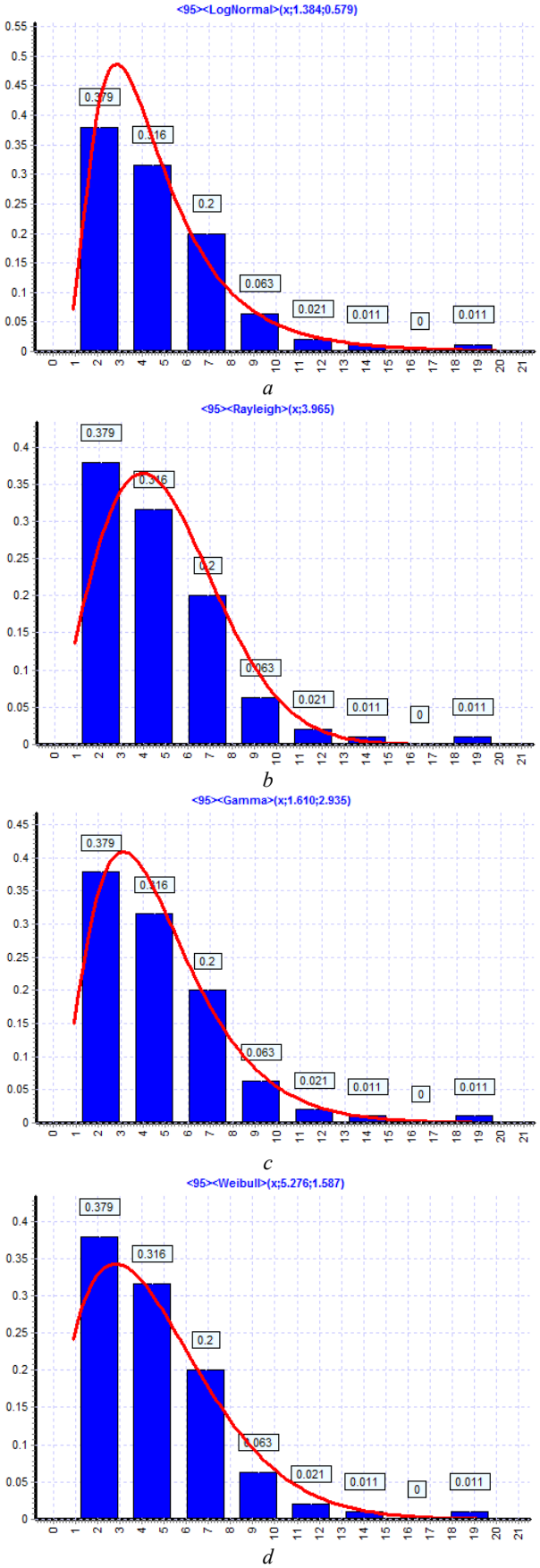

Fig. 2. Histograms of the empirical distribution and the theoretical density functions of some distributions for the water content of oil from the D_{11} array of 330kV autotransformers: *a* – log-normal distribution law; *b* – Rayleigh distribution; *c* – gamma distribution; *d* – Weibull distribution

of these distributions for the water content of oil from the D_{11} array of 330 kV autotransformers.

For relatively symmetric distributions, in addition to the Weibull distribution, for some of the arrays the empirical data were found to fit the normal and logistic laws. However, for many arrays with negative skewness, the only distribution law corresponding to the empirical data was a Weibull distribution law.

The values of the Weibull distribution law parameters as well as the calculated and critical values of the Pearson and Kolmogorov-Smirnov tests for the indicators of usable oil in 110 kV transformers are given in Table 5 and for 330 kV autotransformers are given in Table 6.

The same, but for the unusable oil indicators are given in Table 7. For the tables below, the λ_{crit} value of the Kolmogorov-Smirnov test is 1.36.

As can be seen from Tables 6, 7, the calculated values of the goodness of fit criteria for all transformer oil indicators without exception do not exceed the critical values at significance level α = 0.05 and the corresponding value of degrees of freedom. This does not allow rejecting the hypothesis about the acceptability of the distribution of empirical values of transformer oils to the Weibull distribution.

Results analysis. By analogy with [32], the analysis of the mutual arrangement of theoretical densities of distribution of the indicators of usable and unusable transformer oils in of 110 and 330 kV transformers was carried out. As an example Figures 3-5 shows the densities of theoretical distributions for such indicators as the organic acid content (Fig. 3), water content (Fig. 4) and the BDV (Fig. 5) of the oil.

Analysing the mutual arrangement of the theoretical distribution densities of transformer oil indicators, several important conclusions can be drawn:

1. For the usable transformer oil for both 110 kV transformers and 330 kV autotransformers, there is a shift in the mathematical expectations of the distributions density for different arrays of the same indicator. This indicates a different oil ageing degree, which is caused by different oil service life, different operating temperatures of transformers as well as by the influence of structural materials.

2. Analysis of the distribution densities of usable oil for 110 kV transformers and 330 kV autotransformers shows that these distributions are also shifted in relation to each other. It is especially noticeable in the distribution densities of organic acids (Fig. 3) and water content of oils (Fig. 4). Thus, as can be seen from the figure the oxidation intensity of transformer oils in 330 kV autotransformers is lower than in 110 kV transformers, despite the fact that the analysed transformers were non-sealed.

3. The analysis shows that there is a significant shift between the mathematical expectations of the distributions of usable and unusable oil (Figures 3-5). This means that the residual life of the oils in the transformers analysed varies considerably.

Table 5

Values of the Weibull distribution law parameters as well as the calculated and critical values of the Pearson and Kolmogorov-Smirnov tests for the indicators of usable oil in 110 kV transformers

Array	Distribution law parameters		Value of Pearson's chi-squared test			Value of Kolmogorov-Smirnov test
	α	β	f	χ^2_{calc}	χ^2_{crit}	λ_{calc}
Flash point						
D_{11}	140.96	104.9	3	7.47	7.82	0.711
D_{12}	143.71	127.5	4	8.59	9.49	1.194
D_{13}	145.54	96.44	3	7.47	7.82	0.338
D_{14}	148.91	46.2	4	8.26	9.49	0.694
D_{15}	150.69	59.57	3	6.27	7.82	1.044
Organic acid content						
D_{11}	0.0172	1.682	6	10.47	12.6	0.711
D_{12}	0.0308	3.706	5	21.26	11.1	1.001
D_{13}	0.0518	2.454	6	8.54	12.6	0.654
D_{14}	0.0514	3.702	4	7.92	9.49	0.674
D_{15}	0.0581	2.611	5	10.68	11.1	0.800
D_{16}	0.0519	2.154	4	6.074	9.49	0.545
D_{17}	0.0725	1.679	6	10.96	12.6	0.760
BDV						
D_{11}	51.833	8.704	4	8.942	9.49	0.711
D_{12}	64.963	6.596	7	12.03	14.1	0.607
D_{13}	72.625	7.209	6	12.21	12.6	0.643
D_{14}	73.726	7.84	5	6.419	11.1	0.606
D_{15}	75.623	7.517	5	6.59	11.1	0.601
tgδ at 20 °C						
D_{11}	0.1576	1.515	4	9.439	9.49	1.017
D_{12}	0.2103	1.569	4	9.095	9.49	0.639
tgδ at 70 °C						
D_{11}	0.3221	1.491	4	5.079	9.49	0.697
D_{12}	0.6585	1.496	4	6.465	9.49	0.673
D_{13}	0.9478	1.562	4	1.865	9.49	0.311
tgδ at 90 °C						
D_{11}	0.5327	1.379	3	2.296	7.82	0.329
D_{12}	0.6101	1.526	3	1.173	7.82	0.275
D_{13}	1.6593	1.432	3	4.737	7.82	0.734
D_{14}	2.0442	1.383	3	2.764	7.82	0.383
Oil colour						
D_{11}	2.1334	2.631	3	6.794	7.82	0.690
D_{12}	3.4054	1.772	4	8.456	9.49	0.739
D_{13}	3.453	2.339	3	6.523	7.82	0.656
Water-soluble acid content						
D_{11}	0.0049	1.986	2	2.765	5.99	0.449
D_{12}	0.0062	2.365	6	6.383	12.6	0.446
D_{13}	0.0071	2.207	4	1.468	9.49	0.288
D_{14}	0.0078	2.554	4	3.736	9.49	0.378
D_{15}	0.0086	3.112	3	2.277	7.82	0.344
Water content						
D_{11}	8.9923	2.239	5	2.137	11.1	0.279
D_{12}	10.478	2.176	7	10.06	14.1	0.552
D_{13}	12.05	2.849	7	8.763	14.1	0.385

Table 6

Values of the Weibull distribution law parameters as well as the calculated and critical values of the Pearson and Kolmogorov-Smirnov tests for the indicators of usable oil in 330 kV autotransformers

Array	Distribution law parameters		Value of Pearson's chi-squared test			Value of Kolmogorov-Smirnov test
	α	β	f	χ^2_{calc}	χ^2_{crit}	λ_{calc}
Flash point						
D_{11}	149.16	89.71	4	8.848	9.49	0.672
D_{12}	146.99	116.1	4	9.330	9.49	0.556
D_{13}	145.54	134.3	3	7.510	7.82	0.971
D_{14}	140.23	109.2	4	8.678	9.49	0.671
Organic acid content						
D_{11}	0.0079	2.899	2	0.609	5.99	0.228
D_{12}	0.0085	2.766	4	5.851	9.49	0.586
D_{13}	0.0094	2.812	5	9.364	11.1	0.693
D_{14}	0.0096	2.986	3	1.939	7.82	0.401
D_{15}	0.0223	1.725	2	4.943	5.99	0.699
BDV						
D_{11}	77.523	11.48	3	5.235	7.82	0.890
D_{12}	71.499	11.24	4	8.207	9.49	0.893
D_{13}	70.319	9.612	4	2.768	9.49	0.260
D_{14}	69.855	8.038	4	9.229	9.49	0.754
tgδ at 90 °C						
D_{11}	0.237	1.605	3	1.485	7.82	0.459
D_{12}	0.7926	2.055	2	2.710	5.99	0.509
D_{13}	0.9018	1.283	3	7.286	7.82	0.760
D_{14}	1.9017	1.745	4	0.685	9.49	0.181
Contamination content						
D_{11}	8.1592	2.457	2	3.024	5.99	0.709
D_{12}	11.018	1.309	1	1.052	3.84	0.335
Water content						
D_{11}	5.2755	1.587	1	1.068	3.84	0.178
D_{12}	10.762	2.407	5	3.305	11.1	0.301

Table 7

Values of the Weibull distribution law parameters as well as the calculated and critical values of the Pearson and Kolmogorov-Smirnov tests for the indicators of unusable oil in 110 kV transformers and 330 kV autotransformers

Array	Distribution law parameters		Value of Pearson's chi-squared test			Value of Kolmogorov-Smirnov test
	α	β	f	χ^2_{calc}	χ^2_{crit}	λ_{calc}
110 kV transformer						
Organic acid content						
D_{21}	0.1911	6.07	6	2.990	12.6	0.376
D_{22}	0.2901	23.36	4	1.843	9.49	0.265
BDV						
D_2	29.459	7.311	4	3.162	9.49	0.228
Water-soluble acid content						
D_2	0.0401	3.155	5	3.009	11.1	0.420
Water content						
D_2	39.98	4.059	3	1.850	7.82	0.338
330 kV autotransformer						
Organic acid content						
D_2	0.1445	9.955	4	7.427	9.49	0.704
BDV						
D_2	42.576	23.25	4	2.763	9.49	0.323
Water content						
D_2	31.232	7.196	4	2.690	9.49	0.407

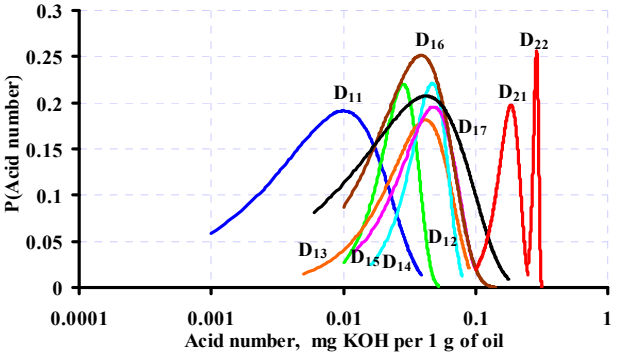

a

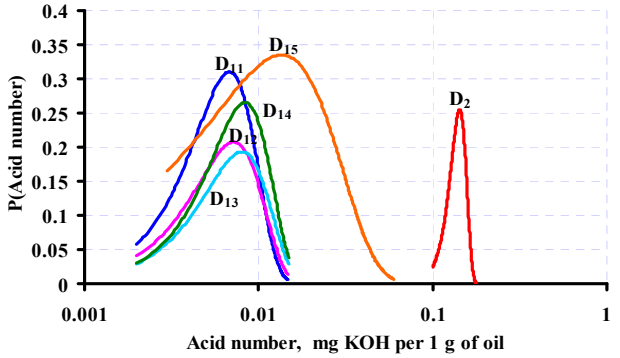

b

Fig. 3. Density functions of the theoretical distribution of organic acid content in oil for 110 kV transformers (*a*) and 330 kV autotransformers (*b*)

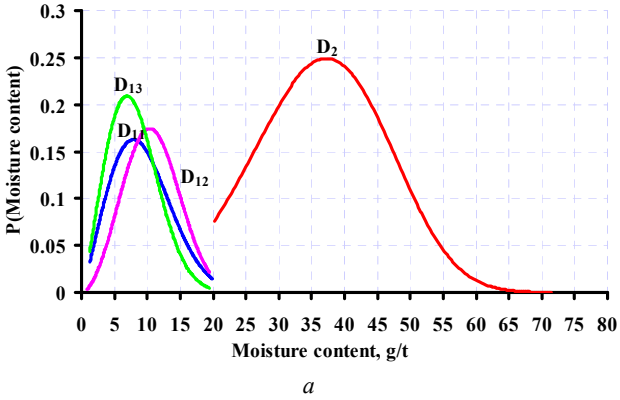

a

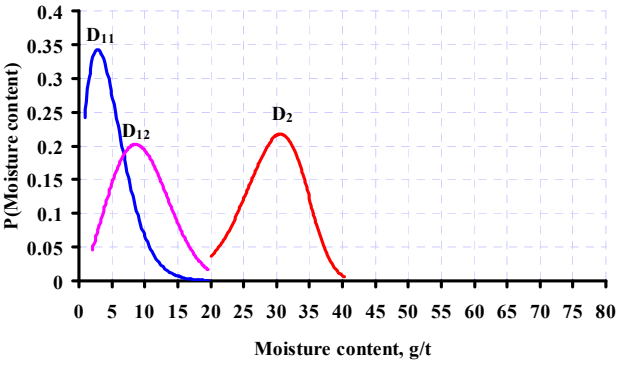

b

Fig. 4. Density functions of the theoretical distribution of water content in oil for 110 kV transformers (*a*) and 330 kV autotransformers (*b*)

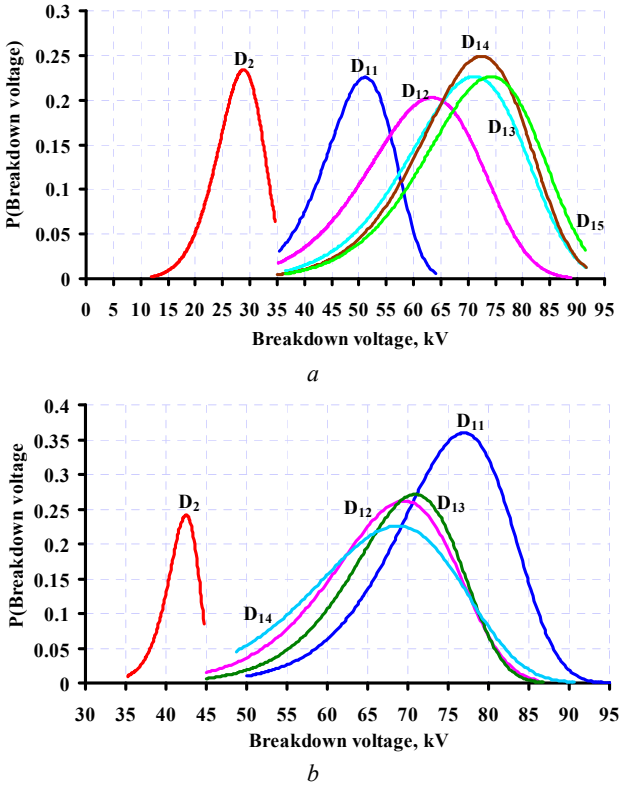

Fig. 5. Density functions of the theoretical distribution of the BDV in oil for 110 kV transformers (*a*) and 330 kV autotransformers (*b*)

Conclusions.

The analysis of the distribution laws of transformer oils showed that for both usable and unusable oil the distribution of oil indicators could be described by the Weibull distribution, which agrees well with the results of previously published studies. In the process of analysis, it was found that for the usable transformer oil, both for 110 kV transformers and 330 kV autotransformers there is a shift of mathematical expectations of the distribution density for different arrays of the same indicator. This indicates a different oil ageing degree which is caused by different oil service life, different operating temperatures of transformers as well as by the influence of structural materials. During the analysis, it was found that in 330 kV autotransformers the oxidation reactions proceed with less intensity compared to 110 kV transformers. This is evidenced by the presence of a shift between the distribution densities of some indicators of usable oil in 110 kV transformers and 330 kV autotransformers. It has been found that there is a significant shift between the mathematical expectations of the distributions of usable and unsuitable oil. This means that the residual life of oils in transformers analysed varies significantly. The obtained values of the parameters of the distribution laws of transformer oil indicators can be used in the development of models to estimate the service life of oils, as well as to predict and plan the timing of maintenance and repair of equipment, which will allow to carry out the transition to maintenance according to the real situation rather than the calendar plan. In addition, the presence of distribution law parameter values for indicators of oil with different states allow to estimate the state of transformer oils using likelihood ratios, which can significantly reduce the risks of making wrong decisions.

Conflict of interests. The authors declare no conflicts of interest.

REFERENCES

1. N'cho J., Fofana I., Hadjadj Y., Beroual A. Review of Physicochemical-Based Diagnostic Techniques for Assessing Insulation Condition in Aged Transformers. *Energies*, 2016, vol. 9, no. 5, p. 367. doi: https://www.doi.org/10.3390/en9050367.

2. Mehmood M., Nazir M., Li J., Wang F., Azam M. Comprehensive Investigation on Service Aged Power Transformer Insulating Oil After Decades of Effective Performance in Field. *Arabian Journal for Science and Engineering*, 2020, vol. 45, no. 8, pp. 6517-6528. doi: https://www.doi.org/10.1007/s13369-020-04559-7.

3. Rengaraj R., Venkatakrishnan G.R., Moorthy P., Pratyusha R., Ritika, Veena K. Transformer Oil Health Monitoring Techniques–An Overview. *Advances in Intelligent Systems and Computing*, 2020, pp. 135-154. doi: https://www.doi.org/10.1007/978-981-15-5029-4_12.

4. Tyuryumina A., Batrak A., Sekackiy V. Determination of transformer oil quality by the acoustic method. *MATEC Web of Conferences*, 2017, vol. 113, p. 01008. doi: https://www.doi.org/10.1051/matecconf/201711301008.

5. Leong Y., Ker P., Jamaludin M., Nomanbhay S.M., Ismail A., Abdullah F., Looe H., Lo C. UV-Vis Spectroscopy: A New Approach for Assessing the Color Index of Transformer Insulating Oil. *Sensors*, 2018, vol. 18, no. 7, p. 2175. doi: https://www.doi.org/10.3390/s18072175.

6. Kang S.B., Kim W.-S., Chung D.C., Joung J.M., Kwak M.H. Degradation diagnosis of transformer insulating oils with terahertz time-domain spectroscopy. *Journal of the Korean Physical Society*, 2017, vol. 71, no. 12, pp. 986-992. doi: https://www.doi.org/10.3938/jkps.71.986.

7. Alshehawy A.M., Mansour D.A., Ghali M., Rezk A. Evaluating the impact of aging in field transformer oil using optical spectroscopy techniques. *2017 IEEE 19th International Conference on Dielectric Liquids (ICDL)*, 2017, pp. 1-4. doi: https://www.doi.org/10.1109/ICDL.2017.8124626.

8. Degeratu S., Rotaru P., Rizescu S., Danoiu S., Bizdoaca N.G., Alboteanu L.I., Manolea H.O. Condition monitoring of transformer oil using thermal analysis and other techniques. *Journal of Thermal Analysis and Calorimetry*, 2015, vol. 119, no. 3, pp. 1679-1692. doi: https://www.doi.org/10.1007/s10973-014-4276-3.

9. Zhao Y., Qian Y., Li L., Zheng Z., Wang Q., Zhou Y. Research on Transformer Oil Multi-frequency Ultrasonic Monitoring Technology Based on Convolutional Neural

Network. *2019 IEEE 20th International Conference on Dielectric Liquids (ICDL)*, 2019, pp. 1-5. doi: https://www.doi.org/10.1109/ICDL.2019.8796733.

10. Srividhya V., Babu J.S., Sujatha K., Veerendrakumar J., Aruna M., Shafiya S., SaiKrishna, Anand M. Determination of Breakdown Voltage for Transformer Oil Testing Using ANN. *Advances in Intelligent Systems and Computing*, 2021, pp. 443-452. doi: https://www.doi.org/10.1007/978-981-33-6981-8_35.

11. Singh H., Singh J. Enhanced optimal trained hybrid classifiers for aging assessment of power transformer insulation oil. *World Journal of Engineering*, 2020, vol. 17, no. 3, pp. 407-426. doi: https://www.doi.org/10.1108/wje-11-2019-0339.

12. Gautam L., Kumar R., Sood Y.R., Identifying Transformer Oil Criticality Using Fuzzy Logic Approach. *2020 IEEE Students Conference on Engineering & Systems (SCES)*, 2020, pp. 1-6. doi: https://www.doi.org/10.1109/SCES50439.2020.9236724.

13. Milosavljevic S., Janjic A. Integrated Transformer Health Estimation Methodology Based on Markov Chains and Evidential Reasoning. *Mathematical Problems in Engineering*, 2020, vol. 2020, pp. 1-12. doi: https://www.doi.org/10.1155/2020/7291749.

14. Surya Subaga I.G., Manuaba I.B.G., Sukerayasa I.W. Analisis Prediktif Pemeliharaan Minyak Transformator Menggunakan Metode Markov. *Jurnal SPEKTRUM*, 2019, vol. 6, no. 4, pp. 96-101. (Ind). Available at: https://ojs.unud.ac.id/index.php/spektrum/article/view/55335/32753 (Accessed 22 May 2021).

15. Rexhepi V., Nakov P. Condition assessment of power transformers status based on moisture level using fuzzy logic techniques. *Journal of Mechatronics, Electrical Power, and Vehicular Technology*, 2018, vol. 9, no. 1, pp. 17-24. doi: https://www.doi.org/10.14203/j.mev.2018.v9.17-24.

16. Chantola A., Sharma M., Saini A. Integrated Fuzzy Logic Approach for Calculation of Health Index of Power Transformer. *2018 Second International Conference on Inventive Communication and Computational Technologies (ICICCT)*, 2018, pp. 1045-1050. doi: https://www.doi.org/10.1109/ICICCT.2018.8473316.

17. Shutenko O., Ponomarenko S. Diagnostics of Transformer Oils Using the Multiple Linear Regression Model *2020 IEEE Problems of Automated Electrodrive. Theory and Practice (PAEP)*, 2020, pp. 1-6, doi: https://www.doi.org/10.1109/PAEP49887.2020.9240875.

18. Abdi S., Harid N., Safiddine L., Boubakeur A., Haddad A. The Correlation of Transformer Oil Electrical Properties with Water Content Using a Regression Approach. *Energies*, 2021, vol. 14, no. 8, p. 2089. doi: https://www.doi.org/10.3390/en14082089.

19. Gouda O., El Dein A. Prediction of Aged Transformer Oil and Paper Insulation. *Electric Power Components and Systems*, 2019, vol. 47, no. 4-5, pp. 406-419. doi: https://www.doi.org/10.1080/15325008.2019.1604848.

20. *IEC 60422. Mineral insulating oils in electrical equipment - Supervision and maintenance guidance*. 2012.

21. *SOU-N EE 43-101:2009. Adoption, application and use of transformer oils. Quality assessment standards*. Kyiv, 2018. (Ukr).

22. Davidenko I.V., Egorov A.A. Determination of Criteria for Assessing the Oil Quality of Current Transformers Type TFZM 110 kV. *2020 IEEE Conference of Russian Young Researchers in Electrical and Electronic Engineering (EIConRus)*, 2020, pp. 1204-1207. doi: https://www.doi.org/10.1109/EIConRus49466.2020.9039527.

23. Azis N., Zhou D., Wang Z.D., Jones D., Wells B., Wallwork G.M. Operational condition assessment of in-service distribution transformers. *2012 IEEE International Conference on Condition Monitoring and Diagnosis*, 2012, pp. 1156-1159. doi: https://www.doi.org/10.1109/CMD.2012.6416364.

24. Davidenko I., Egorov A. Development of an integral criterion for evaluating the degree of aging of transformer oils. *IOP Conference Series: Materials Science and Engineering*, 2020, vol. 950, p. 012005. doi: https://www.doi.org/10.1088/1757-899x/950/1/012005.

25. Shutenko O. Determine the boundary value of the concentration of gases dissolved in oil of method minimum risk. *2017 IEEE First Ukraine Conference on Electrical and Computer Engineering (UKRCON)*, 2017, pp. 468-472. doi: https://www.doi.org/10.1109/UKRCON.2017.8100533.

26. Shutenko O., Zagaynova A., Serdyukova G. Determining the maximally permissible values for the indicators of insulation of sealed entrance bushings with a voltage of 110 kV using the method of minimal risk. *Eastern-European Journal of Enterprise Technologies*, 2018, vol. 5, no. 8 (95), pp. 6-15. doi: https://www.doi.org/10.15587/1729-4061.2018.142185.

27. Mohd Selva A., Azis N., Shariffudin N.S., Ab Kadir M.Z.A., Jasni J., Yahaya M.S., Talib M.A. Application of Statistical Distribution Models to Predict Health Index for Condition-Based Management of Transformers. *Applied Sciences*, 2021, vol. 11, no. 6, pp. 2728. doi: https://www.doi.org/10.3390/app11062728.

28. Tsuboi T., Takami J., Okabe S., Inami K., Aono K. Aging effect on insulation reliability evaluation with Weibull distribution for oil-immersed transformers. *IEEE Transactions on Dielectrics and Electrical Insulation*, 2010, vol. 17, no. 6, pp. 1869-1876. doi: https://www.doi.org/10.1109/TDEI.2010.5658240.

29. Birger I.A. *Technical diagnostics*. Moscow, Mashinostroenie Publ., 1978. 240 p. (Rus).

30. Davidenko I.V. Determination of allowable values of controlled parameters of oil-filled equipment on the basis of an array of observed data. *Elektrichestvo*, 2009, no. 6, pp. 10-21. (Rus). Available at: https://elibrary.ru/download/elibrary_12880537_35897195.pdf (Accessed 22 May 2021).

31. Davidenko I.V. Investigation of indicators describing the operational state of oil-filled bushings, using mathematical statistics. *University news. North-Caucasian region. Technical sciences series*, 2006, no. 15, pp. 31-33. (Rus).

32. Shutenko O., Zagaynova A., Serdyukova G. Analysis of distribution laws of insulation indicators of high-voltage oil-fillled bushings of hermetic and non-hermetic execution. *Technology audit and production reserves*, 2018, vol. 4, no. 1 (42), pp. 30-39. doi: https://www.doi.org/10.15587/2312-8372.2018.140873.
33. Lipstein R.A., Shakhnovich M.I. *Transformer oil*. Moscow, Energoatomizdat Publ., 1983. 296 p. (Rus).
34. Vasilevskij V.V. Assessment of the resource consumption of oil-filled power transformer paper insulation based on updated aging integral. *Electrical Engineering & Electromechanics*, 2015, no. 1, pp. 16-19. (Rus). doi: https://www.doi.org/10.20998/2074-272x.2015.1.03.
35. Poliakov M.A., Vasilevskij V.V. Evaluation of power transformer insulation residual life based on its individual life cycle characteristics. *Electrical Engineering & Electromechanics*, 2014, no. 3, pp. 38-41. (Rus). doi: https://www.doi.org/10.20998/2074-272x.2014.3.07.
36. Shutenko O., Ponomarenko S. Analysis of the Impact of Power Transformer Loading on the Transformer Oil Aging Intensity. *2020 IEEE KhPI Week on Advanced Technology (KhPIWeek)*, 2020, pp. 76-81. doi: https://www.doi.org/10.1109/KhPIWeek51551.2020.9250159.
37. Shutenko O.V., Baklay D.N. *Planning of experimental research in power engineering. Methods of Processing of Experimental Data*. Kharkiv, NTU «KhPI» Publ., 2013. 268 p. (Rus).
38. Rinne H. *The Weibull distribution*. Boca Raton, CRC Press, 2009. 808 p.

Received 15.07.2021
Accepted 24.09.2020
Published 26.10.2021

O. Shutenko[1]*, PhD, Associate Professor,*
S. Ponomarenko[1]*, PhD Student,*
[1] National Technical University «Kharkiv Polytechnic Institute»,
2, Kyrpychova Str., Kharkiv, 61002, Ukraine,
e-mail: o.v.shutenko@gmail.com,
PonomarenkSerhii@gmail.com (Corresponding author)

How to cite this article:
Shutenko O., Ponomarenko S. Analysis of distribution laws of transformer oil indicators in 110-330 kV transformers. *Electrical Engineering & Electromechanics*, 2021, no. 5, pp. 46-56. doi: https://doi.org/10.20998/2074-272X.2021.5.07.

UDC 621.3 https://doi.org/10.20998/2074-272X.2021.5.08

H. Sahraoui, H. Mellah, S. Drid, L. Chrifi-Alaoui

ADAPTIVE MAXIMUM POWER POINT TRACKING USING NEURAL NETWORKS FOR A PHOTOVOLTAIC SYSTEMS ACCORDING GRID

Introduction. *This article deals with the optimization of the energy conversion of a grid-connected photovoltaic system.* ***The novelty*** *is to develop an intelligent maximum power point tracking technique using artificial neural network algorithms.* ***Purpose.*** *Intelligent maximum power point tracking technique is developed in order to improve the photovoltaic system performances under the variations of the temperature and irradiation.* ***Methods.*** *This work is to calculate and follow the maximum power point for a photovoltaic system operating according to the artificial intelligence mechanism is and the latter is used an adaptive modified perturbation and observation maximum power point tracking algorithm based on function sign to generate an specify duty cycle applied to DC-DC converter, where we use the feed forward artificial neural network type trained by Levenberg-Marquardt backpropagation.* ***Results.*** *The photovoltaic system that we chose to simulate and apply this intelligent technique on it is a stand-alone photovoltaic system. According to the results obtained from simulation of the photovoltaic system using adaptive modified perturbation and observation – artificial neural network the efficiency and the quality of the production of energy from photovoltaic is increased.* ***Practical value.*** *The proposed algorithm is validated by a dSPACE DS1104 for different operating conditions. All practice results confirm the effectiveness of our proposed algorithm.* References 37, table 1, figures 27.

Key words: **artificial neural network, grid-connected, adaptive modified perturbation and observation, artificial neural network-maximum power point tracking.**

Вступ. *У статті йдеться про оптимізацію перетворення енергії фотоелектричної системи, підключеної до мережі.* ***Новизна*** *полягає у розробці методики інтелектуального відстеження точок максимальної потужності з використанням алгоритмів штучної нейронної мережі.* ***Мета***. *Методика інтелектуального відстеження точок максимальної потужності розроблена з метою поліпшення характеристик фотоелектричної системи в умовах зміни температури та опромінення.* ***Методи***. *Робота полягає в обчисленні та відстеженні точки максимальної потужності для фотоелектричної системи, що працює відповідно до механізму штучного інтелекту, і в останній використовується адаптивний модифікований алгоритм збурення та відстеження точок максимальної потужності на основі знаку функції для створення заданого робочого циклу стосовно DC-DC перетворювача, де ми використовуємо штучну нейронну мережу типу «прямої подачі», навчену зворотному розповсюдженню Левенберга-Марквардта.* ***Результати***. *Фотоелектрична система, яку ми обрали для моделювання та застосування цієї інтелектуальної методики, є автономною фотоелектричною системою. Відповідно до результатів, отриманих при моделюванні фотоелектричної системи з використанням адаптивних модифікованих збурень та спостереження – штучної нейронної мережі, ефективність та якість виробництва енергії з фотоелектричної енергії підвищується.* ***Практична цінність***. *Запропонований алгоритм перевірено dSPACE DS1104 для різних умов роботи. Усі практичні результати підтверджують ефективність запропонованого нами алгоритму.* Бібл. 37, табл. 1, рис. 27.

Ключові слова: **штучна нейронна мережа, підключена до мережі, адаптивне модифіковане збурення та спостереження, штучна нейронна мережа-відстеження точки максимальної потужності.**

Introduction. Nowadays, the electric power generation mainly uses fossil and fissile (nuclear) fuels. The widespread use of fossil fuels, such as gasoline, coal or natural gas, allows for low production prices. On the other hand, their use results in a large release of greenhouse gases and polluting gases. Electricity production from fossil fuels has a great responsibility for global CO_2 emissions, hence pollution, according to the last International Energy Agency report [1]. Nuclear power, which does not directly release carbon dioxide, the risks of accident linked to their exploitation are very low but the consequences of an accident would be disastrous. Although the risks of accident linked to their exploitation are very low, but the consequences of an accident would be disastrous and we must not forget the Fukushima Daiichi nuclear disaster in Japan. Furthermore, the treatment of waste from this mode of production is very expensive; the radioactivity of the treated products remains high for many years [2], that's what prompted to the propose a nuclear plant waste management policies and strategies [2], and some researcher suggests to build a regional and global nuclear security system [3]. Finally, uranium reserves are like those of limited oil [4].

Although the world is in surplus in electricity production today, the future is therefore not promising on fossil fuel resources whose reserves are constantly decreasing and whose prices fluctuate enormously depending on the economic situation [5]. The future preparations in the fields of energy production to satisfy the humanity needs should be foreseen today, in order to be able to gradually face the inevitable energy changes.

Each innovation and each breakthrough in research will only have repercussions in about ten years at best, the time to carry out the necessary tests and to consider putting into production without risk for the user as much for his own health than for its electrical installations, to avoid the problems of pollution in the production of electricity, alternative solutions can be photovoltaic (PV), wind, or even hydroelectric sources [4, 5].

The use of PV solar energy seems to be a necessity for the future. Indeed, solar radiation constitutes the most abundant energy resource on earth. The amount of energy released by the Sun, for one hour could be enough to cover global energy needs for a year, for that we should better exploit this energy and optimize its collection by PV collectors [6].

The basic element of a PV system is the solar panel which is made up of photosensitive cells connected to each other. Each cell converts the rays from the Sun into continuous type electricity. PV panels have a specific highly non-linear electrical characteristic which appears clearly in the current-voltage and power-voltage curves [7]. Its electrical characteristics have a particular point

called Maximum Power Point (MPP). This point is the optimal operating point for which the panel operates at its maximum power, MPP is highly dependent on climatic conditions and load, which makes the position of the MPP variable over time and therefore difficult to locate [8].

A Maximum Power Point Tracking (MPPT) control is associated with an intermediate adaptation stage, allowing the PV to operate at the MPP so as to continuously produce the maximum power of PV, whatever the weather conditions (temperature and irradiation), and whatever the charge. The converter control places the system at MPP this point defined by current I_{mpp} and voltage V_{mpp}. There are several MPPT techniques that aim to extract maximum power from the solar cells outputs [9-12] the interested reader is referred to [11] for more details. Classic techniques such as the Incremental Conductance technique and Perturbation and Observation (P&O) technique, these two methods are the most used and easy to implement methods but have drawbacks [10-13].

New techniques based on artificial intelligence, such as Fuzzy Logic Control [14, 15] Squirrel Search Algorithm [16], Particle Swarm Optimization [17], Levy Flight Optimization [12], Artificial Neural Networks (ANN) [18, 19], and other propose a hybrid techniques [20-23].

The methods based on ANN allow solving non-linear problems and more complicated by a very fast way since they are represented by non-linear mathematical functions [24]. A different ANN-MPPT algorithm for maximization of power PV production have been studied in many research papers [18, 19, 25]. Messalti et al. in [19] proposes with experimental validation two versions of ANN-MPPT controllers either with fixed or variable step. The aim of their works was to propose an optimal MPPT controller based on neural network for used it in the PV system. Different operating climatic conditions are investigated in the ANN training step in order to improve, tracking accuracy, response time and reduce a chattering.

Kumar et al. in [26] propose two Neural Networks (NN) in the purpose of PV grid-connected with multi-objective and distributed system; one is for assuring MPPT and the other for the generation of reference currents; the NN used for MPPT is based on hill climbing learning algorithm, and use a NN version of a Power Normalized Kernel Least Mean Fourth algorithm control (PNKLMF-NN) to generate a reference currents.

Tavakoliel al. in [27] propose an intelligent method for MPPT control in PV systems, this study establishes a two-level adaptive control framework to increase its efficiency by facilitating system control and efficiently handling uncertainties and perturbations in PV systems and the environment; where the ripple correlation control is the first level of control and the second level is based on an adaptive controller rule for the Model Reference Adaptive Control system and is derived through the use of a self-constructed Lyapunov neural network. However, this approach did not been applied in the purpose of grid connected PV system.

In [28] the authors have made a new technique – a Adaptive Modified Perturbation and Observation (AMPO), which reduces the MPP search steps this last based on the function which widely used in sliding mode control sign function, by this technique of reducing the calculation time and the chattering; compared to classic P&O technique.

Many authors study the issues of PV system grid connection [26], [29-31]. Slama et al. in [29] offer a clever algorithm for determining the best hours to switch between battery and PVs, on the other hand, Belbachir et al. in [30] seeks the optimal integration, both for distributed PVs and for the batteries, other deal with the management of electricity consumption [31].

In this paper, we propose an adaptive P&O algorithm technique based on neural network with the PV system to increase the power of PV and operate at MPP, whatever the climatic variation such as the radiation and the temperature, according a grid demand.

The main contribution of this work is to present an Adaptive Modified Perturbation and Observation – Artificial Neural Networks (AMPO-ANN) based on the sign function which simplifies and reduces the step and time of calculating MPPT point which allows minimizing both the calculation time, the structure of the classic P&O algorithm and the AMPO-ANN designing. Furthermore, in the purpose of real-time application the major problem in a neural network framework is the large size of the created program who add a difficult to implant, especially for the realization of a complex system with small time constant.

We are mainly interested in the development of a control system based on ANN which allows the continuation of the MPP by simulation and experiments, which allows increasing the performance of the neural MPPT chart compared to the other maximization methods. Figure 1 below presents a proposed system of control.

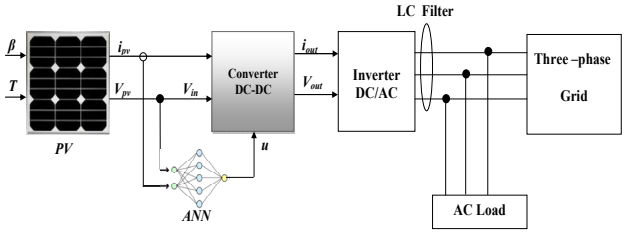

Fig. 1. Schematic diagram of the PV system under study with AMPO-ANN strategy

The goal of the paper is to develop a technique of maximization power point tracking search based on the function sign which simplifies and reduces the step size and the computation time of the maximum power point tracking point which minimize both calculation time.

Subject of investigations. This paper is valid power maximization technique-based neurons networks by a test bench with a dSPACE DS1104.

Description and modeling of proposed PV system. Equation (1) describes the PV cell model, this model (Fig. 2) can be definite by the application of standard data given by the manufacturer. The equivalent circuit for PV cell is presented as follow [32].

The typical equation for a single-diode of PV panel is as follows:

$$I_{pv} = I_{ph} - I_s\left(e^{\frac{V_{pv}+R_sI_{pv}}{aV_T}} - 1\right) - \frac{V_{pv}+R_sI_{pv}}{R_{sh}}, \quad (1)$$

where I_{pv} is the current generated by PV panel; I_{ph} is the generated photo-current; I_s is the current of saturation; V_{pv} is the voltage of PV panel; R_s is the array's equivalent series resistance; a is the constant of the ideal diode VD; V_T is the thermal voltage of PV ($V_T = KT/q$, where K is the Boltzmann's constant; T is the temperature of PV; q is the charge of an electron); R_{sh} is the array's equivalent parallel resistance.

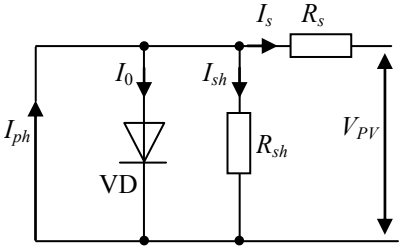

Fig. 2. The PV cell equivalent circuit

Figures 3 and 4 illustrate the PV panel's characteristics as they change; both temperatures between 25 to 75 °C and irradiation between 200 to 1000 W/m^2 respectively.

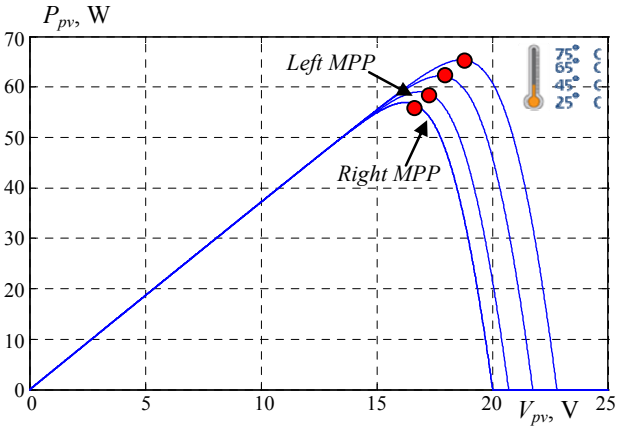

Fig. 3. Characteristics $P = f(V)$ of the PV panel under variation of temperature

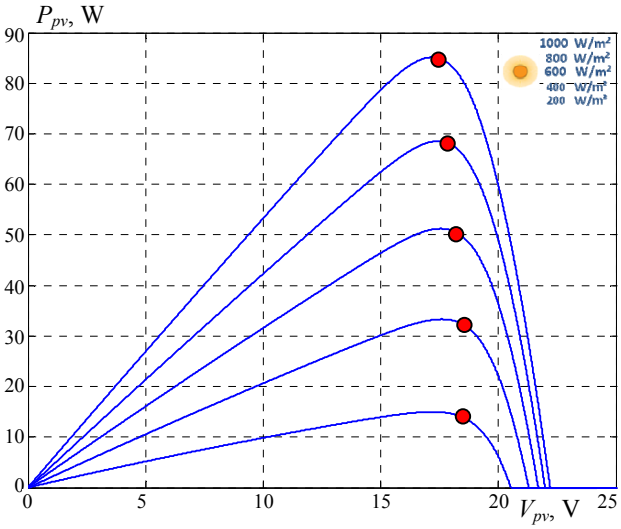

Fig. 4. Characteristics $P = f(V)$ of the PV panel under irradiation variation

Buck converter modeling. The load is connected to the DC bus via a DC-DC buck power converter [33] (Fig. 5), which allows it to be controlled.

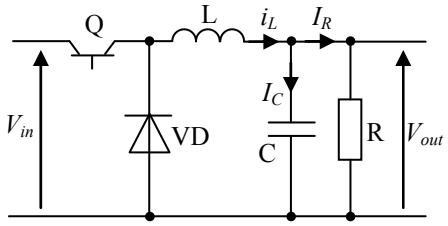

Fig. 5. Buck converter

To model the converter, state space average equations are employed, as shown in the equation (2) [34]

$$\begin{cases} \dot{x}_1 = k_1 u V_{in} - k_1 x_2; \\ \dot{x}_2 = k_2 x_1 - k_3 x_2, \end{cases} \quad (2)$$

where u is duty cycle and $k_1 = 1/L$; $k_2 = 1/C$; $k_3 = 1/RC$.

The steady state is given by

$$[x_1 \quad x_2] = [i_L \quad V_{out}]. \quad (3)$$

• **The DC/AC inverter model.** Figure 6 presents the structure of three-phase voltage source inverter (VSI).

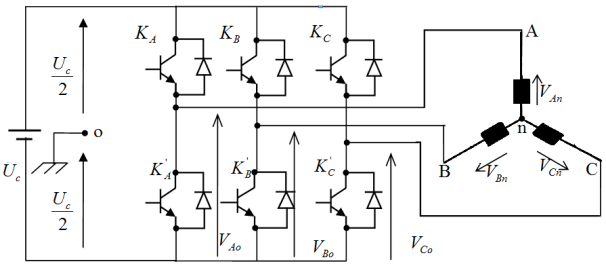

Fig. 6. Structure of a three-phase VSI

The switching function is $C_i\{i = A, B, C\}$ as bellow[35]:

- if $C_i = 1$, then K_i is OFF and K'_i is ON;
- if $C_i = 0$, then K_i is ON and K'_i is OFF.

The outputs voltage of the inverter U_{AB}, U_{BC}, U_{CA} can be write as:

$$\begin{cases} U_{AB} = U_{Ao} - U_{Bo}; \\ U_{BC} = U_{Bo} - U_{Co}; \\ U_{CA} = U_{Co} - U_{Ao}. \end{cases} \quad (4)$$

Since the phase voltages are star-connected to load sum to zero, equation (4) can be written:

$$\begin{cases} U_{An} = \frac{1}{3}\left[U_{AB} - U_{CA}\right]; \\ U_{Bn} = \frac{1}{3}\left[U_{BC} - U_{AB}\right]; \\ U_{Cn} = \frac{1}{3}\left[U_{CA} - U_{BC}\right] \end{cases} \quad (5)$$

For the phase-to-neutral voltages of a star-connected load obtain this model:

$$\begin{cases} U_{An} + U_{no} = U_{Ao}; \\ U_{Bn} + U_{no} = U_{Bo}; \\ U_{Cn} + U_{no} = U_{Co}. \end{cases} \quad (6)$$

and we conclude that:

$$U_{no} = \frac{1}{3}\left(U_{Ao} + U_{Bo} + U_{Co}\right). \quad (7)$$

For ideal switching can be obtained:

$$U_{io} = C_i \cdot U_c - U_c/2, \quad (8)$$

with

$$\begin{cases} U_{Ao} = (C_A - 0{,}5)U_C; \\ U_{Bo} = (C_B - 0{,}5)U_C; \\ U_{Co} = (C_C - 0{,}5)U_C. \end{cases} \quad (9)$$

Substitution of (6) into (7) obtain [30]:

$$\begin{cases} U_{An} = \frac{2}{3}U_{Ao} - \frac{1}{3}U_{Bo} - \frac{1}{3}U_{Co}; \\ U_{Bn} = -\frac{1}{3}U_{Ao} + \frac{2}{3}U_{Bo} - \frac{1}{3}U_{Co}; \\ U_{Cn} = -\frac{1}{3}U_{Ao} - \frac{1}{3}U_{Bo} + \frac{2}{3}U_{Co}. \end{cases} \quad (10)$$

Setting (9) with (10), obtain:

$$\begin{bmatrix} U_{An} \\ U_{Bn} \\ U_{Cn} \end{bmatrix} = \frac{1}{3} \cdot U_C \begin{bmatrix} 2 & -1 & -1 \\ -1 & 2 & -1 \\ -1 & -1 & 2 \end{bmatrix} \begin{bmatrix} C_A \\ C_B \\ C_C \end{bmatrix}. \quad (11)$$

The Conventional P&O Algorithm (CPOA). In the P&O process the voltage is increased or decreased with a defined step size in the direction of reaching the MPP. The method is carried out again and again till the MPP is attained. In steady condition the operational point oscillates about the MPP, the oscillation is highly dependent on step size, so that when using a small step size, it can reduce volatility but can reduce system dynamics as well. On the other hand, while using a large step size it can improve system dynamics, but it can increase volatility around MPP as well [36]. Figure 7 illustrates the flowchart of the CPOA algorithm.

AMPO-ANN algorithm. Many MPPT approaches have recently been created and developed. In terms of accuracy, for real time implementation the P&O MPPT method is more practical than other MPPTs because it is easier to implement [38]. The P&O MPPT technique is primarily based on the perturbation of the PV output voltage $V(t)$ and related output power $P(t)$, which is compared to the prior perturbation $P(t+1)$. Keep the next voltage shift in the same direction as the previous one if the power increases.

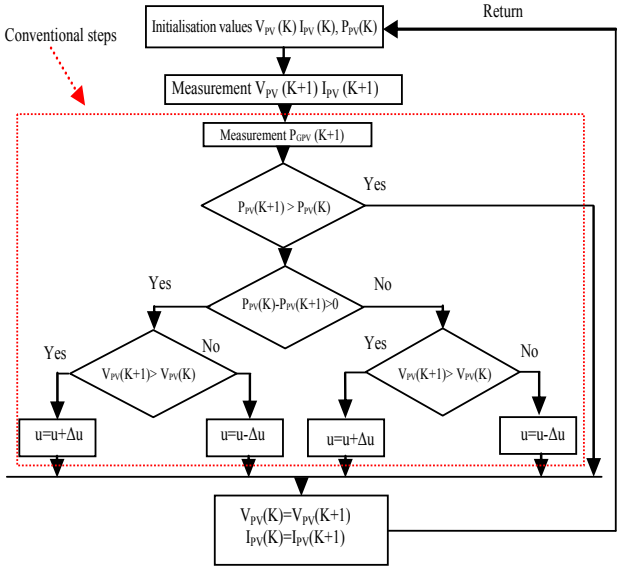

Fig.7. Flowchart of the CPOA algorithm

Artificial intelligence is used in many areas of research, and ANN is a bright and promising part of these technologies, where process control and monitoring, recognition of patterns, power electronics, finance and economics, and medical diagnosis are only a few of the applications where ANNs have proven their worth [37].

In this paper, we will use two neural networks at the same time; the first network whose role is to estimate the output current which corresponds to the maximum power, and the second is used to estimate the voltage which corresponds to the maximum power too[28].

However, if the steps of the algorithm are tracking speed has been increased, as has the accuracy. and rapidity are increased ($dP_{pv}/dV_{pv}>0$), but with high increasing in the oscillation, resulting in comparatively low performance and vice versa, In this paper, an AMPO algorithm method is dedicated to find a simple implantation in comparison with classical CPOA algorithm, and the AMPO can be written as follows:

$$u(\gamma) = U_c(\gamma - 1) + \gamma \cdot \text{sign}(\Delta P), \quad (12)$$

where γ is fixed step and U_c is the voltage control;

$$\Delta P = P(\gamma) - P(\gamma - 1),$$

if $\Delta P > 0$ then increase U_c, else $\Delta P < 0$ decrease U_c.

A power of the panel (P_{pv}) sensor is connected to the P&O algorithm unit in order to detect the power in state γ and compare it with next value (γ+1). At a certain point, when the difference between $P_{pv}(\gamma)$ and $P_{pv}(\gamma+1)$ is ΔP_{pv} then the algorithm will recognize that there is a powerful change and the algorithm should start from the beginning (γ). The value of $u(\gamma)$ (u is voltage control of P&O) is set to depend on the value of γ of the ΔP_{pv} criteria and it is different from irradiation values of PV, the $\Delta P_{pv}/\Delta V_{pv}$ change value around at point MPP, the duty cycle follows this change, view the duty cycle varying between values positive, zeros, negative.

In this article, we replace this variation of power $u(\gamma+1)$ show in equation (12) by function sign(P_{pv}) play the role of conventional step of algorithm P&O, with rapidly responses, equation (13) can be written in the following form:

$$\text{sign}(P_{pv}) = \begin{cases} 1 & if \quad P_{pv} > 0; \\ 0 & if \quad P_{pv} = 0; \\ -1 & if \quad P_{pv} < 0; \end{cases} \quad (13)$$

The adding the variation of power (ΔP_{pv}) and voltage (ΔV_{pv}) can be whiten equation (13) as follow:

$$\text{sign}(\Delta P_{pv}/\Delta V_{pv}) = \begin{cases} 1 & if \quad \Delta P_{pv}/\Delta V_{pv} > 0; \\ 0 & if \quad \Delta P_{pv}/\Delta V_{pv} = 0 \text{ at MPP}; \\ -1 & if \quad \Delta P_{pv}/\Delta V_{pv} < 0. \end{cases} \quad (14)$$

Equation (14) can be written as follow:

$$\delta = \text{sign}\{(P_{pv}(\gamma) - P_{pv}(\gamma+1)) \cdot (V_{pv}(\gamma) - V_{pv}(\gamma+1))\}. \quad (15)$$

To simplify the writing of equation (15) can be written in the following form:

$$\delta = \text{sign}(\Delta P_{pv} \cdot \Delta V_{pv}). \quad (16)$$

State of the voltage control δ of AMPO can be summarized in Table 1.

Table 1

Variation of MPP in algorithm

sign($\Delta P_{pv}(\gamma)$)	sign($\Delta P_{pv}(\gamma+1)$)	δ	u duty cycle	State of MPOA
–1	–1	–2	+1	Left MPP
–1	+1	0	0	at MPP
+1	–1	0	0	at MPP
+1	+1	+2	+1	Right MPP

The Table 1 presented the variation of MPP point in algorithm by 4 cases:

- **Case 1**. If state of changing algorithm is sign($\Delta P_{pv}(\gamma)$) = –1, then sign($\Delta P_{pv}(\gamma+1)$) = –1, and δ = –2, the MPP moving to left; there for u = +1, to increase power of PV (P_{pv}).
- **Case 2**. If state of changing algorithm is sign($\Delta P_{pv}(\gamma)$) = +1, then sign($\Delta P_{pv}(\gamma+1)$) = –1, and δ = 0, at point MPP; there for u = 0, no changing in the power of PV (P_{pv}).
- **Case 3**. If state of changing algorithm is sign($\Delta P_{pv}(\gamma)$) = –1, then sign($\Delta P_{pv}(\gamma+1)$) = +1, and δ = 0, at point MPP; there for u = 0, no changing in the power of PV (P_{pv}).
- **Case 4**. If state of changing algorithm is sign($\Delta P_{pv}(\gamma)$) = +1, then sign($\Delta P_{pv}(\gamma+1)$) = +1, and δ = +2, the MPP moving to right; there for u = +1, to decrease power of PV (P_{pv}).

After this case the variation of δ and u can be thought in AMPO-ANN for desired voltage regulation (for regulate the desire voltage), as shown in Fig. 8.

The value of δ presented the variation of power of panel ΔP_{pv} we can add to value of duty cycle u for adjust at point MPP can be written as follow:

$$u(\gamma) = u(\gamma) + \delta \cdot u(\gamma + 1). \quad (16)$$

After equations (15) – (17) can be designing the flow chart of the MPOA algorithm modified shown in Fig. 8 and presented a new step has determined by previous equation.

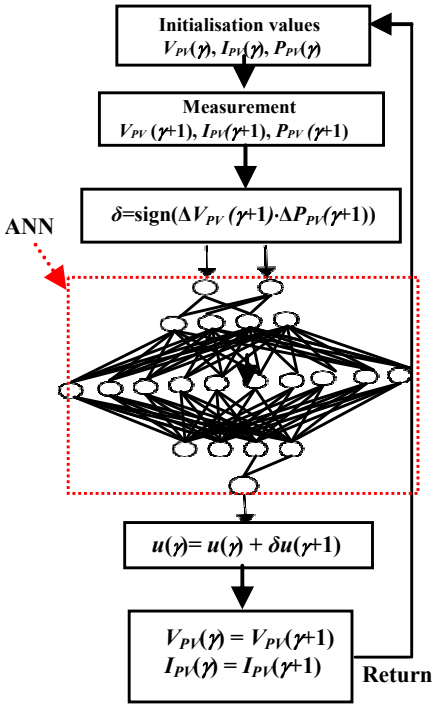

Fig.8. Flowchart of the adaptive ANN-AMPO

Simulation of proposed system. The simulation of the Intelligent Maximum Power Point Tracking (IMPPT) based on AMPO-ANN makes it possible to verify that neural networks approach, after learning is effectively capable of predicting the desired output for the values of the data at the input which are not used during learning. We should always compare the true exit from the trajectory of neural networks with the trajectory of the model of PV cells.

The simulations results given in Fig. 9 and represent the electrical characteristics of the stand-alone PV system controlled by AMPO-ANN under standard climatic conditions (1000 W/m² and 25 °C). The powers obtained from the proposed technique stabilize in a steady state around the optimal values delivered by PV (P_{mpp} = 111 W, V_{mpp} = 26 V and I_{mpp} = 4.4 A); AMPO controller allows us for parts per million (PPM) to be attained in 0.06 s, whilst the ANN algorithm allows for PPM to be obtained in 0.02 s only. In addition Fig. 9 shows that in steady state the maximum power supplied by the PV system controlled by the AMPO-ANN is more stable and closer to the PPM compared to AMPO control; the AMPO control give a power oscillates around the MPP which resulting in power losses.

From Fig. 9,*a* we observe that P_{pv} takes 0.02 s in transient state to stabilize at a steady – state value which is MPP in the neighborhood of 111 W.

Figure 9,*b* summarizes a comparison between the MPPT of PV output power controlled by AMPO and AMPO-ANN. We see that the power generalized based on AMPO algorithm has more pikes and is more oscillate compared to the improved technique based on ANN.

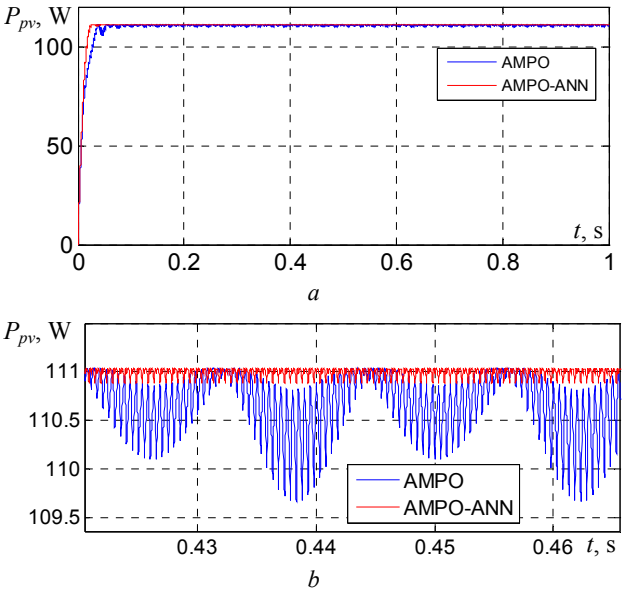

Fig. 9. *a* – power of PV (AMPO-ANN);
b – zoom power of PV (AMPO-ANN)

From Fig. 10 we observe the during the period from 0 s to 0.05 s the voltage decreases with significant oscillations, then it stabilizes at the maximum value 26 V.

Figure 11 shows the load current curve based on AMPO-ANN techniques, we note that its value in steady state stabilizes around 4.4 A.

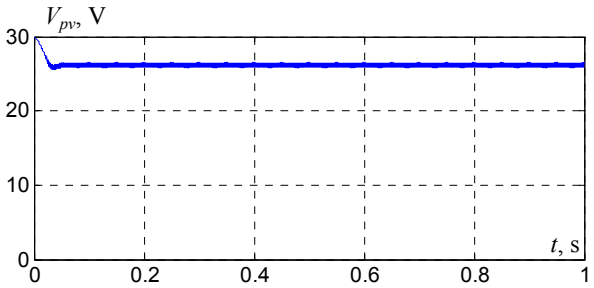

Fig. 10. Voltage of PV (AMPO-ANN)

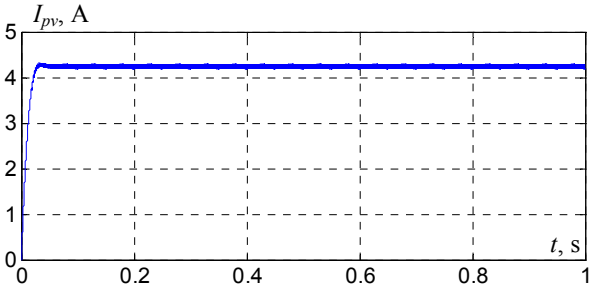

Fig. 11. Current of PV (AMPO-ANN)

In order to verify the robustness and the reliability of the proposed method, we will test the performance of AMPO-ANN by performing separately under climate condition variation, we make variations on solar irradiation and we assume that the temperature is a constant equal to 25 °C, where we suppose that the irradiation drops from 500 to 1000 W/m^2, at 0.5 s.

According Fig. 12 we note that the maximum power delivered by the PV varies proportionally with irradiation. When the irradiation is 500 W the P_{pv} stabilizes around 38 W. But when the sun goes from 500 to 1000 W/m² the P_{pv} rises to 111 W.

In addition, the simulation result presented by Fig. 9, shows that the AMPO-ANN represent better performances compared to AMPO; since they converge quickly towards the new P_{mpp} with reduced the chattering. Figures 13, 14 show current and voltage of PV based on AMPO-ANN techniques respectively.

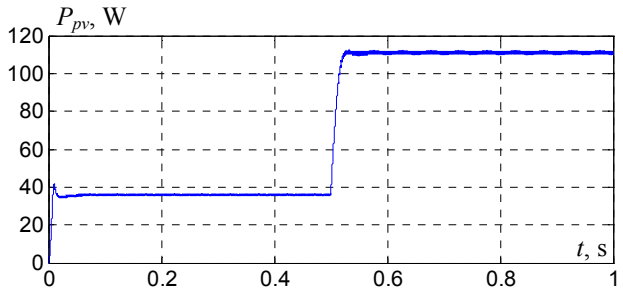

Fig. 12. Power of PV (AMPO-ANN)

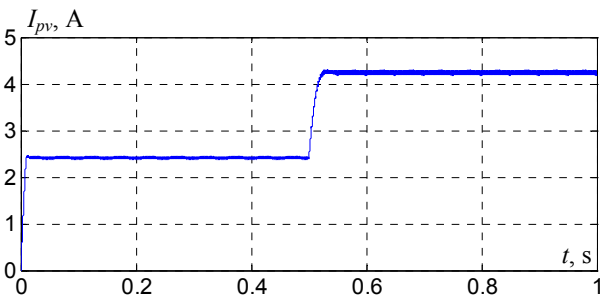

Fig. 13. Current of PV (AMPO-ANN)

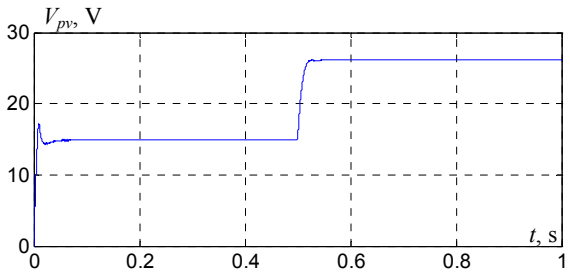

Fig. 14. Voltage of PV (AMPO-ANN)

We will test the performances of the AMPO-ANN algorithm previously developed with the purpose of the grid connection and the climatic conditions are fixed in standard conditions, then connect the PV system to the electrical networks. Figure 15 shows the simulation results. We observe better results for I_{mes} (current measured by the network), I_{ch} (load current) also the three-phase currents I_a, I_b, I_c (Fig. 16).

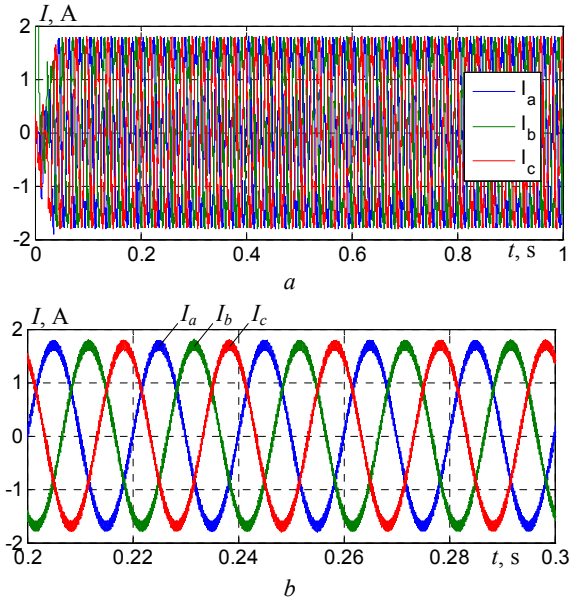

Fig. 15. *a* – three-phase currents (AMPO-ANN); *b* – zoom three-phase currents (AMPO-ANN).

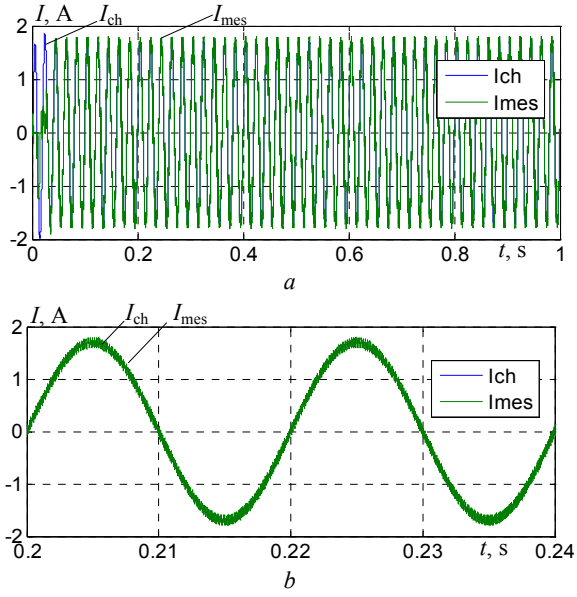

Fig. 16. *a* – current I_{ch} and I_{mes} (AMPO-ANN); *b* – zoom current I_{ch} and I_{mes} (AMPO-ANN)

The results confirm the correct functioning of the two controllers AMPO and AMPO-ANN, but also show a better functioning of the AMPO-ANN. The latter has proven to have better performance, fast response time and very low, steady state error, and it is robust to variations in atmospheric conditions.

Experimental results. The proposed AMPO-ANN controller has been put to the test in order to improve its performance. Instead of a solar panel, an experimental setup of a system made of a PV emulator coupled to a DC-DC converter is shown in Fig. 17. LA-25NP and LV-25P are sensors of the current I_{pv} and voltage V_{pv}. The proposed control is implemented on the dSPACE DS1104.

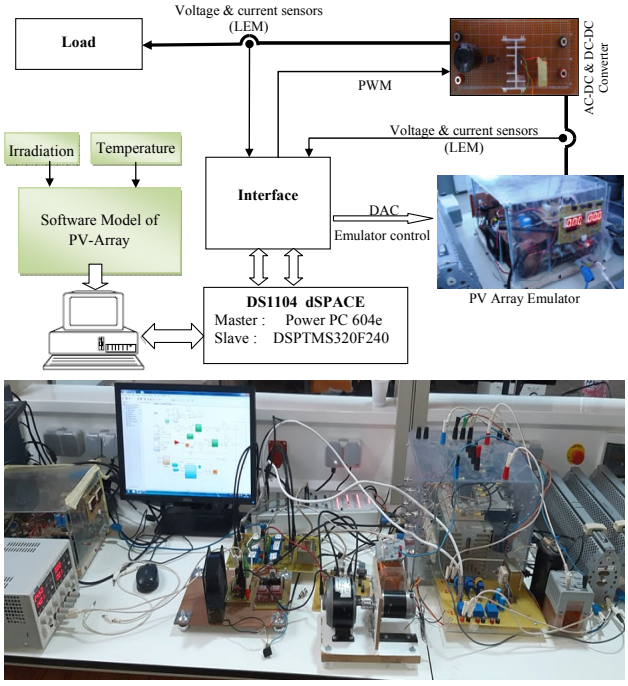

Fig. 17. Structure of the laboratory setup

In the simulation part we assume that all components are perfect (simplifying assumptions, losses and switching phenomena are ignored), so the DC-DC & AC-DC converters has an almost perfect operation.

On the other hand, the tests which we carried out in the laboratory take into account the saturation of the used components and the switching phenomena, these tests consist to validating the proposed technique which applied to a DC-DC converter then connected to an AC-DC converter (inverter).

From Fig. 18-20 we observe that P_{pv} takes 0 s in transient state to stabilize at a steady – state value which is MPP in the neighborhood of 100 W, current and voltage also taken point MPP at values 3.4 A and 29 V.

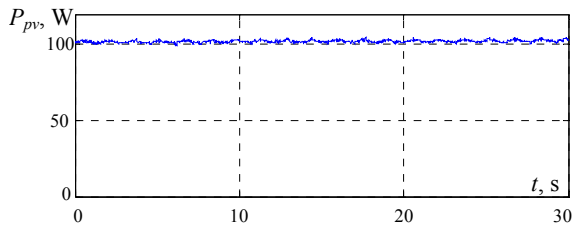

Fig. 18. Power of PV (AMPO-ANN)

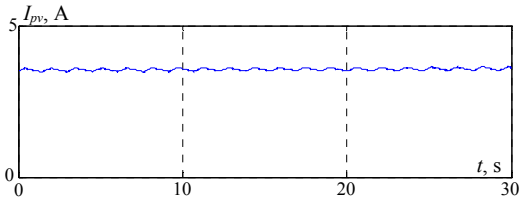

Fig. 19. Current of PV (AMPO-ANN)

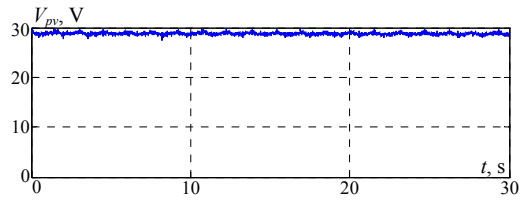

Fig. 20. Voltage of PV (AMPO-ANN)

We will test the performances of the AMPO-ANN algorithm previously developed with the purpose of the grid connection and the climatic conditions are fixed in standard conditions, then connect the PV system to the electrical networks. Figures 21, 22 show the experimental results. We observe better results for I (current measured by the network), V_{AC} (load voltage), also single phase of current and voltage.

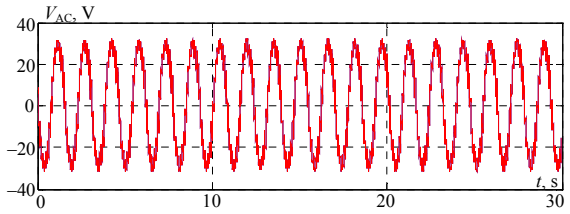

Fig. 21. Voltage of AC bus (AMPO-ANN)

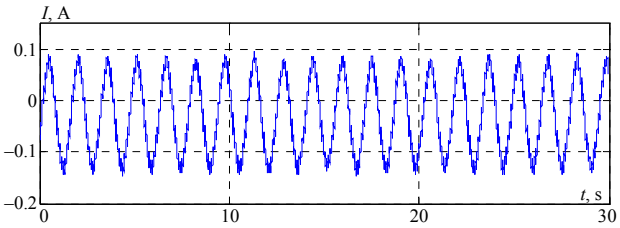

Fig. 22. Current of AC bus (AMPO-ANN)

The Figures 23-27 show the results of realizing the output power of the PV, its operating voltage and current, and the duty cycle (at the frequency of 3000 Hz) for the AMPO-ANN and the conventional disturbance and observation (P&O) AMPO-ANN using a converter and inverter environmental conditions. It is clearly seen how the AMPO-ANN algorithm reduces the response time of the PV system. Obviously, the system with AMPO has a great loss of energy in the transient state, that when the increase in power is the result of the increase in illumination in sinusoidal form between 500 W/m^2 and 1000 W/m^2, the reversal of the direction of illumination produced by the AMPO-ANN algorithm causes the increase of the power at the MPP point to 101 W and at the same time the output voltage of the inverter, the output voltage V_{AC} is 28 V and current at 0.15 A are illuminate also the harmonics in grid connected, the MPP starts close to the operating point, but the P&O algorithm detects that and moves the operating point in the right

direction. The AMPO-ANN algorithm gives a better result than the classic algorithm AMPO.

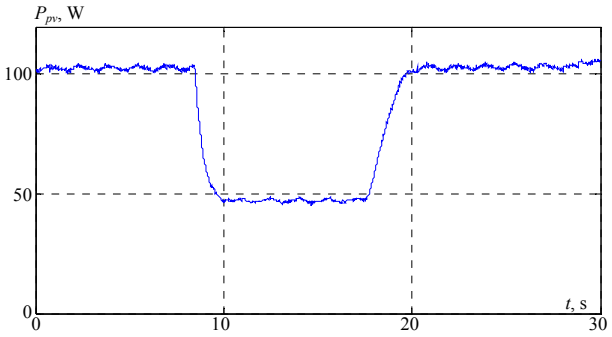

Fig. 23. Power of PV (AMPO-ANN)

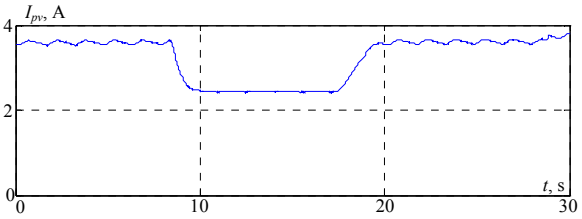

Fig. 24. Current of PV (AMPO-ANN)

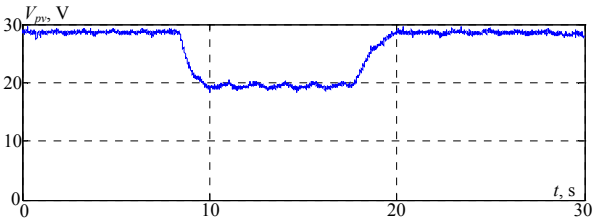

Fig. 25.Voltage of PV (AMPO-ANN)

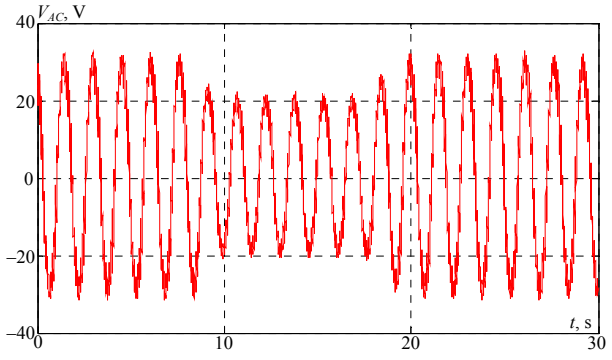

Fig. 26. Voltage of AC bus (AMPO-ANN)

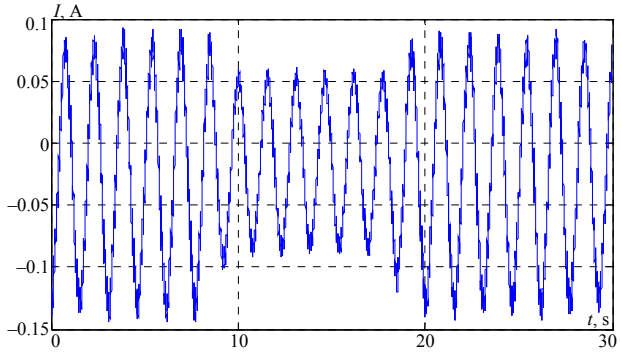

Fig. 27. Current of AC bus (AMPO-ANN)

Conclusions.

We analyzed the electrical functioning of a photovoltaic system, adapted by DC-DC converter, regulated by an maximum power point tracking command, to control maximum power point tracking of a photovoltaic system based on neural networks were presented and its architecture of neural networks was used. The simulation and validation results show that this system can adapt the maximum operating point for variations in external disturbances.

We can say that artificial neural networks are efficient and powerful modeling tools, their robustness lies in the possibility of predicting the output of the network even if the relationship with the input is not linear.

The purpose of the modified algorithm adaptive modified perturbation and observation – artificial neural network is to reduce oscillation and achieve a high response of the output power in response to changing weather conditions and parameter variations. All of the results show that the proposed technique control and our improved maximum power point tracking approach are effective.

Funding. This work was supported by the Franco-Algerian cooperation program PHC-Maghreb.

Acknowledgement. The authors would like to thank laboratory teams of research Propulsion Systems – Electromagnetic Induction, LSPIE, University of Batna 2, Batna, Algeria.

Conflict of interest. The authors declare that they have no conflicts of interest.

REFERENCES

1. International Energy Agency. Global Energy & CO2 Status Report 2019. Available at: https://www.iea.org/reports/global-energy-co2-status-report-2019 (accessed 25 May 2021).

2. Wisnubroto D.S., Zamroni H., Sumarbagiono R., Nurliati G. Challenges of implementing the policy and strategy for management of radioactive waste and nuclear spent fuel in Indonesia. *Nuclear Engineering and Technology*, 2021, vol. 53, no. 2, pp. 549-561. doi: https://doi.org/10.1016/j.net.2020.07.005.

3. Zhou W., Ibano K., Qian X. Construction of an East Asia Nuclear Security System. In: Zhou W., Qian X., Nakagami K. (eds) *East Asian Low-Carbon Community*. Springer, Singapore, 2021, pp. 199-214. doi: https://doi.org/10.1007/978-981-33-4339-9_11.

4. Rahman F.A., Aziz M.M.A., Saidur R., Bakar W.A.W.A., Hainin M.R., Putrajaya R., Hassan N.A. Pollution to solution: Capture and sequestration of carbon dioxide (CO_2) and its utilization as a renewable energy source for a sustainable future. *Renewable and Sustainable Energy Reviews*, 2017, vol. 71, pp. 112-126. doi: https://doi.org/10.1016/j.rser.2017.01.011.

5. Al-Maamary H.M.S., Kazem H.A., Chaichan M.T. The impact of oil price fluctuations on common renewable energies in GCC countries. *Renewable and Sustainable Energy Reviews*, 2017, vol. 75, pp. 989-1007. doi: https://doi.org/10.1016/j.rser.2016.11.079.

6. Ahmadlouydarab M., Ebadolahzadeh M., Muhammad Ali H. Effects of utilizing nanofluid as working fluid in a lab-scale designed FPSC to improve thermal absorption and efficiency. *Physica A: Statistical Mechanics and its Applications*, 2020, vol. 540, p. 123109 .doi: https://doi.org/10.1016/j.physa.2019.123109.

7. Abbassi A., Abbassi R., Heidari A.A., Oliva D., Chen H., Habib A., Jemli M., Wang M. Parameters identification of photovoltaic cell models using enhanced exploratory salp chains-based approach. *Energy*, 2020, vol. 198, p. 117333. doi: https://doi.org/10.1016/j.energy.2020.117333.

8. Sivakumar L.P., Sivakumar S., Prabha A., Rajapandiyan A. Implementation of particle swarm optimization for maximum power absorption from photovoltaic system using energy extraction circuit. *2019 IEEE International Conference on Intelligent Techniques in Control, Optimization and Signal Processing (INCOS)*, 2019, pp. 1-4. doi: https://doi.org/10.1109/incos45849.2019.8951378.
9. Ramos-Hernanz J., Uriarte I., Lopez-Guede J.M., Fernandez-Gamiz U., Mesanza A., Zulueta E. Temperature based maximum power point tracking for photovoltaic modules. *Scientific Reports*, 2020, vol. 10, no. 1, p. 12476. doi: https://doi.org/10.1038/s41598-020-69365-5.
10. De Brito M.A.G., Galotto L., Sampaio L.P., E Melo G.D.A., Canesin C.A. Evaluation of the main MPPT techniques for photovoltaic applications. *IEEE Transactions on Industrial Electronics*, 2013, vol. 60, no. 3, pp. 1156-1167. doi: https://doi.org/10.1109/tie.2012.2198036.
11. Motahhir S., El Hammoumi A., El Ghzizal A. The most used MPPT algorithms: Review and the suitable low-cost embedded board for each algorithm. *Journal of Cleaner Production*, 2020, vol. 246, p. 118983. doi: https://doi.org/10.1016/j.jclepro.2019.118983.
12. Charin C., Ishak D., Mohd Zainuri M.A.A. A maximum power point tracking based on levy flight optimization. *International Journal of Power Electronics and Drive Systems*, 2020, vol. 11, no. 3, p. 1499. doi: https://doi.org/10.11591/ijpeds.v11.i3.pp1499-1507.
13. Rezkallah M., Hamadi A., Chandra A., Singh B. Design and implementation of active power control with improved P&O Method for wind-PV-battery-based standalone generation system. *IEEE Transactions on Industrial Electronics*, 2018, vol. 65, no. 7, pp. 5590-5600. doi: https://doi.org/10.1109/tie.2017.2777404.
14. Nebti K., Lebied R. Fuzzy maximum power point tracking compared to sliding mode technique for photovoltaic systems based on DC-DC boost converter. *Electrical Engineering & Electromechanics*, 2021, no. 1, pp. 67-73. doi: https://doi.org/10.20998/2074-272x.2021.1.10.
15. Algazar M.M., Al-Monier H., El-Halim H.A., Salem M.E.E.K. Maximum power point tracking using fuzzy logic control. *International Journal of Electrical Power & Energy Systems*, 2012, vol. 39, no. 1, pp. 21-28. doi: https://doi.org/10.1016/j.ijepes.2011.12.006.
16. Fares D., Fathi M., Shams I., Mekhilef S. A novel global MPPT technique based on squirrel search algorithm for PV module under partial shading conditions. *Energy Conversion and Management*, 2021, vol. 230, p. 113773. doi: https://doi.org/10.1016/j.enconman.2020.113773.
17. Ishaque K., Salam Z., Amjad M., Mekhilef S. An improved particle swarm optimization (PSO)–based MPPT for PV with reduced steady-state oscillation. *IEEE Transactions on Power Electronics*, 2012, vol. 27, no. 8, pp. 3627-3638. doi: https://doi.org/10.1109/tpel.2012.2185713.
18. Bendib B., Krim F., Belmili H., Almi M.F., Bolouma S. An intelligent MPPT approach based on neural-network voltage estimator and fuzzy controller, applied to a stand-alone PV system. *2014 IEEE 23rd International Symposium on Industrial Electronics (ISIE)*, 2014, pp. 404-409. doi: https://doi.org/10.1109/isie.2014.6864647.
19. Messalti S., Harrag A., Loukriz A. A new variable step size neural networks MPPT controller: Review, simulation and hardware implementation. *Renewable and Sustainable Energy Reviews,* 2017, vol. 68, pp. 221-233. doi: https://doi.org/10.1109/isie.2014.6864647.
20. Motamarri R., Nagu B. GMPPT by using PSO based on Lévy flight for photovoltaic system under partial shading conditions. *IET Renewable Power Generation*, 2020, vol. 14, no. 7, pp. 1143-1155. doi: https://doi.org/10.1049/iet-rpg.2019.0959.
21. Motamarri R., Bhookya N. JAYA algorithm based on Lévy flight for global MPPT under partial shading in photovoltaic system. *IEEE Journal of Emerging and Selected Topics in Power Electronics*, 2021, vol. 9, no. 4, pp. 4979-4991. doi: https://doi.org/10.1109/jestpe.2020.3036405.
22. Charin C., Ishak D., Mohd Zainuri M.A.A., Ismail B., Mohd Jamil M.K. A hybrid of bio-inspired algorithm based on Levy flight and particle swarm optimizations for photovoltaic system under partial shading conditions. *Solar Energy*, 2021, vol. 217, pp. 1-14. doi: https://doi.org/10.1016/j.solener.2021.01.049.
23. Abo-Elyousr F.K., Abdelshafy A.M., Abdelaziz A.Y. MPPT-based particle swarm and cuckoo search algorithms for PV systems. *Green Energy and Technology*, 2020, pp. 379-400. doi: https://doi.org/10.1007/978-3-030-05578-3_14.
24. Mohd Adnan M.R.H., Sarkheyli A., Mohd Zain A., Haron H. Fuzzy logic for modeling machining process: a review. *Artificial Intelligence Review*, 2015, vol. 43, no. 3, pp. 345-379. doi: https://doi.org/10.1007/s10462-012-9381-8.
25. Abo-Sennah M.A., El-Dabah M.A., Mansour A.E.-B. Maximum power point tracking techniques for photovoltaic systems: A comparative study. *International Journal of Electrical and Computer Engineering*, 2021, vol. 11, no. 1, p. 57-73. doi: https://doi.org/10.11591/ijece.v11i1.pp57-73.
26. Kumar N., Singh B., Panigrahi B.K. PNKLMF-based neural network control and learning-based HC MPPT technique for multiobjective grid integrated solar PV based distributed generating system. *IEEE Transactions on Industrial Informatics*, 2019, vol. 15, no. 6, pp. 3732-3742. doi: https://doi.org/10.1109/tii.2019.2901516.
27. Tavakoli A., Forouzanfar M. A self-constructing Lyapunov neural network controller to track global maximum power point in PV systems. *International Transactions on Electrical Energy Systems*, 2020, vol. 30, no. 6, pp. 1-15. doi: https://doi.org/10.1002/2050-7038.12391.
28. Sahraoui H., Chrifi-Alaoui L., Drid S., Bussy P. Second order sliding mode control of DC-DC converter used in the photovoltaic system according an adaptive MPPT. *International Journal of Renewable Energy Research*, 2016, vol. 6, no. 2, pp. 375-383. Available at: https://www.ijrer.org/ijrer/index.php/ijrer/article/view/3369/pdf (accessed 25 May 2021).
29. Slama F., Radjeai H., Mouassa S., Chouder A. New algorithm for energy dispatch scheduling of grid-connected solar photovoltaic system with battery storage system. *Electrical Engineering & Electromechanics*, 2021, no. 1, pp. 27-34. doi: https://doi.org/10.20998/2074-272x.2021.1.05.
30. Belbachir N., Zellagui M., Settoul S., El-Bayeh C.Z., Bekkouche B. Simultaneous optimal integration of photovoltaic distributed generation and battery energy storage system in active distribution network using chaotic grey wolf optimization. *Electrical Engineering & Electromechanics*, 2021, no. 3, pp. 52-61. doi: https://doi.org/10.20998/2074-272X.2021.3.09.
31. Shavelkin A.A., Gerlici J., Shvedchykova I.O., Kravchenko K., Kruhliak H.V. Management of power consumption in a photovoltaic system with a storage battery connected to the network with multi-zone electricity pricing to supply the local facility own needs. *Electrical Engineering & Electromechanics*, 2021, no. 2, pp. 36-42. doi: https://doi.org/10.20998/2074-272X.2021.2.06.
32. Jordehi A.R. Parameter estimation of solar photovoltaic (PV) cells: A review. *Renewable and Sustainable Energy Reviews*, 2016, vol. 61, pp. 354-371. doi: https://doi.org/10.1016/j.rser.2016.03.049.
33. Wei Z., Zhang B., Jiang Y. Analysis and modeling of fractional-order buck converter based on Riemann-Liouville derivative. *IEEE Access*, 2019, vol. 7, pp. 162768-162777. doi: https://doi.org/10.1109/access.2019.2952167.

34. Sahraoui H., Drid S., Chrifi-Alaoui L., Hamzaoui M. Voltage control of DC-DC buck converter using second order sliding mode control. *2015 3rd International Conference on Control, Engineering & Information Technology (CEIT)*, 2015, pp. 1-5. doi: https://doi.org/10.1109/ceit.2015.7233082.

35. Alnejaili T., Drid S., Mehdi D., Chrifi-Alaoui L., Belarbi R., Hamdouni A.. Dynamic control and advanced load management of a stand-alone hybrid renewable power system for remote housing. *Energy Conversion and Management*, 2015, vol. 105, pp. 377-392. doi: https://doi.org/10.1016/j.enconman.2015.07.080.

36. Ahmed J., Salam Z. An improved perturb and observe (P&O) maximum power point tracking (MPPT) algorithm for higher efficiency. *Applied Energy*, 2015, vol. 150, pp. 97-108. doi: https://doi.org/10.1016/j.apenergy.2015.04.006.

37. Bouchaoui L., Hemsas K.E., Mellah H., Benlahneche S. Power transformer faults diagnosis using undestructive methods (Roger and IEC) and artificial neural network for dissolved gas analysis applied on the functional transformer in the Algerian north-eastern: a comparative study. *Electrical Engineering & Electromechanics*, 2021, no. 4, pp. 3-11. doi: https://doi.org/10.20998/2074-272X.2021.4.01.

Received 17.07.2021
Accepted 05.09.2021
Published 26.10.2021

Hamza Sahraoui[1,3], *Doctor of Engineering*,
Hacene Mellah[2], *Doctor of Engineering*,
Said Drid[3], *Professor, Dr.-Ing. of Engineering*,
Larbi Chrifi-Alaoui[4], *Dr.-Ing. of Engineering*,
[1] Electrical Engineering Department,
Hassiba Benbouali University of Chlef,
B.P 78C, Ouled Fares Chlef 02180, Chlef, Algeria,
e-mail: hamzasahraoui@gmail.com
[2] Electrical Engineering Department,
University Akli Mouhand Oulhadj-Bouira,
Rue Drissi Yahia Bouira, 10000, Algeria,
e-mail: has.mel@gmail.com (Corresponding author)
[3] Research Laboratory LSPIE,
Electrical Engineering Department,
University of Batna 2,
53, Route de Constantine, Fésdis, Batna 05078, Algeria,
e-mail: saiddrid@ieee.org
[4] Laboratoire des Technologies Innovantes (LTI),
University of Picardie Jules Verne, IUT de l'Aisne,
13 Avenue François Mitterrand 02880 Cuffies-Soissons, France,
e-mail: larbi.alaoui@u-picardie.fr

How to cite this article:
Sahraoui H., Mellah H., Drid S., Chrifi-Alaoui L. Adaptive maximum power point tracking using neural networks for a photovoltaic systems according grid. *Electrical Engineering & Electromechanics*, 2021, no. 5, pp. 57-66. doi: https://doi.org/10.20998/2074-272X.2021.5.08.

UDC 621.316.9 https://doi.org/10.20998/2074-272X.2021.5.09

D.G. Koliushko, S.S. Rudenko, A.N. Saliba

METHOD OF INTEGRO-DIFFERENTIAL EQUATIONS FOR INTERPRETING THE RESULTS OF VERTICAL ELECTRICAL SOUNDING OF THE SOIL

The paper is devoted to ***the problem*** *of determining the geoelectric structure of the soil within the procedure of testing the grounding arrangements of existing power plants and substations to the required depth in conditions of dense development. To solve the problem, it was proposed to use the Schlumbergers method , which has a greater sounding depth compared to the Wenner electrode array.* ***The purpose*** *of the work is to develop a mathematical model for interpreting the results of soil sounding by the Schlumberger method in the form of a four-layer geoelectric structure.* ***Methodology****. To construct a mathematical model, it is proposed to use the solution of a particular problem about the field of a point current source, which, like the observation point, is located in the first layer of a four-layer soil. Based on this expressions, a system of linear algebraic equations of the 7-th order with respect to the unknown coefficients a_i and b_i was compiled. On the basis of its analytical solution, an expression for the potential of the electric field was obtained for conducting VES (the point current source and the observation point are located only on the soil surface).* ***Results****. Comparison of the results of soil sounding by the Schlumberger installation and the interpretation of its results for the same points shows a sufficient degree of approximation: the maximum relative error does not exceed 9.7 % (for the second point), and the average relative error is 3.6 %.* ***Originality****. Based on the obtained expression, a test version of the program was implemented in Visual Basic for Applications to interpret the results of VES by the Schlumberger method. To check the obtained expressions, the interpretation of the VES results was carried out on the territory of a 150 kV substation of one of the mining and processing plants in the city of Kriviy Rih.* ***Practical significance.*** *The developed mathematical model will make it possible to increase the sounding depth, and, consequently, the accuracy of determining the standardized parameters of the grounding arrangements of power stations and substations.* References 13, figures 3.

Key words: **electrical substation, grounding arrangements, vertical electrical sounding, Schlumberger method, method of integro-differential equations.**

Робота присвячена проблематиці визначення геоелектричної структури ґрунту в межах випробування заземлювальних пристроїв діючих електричних станцій та підстанцій на необхідну глибину в умовах щільної забудови. Для вирішення проблеми запропоновано використати установку Шлюмберже, яка має більшу глибину зондування у порівнянні з установкою Веннера. За допомогою методів інтегро-диференційних рівнянь було отримано аналітичні вирази для інтерпретації результатів зондування ґрунту установкою Шлюмберже у випадку чотиришарового ґрунту. Для перевірки отриманих виразів була проведена інтерпретація результатів вертикального електричного зондування на території підстанції 150 кВ одного з гірничо-збагачувальних комбінатів: максимальна відносна похибка не перевищує 9,7 %, а середня – 3,6 %. Бібл. 13, рис. 3.

Ключові слова: **електрична підстанція, заземлювальний пристрій, вертикальне електричне зондування, установка Шлюмберже, метод інтегро-диференційних рівнянь.**

Formulation of the problem. The procedure for determining the soil resistivity as a component of testing of the grounding arrangement (GA) for power stations and substations is regulated in the IEEE standards [1, 2]. In this case, it is recommended to use the Wenner installation for conducting vertical electrical sounding (VES) of the soil. Although, in the general case, the soil is a multilayer structure with many anisotropic inclusions, the expressions to interpret VES curves in the form of a two-layer geoelectric space with plane-parallel interfaces between layers are mainly used. The quality of VES and the interpretation of its results significantly affect the accuracy of calculating the parameters of GA, and, consequently, on the electrical safety of personnel and the reliability of the substation equipment.

VES is carried out by injecting a test current by a generator between current electrodes A and B and measuring the voltage drop at a certain area of the soil surface at potential electrodes M and N. The value of the apparent resistivity is equal to the product of the ratio of the measured voltage and current by the geometric factor of the installation [3]:

$$\rho_k = \frac{U}{I}k, \qquad (1)$$

where U is the voltage drop across the potential electrodes M and N (see Fig. 1); I is the current flowing through the current electrodes A and B; k is the geometrical coefficient of installation. For the Wenner installation, $k = 2\pi L$, where L – distance between the electrodes.

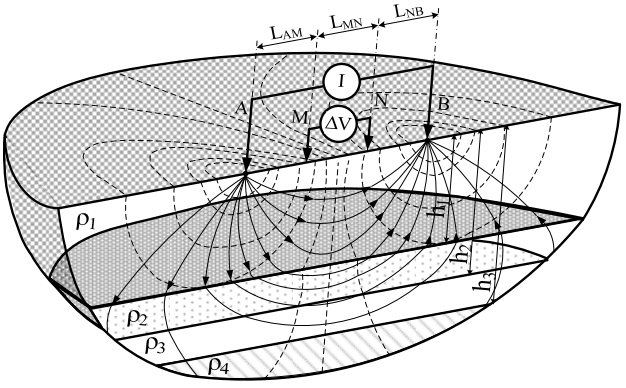

Fig. 1. The principle of conducting VES

The ratio of the spacing lengths of the current and potential electrodes depends on the choice of the VES installation, and the maximum distance between the current electrodes is determined by the required sounding depth. For the Wenner installation, the sounding depth is equal to 1/3 of the spacing length of the current electrodes [3]. Its advantages include:

- poor sensitivity to profile inclusions;
- direct relationship between electrode spacing and sounding depth;

• relatively simple expressions for calculating the apparent resistivity due to the equality of the interelectrode spacing between the current and potential electrodes.

In [4], based on the analysis of the experimental VES curves in the locations of more than 600 energy objects in Ukraine, it was shown that the vast majority of soils at the locations of power stations and substations have a three-layer structure (72,7 %), and another part (19 %) has more than three layers (usually four). Therefore, it is relevant to use interpretation tools with at least four layers, this will cover more than 90 % of energy objects in Ukraine. The authors in [5] based on the solution of the basic problem of the field of a point current source in a four-layer conducting half-space, expressions were obtained for interpreting the results of soil sounding by the Wenner installation. However, carrying out of VES for operating substations, as a rule, has to be performed in conditions of dense industrial or urban development, which does not allow providing the required sounding depth, which is several times greater than the largest diagonal of the GA [6]. Analysis of the literature shows that in the world, as a rule, models for the interpretation of VES curves built on numerical methods [7, 8] or using the method of images model [9] have found application. It was shown in [10] that the calculation error using such models can reach 20 %.

One of the ways to increase the sounding depth while maintaining the spacing of the current electrodes can be the use of a symmetric Schlumberger installation, which is a common case of the Wenner installation. However, a significant drawback is the lack of analytical expressions for interpreting the sounding results.

The purpose of the work is to develop a mathematical model for interpreting the results of soil sounding by the Schlumberger method in the form of a four-layer geoelectric structure.

Research materials. Interpretation of VES results is an inverse problem of electrical prospecting and, in the general case, is an ill-posed problem with many existing solutions that differ from the true one [5]. In this case, the relationship between the measured values of the apparent resistivity and the parameters of this model is expressed by integral equations.

To construct a mathematical model, it is proposed to use the solution of a particular problem about the field of a point current source, which, like the observation point, is located in the first layer of a four-layer soil [5]. When solving the problem, the following assumptions were made: the current does not pass through the boundary of the earth and the atmosphere, the interfaces between the layers are plane-parallel, and within each of them the electrical resistivity ρ_i is uniform. It was assumed that a point current source j is located in the first layer of a four-layer conducting half-space with plane-parallel interfaces (see Fig. 2). The electrical resistances of the first, second, third and fourth layers are denoted by ρ_1, ρ_2, ρ_3 and ρ_4, respectively. The depths of the interfaces of the first and second layers – h_1, the second and third – h_2, the third and fourth – h_3.

The formulation of the problem under consideration consists of the Laplace equation and additional conditions. The electric field of a point current source in a four-layer medium has axial symmetry, and the potential does not depend on the ψ-coordinate; therefore, the Laplace equation in a curvilinear orthogonal cylindrical coordinate system takes the form:

$$\frac{\partial^2 \varphi}{\partial z^2} + \frac{1}{r}\frac{\partial \varphi}{\partial r} + \frac{\partial^2 \varphi}{\partial r^2} = 0 . \qquad (2)$$

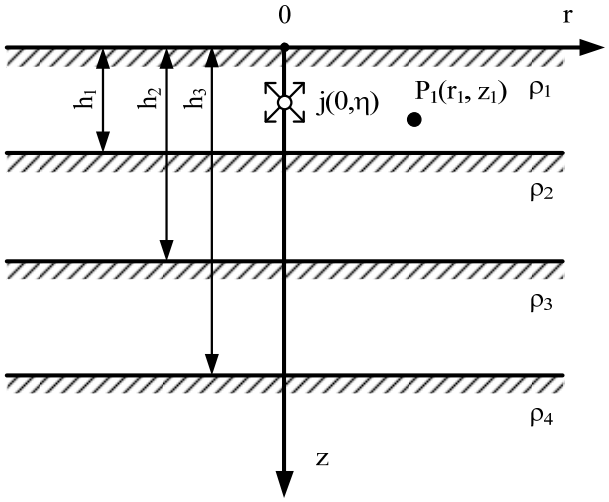

Fig. 2. A point current source j located in the first layer of the four-layer structure; P_1 (r_1, z_1) – observation point

Solution (2) is found by the Fourier method for separation of variables [11]:

$$\varphi(r,z) = \int_0^\infty J_0(\lambda r)\cdot\left(a_i e^{\lambda z} + b_i e^{-\lambda z}\right)d\lambda , \qquad (3)$$

where a_i and b_i are constants determined by soil parameters, coordinates of a point current source and observation point; λ is a separation parameter of variables; J_0 is a zero-order Bessel function of the first kind.

The form of function (3) is common for all layers of the conducting half-space. However, in each layer, depending on the relative position of the point current source and the observation point, the constants take on their particular values. To find the constants a_i and b_i in the first layer, we use the additional conditions:

• with an unlimited increase in the z-coordinate the potential φ tends to zero, therefore

$$a_4 = 0 ; \qquad (4)$$

• in accordance with the principle of electric current continuity at the interface between the i-th and (i+1)-th layers the normal components of the vectors of the electric current density are equal to each other:

$$\frac{1}{\rho_i}\frac{\partial \varphi_i}{\partial z} = \frac{1}{\rho_{i+1}}\frac{\partial \varphi_{i+1}}{\partial z} ; \qquad (5)$$

• from the condition of equality of the tangential components of the electric field strength vector at the boundaries of adjacent layers, at the interface between the i-th and (i+1)-th the potentials are equal:

$$\varphi_i = \varphi_{i+1} ; \qquad (6)$$

• the condition on the boundary of the conducting half-space has the form

$$\left.\frac{\partial \varphi_1}{\partial z}\right|_{z=0} = 0 . \qquad (7)$$

Based on expressions (4) – (7), a system of linear algebraic equations of the 7-th order with respect to the unknown coefficients a_i and b_i was compiled. On the basis of its analytical solution, an expression for the potential of the electric field was obtained in [5]. Considering that when conducting VES, the point current source and the observation point are located only on the soil surface (i.e. $z = 0$ and $\eta = 0$), this expression will take the form:

$$\varphi_{1,1}(r,0)=\frac{I\rho_1}{2\pi}\left[\frac{1}{r}+2K_{2,1}\sum_{n=0}^{m}\frac{K_n}{\sqrt{r^2+(2h_1+H_n)^2}}+\right.$$
$$+2K_{3,2}\sum_{n=0}^{m}\frac{K_n}{\sqrt{r^2+(2h_2+H_n)^2}}+ \quad (8)$$
$$\left.+2K_{4,3}\sum_{n=0}^{m}\frac{K_n}{\sqrt{r^2+(2h_3+H_n)^2}}\right]$$

where $K_{i+1,i}$ is the coefficient of soil heterogeneity equal to $K_{i+1,i}=\frac{\rho_{i+1}-\rho_i}{\rho_{i+1}+\rho_i}$; K_n and H_n are the coefficients obtained as a result of the expansion of the function characterizing the multilayer medium; n is the number of the term of the series; m is the number of terms of the series.

The values of K_n and H_n are found by the least squares method [12] when approximating the function $F_4(\lambda)$, which characterizes a four-layer soil at $\lambda \to \infty$:

$$F_4(\lambda)=\frac{1}{F_Z(\lambda)}, \quad (9)$$

where $F_Z(\lambda)$ is

$$F_Z(\lambda)=1-K_{2,1}e^{-2\lambda h_1}-K_{3,2}e^{-2\lambda h_2}-K_{4,3}e^{-2\lambda h_3}+$$
$$+K_{2,1}K_{3,2}e^{-2\lambda(h_2-h_1)}+K_{2,1}K_{4,3}e^{-2\lambda(h_3-h_1)}+$$
$$+K_{3,2}K_{4,3}e^{-2\lambda(h_3-h_2)}-K_{2,1}K_{3,2}K_{4,3}e^{-2\lambda(h_3-h_2-h_1)}.$$

Thus, a basic expression was obtained for the development of a mathematical model for interpreting the VES results in the form of a four-layer geoelectric structure.

To develop a model that allows us to interpret the results obtained using the Schlumberger method, we will use the expression for determining the apparent resistivity (1), the geometric configuration of the installation itself (see Fig. 1) and the expression for determining the potential on the soil surface (8).

Based on the principle of superposition, the voltage at the potential electrodes M and N will be determined as (10), where φ_{AM}, φ_{BM}, φ_{AN} and φ_{BN} are the values of potential at electrodes M and N, induced from current electrodes A and B, respectively.

Substituting the expression for potential (8) into (10) and taking into account the symmetry of the Schlumberger installation, the voltage drop will have the form (11).

Taking into account (11), the geometric coefficient of installation and transformations, we obtain expression (1) in the following form (12).

$$U=\varphi_M-\varphi_N=\left(\varphi_{AM}\Big|_{r=L_{AM}}-\varphi_{BM}\Big|_{r=L_{BM}}\right)-\left(\varphi_{AN}\Big|_{r=L_{AN}}-\varphi_{BN}\Big|_{r=L_{BN}}\right), \quad (10)$$

$$U=\frac{I\rho_1}{2\pi}\left[\frac{1}{L_{AM}}-\frac{1}{L_{AN}}+2\sum_{i=1}^{4}K_{i+1,i}\left(\sum_{n=0}^{m}\frac{K_n}{\sqrt{{L_{AM}}^2+(2h_i+h_n)^2}}-\sum_{n=0}^{m}\frac{K_n}{\sqrt{{L_{AN}}^2+(2h_i+h_n)^2}}\right)\right], \quad (11)$$

$$\rho_k=\frac{L_{AM}L_{AN}}{(L_{AM}-L_{AN})}\left[\frac{1}{L_{AM}}-\frac{1}{L_{AN}}+2\sum_{i=1}^{4}K_{i+1,i}\left(\sum_{n=0}^{m}\frac{K_n}{\sqrt{{L_{AM}}^2+(2h_i+h_n)^2}}-\sum_{n=0}^{m}\frac{K_n}{\sqrt{{L_{AN}}^2+(2h_i+h_n)^2}}\right)\right]. \quad (12)$$

Based on the obtained expression, a test version of the program was implemented in Visual Basic for Applications to interpret the results of VES by the Schlumberger method. To check the obtained expressions, the interpretation of the VES results (see Table 1) was carried out on the territory of a 150 kV substation of one of the mining and processing plants in the city of Kriviy Rih (see Fig. 3).

Table 1

The results of experimental measurements by the Schlumberger method

$L_{MN}/2$, m	0,1	0,13	0,17	0,22	0,27	0,33	0,4	0,5	0,6	0,8	1
$L_{AB}/2$, m	0,3	0,39	0,51	0,66	0,81	0,99	1,2	1,5	1,8	2,4	3
U/I, Ω	56,01	49,03	34,69	27,91	23,07	19,72	16,39	13,53	11,87	9,491	8,231
ρ_k, Ω·m	70,38	80,1	74,11	77,16	78,27	81,78	82,39	85,01	89,5	95,41	103,43

$L_{MN}/2$, m	1,3	1,7	2,2	2,7	3,3	4	5	6	8	9
$L_{AB}/2$, m	3,9	5,1	6,6	8,1	9,9	12	15	18	24	27
U/I, Ω	6,834	5,199	4,046	3,342	2,861	2,162	1,539	1,176	0,658	0,537
ρ_k, Ω·m	111,64	111,07	111,86	113,39	118,64	108,67	96,7	88,67	66,15	60,73

Comparison of the results of soil sounding by the Schlumberger installation and the interpretation of its results for the same points shows a sufficient degree of approximation (see Fig. 3): the maximum relative error does not exceed 9.7 % (for the second point), and the average relative error is 3.6 %. The results obtained can

be used to determine the electrical properties of the soil, including the propagation of an electromagnetic wave with a short front, created by a special generator [13] that simulates the lightning current.

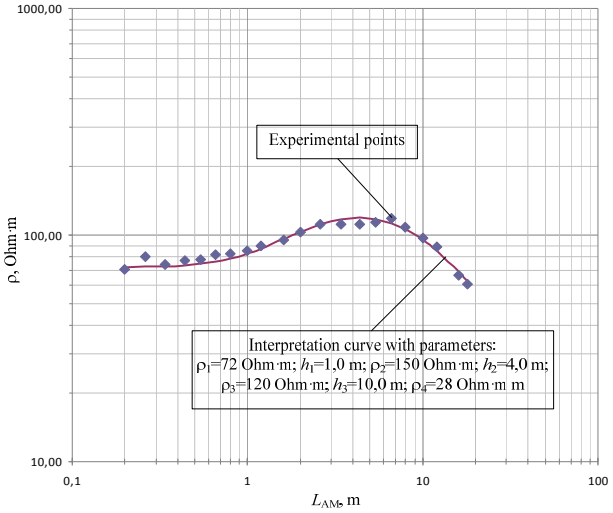

Fig. 3. Interpretation of VES results obtained by the Schlumberger method

Conclusions.

1. Based on the analytical solution of the problem of the field of a point current source located in the first layer of a four-layer geoelectric structure, a mathematical model has been developed for interpreting the results of soil sounding by the Schlumberger installation in the form of a four-layer geoelectric structure.

2. Based on experimental studies carried out at the existing 150 kV substation, the correctness of the developed mathematical model was confirmed. A test computer program has been developed for the interpretation of soil sounding results in an interactive mode.

3. The developed mathematical model will make it possible to increase the sounding depth, and, consequently, the accuracy of determining the standardized parameters of the grounding arrangements of power stations and substations.

Conflict of interest. The authors declare that they have no conflicts of interest.

REFERENCES

1. *IEEE Std 80-2013. Guide for Safety in AC Substation Grounding.* New York, IEEE, 2013. 206 p. doi: https://doi.org/10.1109/IEEESTD.2015.7109078.

2. *IEEE Std 81-2012. Guide for Measuring Earth Resistivity, Ground Impedance, and Earth Surface Potentials of a Grounding System.* New York, IEEE, 2012. 86 p. doi: https://doi.org/10.1109/IEEESTD.2012.6392181.

3. Kolesnikov V.P. *Osnovy interpretatsii elektricheskikh zondirovanii* [The base of interpretation of electrical soundings]. Moscow, Scientific World Publ., 2007. 248 p. (Rus).

4. Koliushko D.G., Rudenko S.S., Koliushko G.M. Analysis of electrophysical characteristics of grounds in the vicinity electrical substation of Ukraine. *Electrical Engineering & Electromechanics*, 2015, no. 3, pp. 67-72. (Rus). doi: https://doi.org/10.20998/2074-272x.2015.3.10.

5. Koliushko D.G., Rudenko S.S. Interpretation the results of the vertical electrical sounding as the geoelectrical half space with four layer. *Bulletin of NTU «KhPI»*, 2015, no. 12 (1121), pp. 324-329. (Rus).

6. Koliushko D.G., Rudenko S.S., Asmolova L.V., Tkachova T.I. Determination of the soil sounding depth for the earthing resistance calculation of substations 35 kV. *Electrical Engineering & Electromechanics*, 2020, no. 1, pp. 52-55. doi: https://doi.org/10.20998/2074-272x.2020.1.08.

7. Lagace P.J., Fortin J., Crainic E.D. Interpretation of resistivity sounding measurements in N-layer soil using electrostatic images. *IEEE Transactions on Power Delivery*, 1996, vol. 11, no. 3, pp. 1349-1354. doi: https://doi.org/10.1109/61.517490.

8. Colominas I., Navarrina F., Casteleiro M. Analysis of transferred Earth potentials in grounding systems: a BEM numerical approach. *IEEE Transactions on Power Delivery*, 2005, vol. 20, no. 1, pp. 339-345. doi: https://doi.org/10.1109/TPWRD.2004.835035.

9. Arnautovski-Toseva V., Grcev L. Image and exact models of a vertical wire penetrating a two-layered earth. *IEEE Transactions on Electromagnetic Compatibility*, 2011, vol. 53, no. 4, pp. 968-976. doi: https://doi.org/10.1109/TEMC.2011.2149533.

10. Arnautovski-Toseva V., Grcev L. On the image model of a buried horizontal wire. *IEEE Transactions on Electromagnetic Compatibility*, 2016, vol. 58, no. 1, pp. 278-286. doi: https://doi.org/10.1109/TEMC.2015.2506608.

11. Burgsdorf V.V., Yakobs A.I. *Zazemlyayushchie ustroystva elektroustanovok* [Grounding arrangement of electrical installations]. Moscow, Energoatomizdat Publ., 1987. 400 p. (Rus).

12. Rencher A.C., Christensen W.F. *Methods of multivariate analysis, Third Edition.* John Wiley & Sons, Inc., 2012. 768 p. doi: https://doi.org/10.1002/9781118391686.

13. O. Rezinkin, M. Rezinkina, A. Danyluk, R. Tomashevskyi, Formation of high-voltage pulses with nanosecond fronts in low-impedance loads. *IEEE 2nd Ukraine Conference on Electrical and Computer Engineering (UKRCON)*, 2019, pp. 464-467 doi: https://doi.org/10.1109/UKRCON.2019.8880015.

Received 15.06.2021
Accepted 30.08.2021
Published 26.10.2021

D.G. Koliushko[1], *PhD, Senior Research Scientist,*
S.S. Rudenko[1], *PhD, Senior Research Scientist,*
Abdel Nour Saliba[2], *General Manager, Postgraduate Student,*
[1] National Technical University «Kharkiv Polytechnic Institute», 2, Kyrpychova Str., Kharkiv, Ukraine, 61002,
e-mail: nio5_molniya@ukr.net (Corresponding author)
[2] TMC Group,Beirut, Horsh Tabet, Sin el Fil, Lebanon,
e-mail: abdel.nour.saliba@gmail.com

How to cite this article:
Koliushko D.G., Rudenko S.S., Saliba A.N. Method of integro-differential equations for interpreting the results of vertical electrical sounding of the soil. *Electrical Engineering & Electromechanics*, 2021, no. 5, pp. 67-70. doi: https://doi.org/10.20998/2074-272X.2021.5.09.

Матеріали приймаються за адресою:
Кафедра "Електричні апарати", НТУ "ХПИ", вул. Кирпичова, 21, м. Харків, 61002, Україна
Електронні варіанти матеріалів по e-mail: a.m.grechko@gmail.com

Довідки за телефонами: +38 050 653 49 82 Клименко Борис Володимирович
+38 067 359 46 96 Гречко Олександр Михайлович

Передплатний індекс: 01216